Ultrasound Speckle Image Velocimetry: Studies on System Performance and Application to Cardiovascular Fluid Dynamics

Thesis by
Ben Albert Lin

In Partial Fulfillment of the Requirements for
the degree of
Doctor of Philosophy

CALIFORNIA INSTITUTE OF TECHNOLOGY
Pasadena, California

2018
(Defended September 30, 2009)

DEDICATION

To my parents.

ACKNOWLEDGEMENTS

I would like to thank my advisor and mentor, Professor Morteza Gharib, as well as the members of my dissertion committee (Professors John Dabiri, Scott Fraser, and Changhuei Yang) for all of their guidance and support.

ABSTRACT

Knowledge of detailed blood flow characteristics can be extremely valuable in a variety of settings. Examples range from studying disease processes such as atherosclerosis to aiding in the design of medical devices such as prosthetic cardiac valves. For *in vivo* and optically inaccessible *in vitro* flows, accurate measurements of velocity fields and shear stresses can be difficult to obtain. Doppler ultrasound and magnetic resonance imaging are the most commonly used techniques, but have important limitations. Recently, there has been increased interest in the application of particle image velocimetry principles towards tracking of ultrasound speckle patterns to determine multidimensional flow velocities with increased temporal resolution. We refer to our implementation as ultrasound speckle image velocimetry (USIV). In this research project, our first objective was to obtain a detailed characterization of the factors unique to ultrasound imaging that can influence the accuracy of velocity measurements. By conducting *in vitro* experiments with uniform speckle phantom translation as well as steady tube flow, we have shown that characteristics such as transducer focal depth and beam sweep speed as well as particle motion direction and velocity can all influence USIV results. Our second objective was to demonstrate the utility of USIV for analyzing *in vivo* blood flows. After administering ultrasound contrast agent to anesthetized pigs, we were able to obtain detailed images of both left ventricular flow and abdominal aortic flow. Velocity profiles were measured during both left ventricular filling and ejection. Our most interesting finding was the presence in certain cases of highly asymmetric retrograde flow in the infrarenal aorta. The factors that lead to such flows may have relevance to the development of atherosclerosis and abdominal aneurysms. USIV is likely to be very useful for further studies both *in vivo* and with *in vitro* elastic aorta models.

TABLE OF CONTENTS

LIST OF ILLUSTRATIONS AND TABLES

Page

Page

Page

Chapter 1

BACKGROUND

A. Introduction

Biological fluid dynamics involves fluid flows that are either external or internal to organisms (Fung, 1990). Examples of external flows include the swimming of fish and the flight of birds. Examples of internal flows include blood flow in the heart and vasculature, air flow in the lungs and fluid flow in the lymphatic system. Cardiovascular blood flow has been the most widely studied type of internal flow in biological systems.

The study of cardiovascular fluid dynamics was documented in the early 1500s when Leonardo DaVinci sketched depictions of flow through the aortic valve (Gharib et al., 2002). More recently, especially during the last several decades, there has been tremendous interest in understanding the principles most relevant to blood flow (Nichols and O'Rourke, 2005; Thiriet, 2008a, 2008b). Studies have been conducted with a number of approaches including simulations, *in vitro* flow phantoms and *in vivo* experiments with either noninvasive or invasive measurements. These studies have involved a wide variety of topics such as fundamental pathophysiology, diagnostic imaging, and medical device design. Research questions can be focused on macroscopic (e.g., vascular grafts) or microscopic spatial scales (e.g., cell surface shear stress receptors). Such knowledge can contribute greatly to the understanding of disease processes as well as aid in the design of devices for diagnostic or treatment purposes.

Several interesting applications and research approaches related to cardiovascular fluid dynamics will be discussed below. This will be followed by an introduction to the use of ultrasound for cardiovascular imaging. Existing tools that combine blood flow velocity measurements with anatomic imaging (allowing for quantitative flow visualization) will then be described.

B. Cardiovascular Fluid Dynamics

The mammalian cardiovascular system consists of a four-chambered heart that pumps oxygenated blood from the left atrium to left ventricle and then through the aorta into a branching network of arteries and arterioles before reaching capillary beds where oxygen can diffuse into surrounding tissues. Deoxygenated blood collects in venules and veins before returning to the right atrium of the heart assisted by peripheral muscle contractions. This blood is transported to the right ventricle and pumped through the lung vasculature and alveolar capillaries to be oxygenated again prior to returning to the left atrium to restart the cycle. This arrangement is illustrated in Figure 1-1.

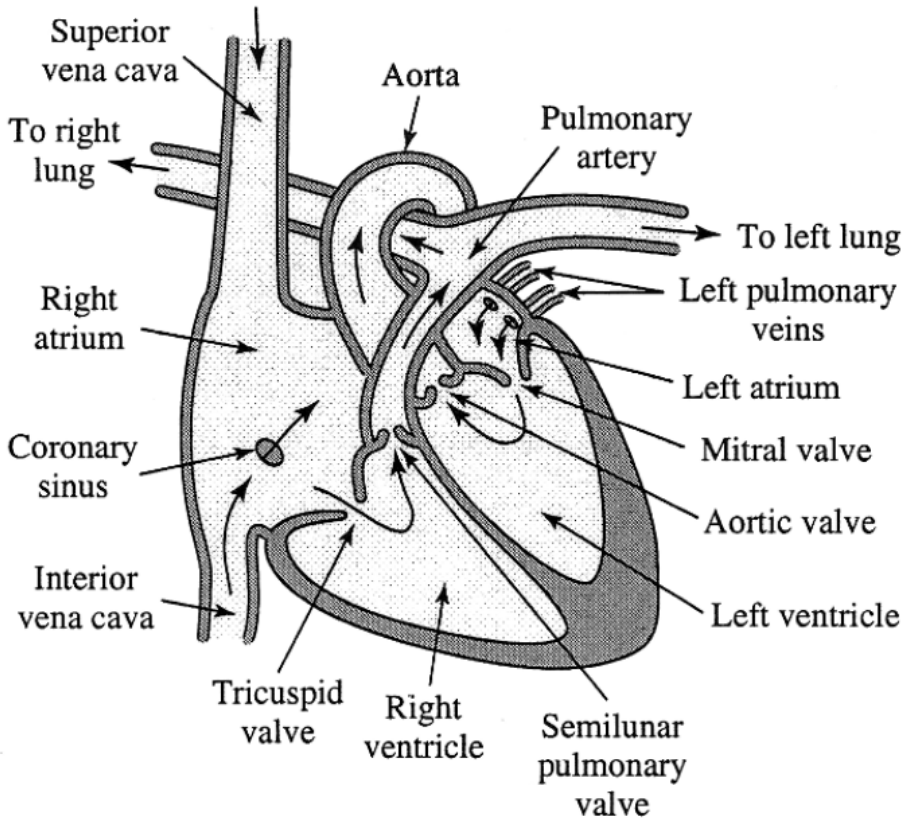

Figure 1-1. Schematic depicting the normal pattern of blood flow through the cardiac chambers and vasculature. Reprinted with permission from Benedek (2000).

Blood is a complex fluid consisting of formed elements such as erythrocytes and leukocytes that are suspended in plasma. For vessel diameters greater than 0.5 mm, the suspension can be considered to behave as a Newtonian fluid (Nichols and O'Rourke, 2005). At smaller length scales, such as in the capillaries, the size of the flexible erythrocytes becomes larger than the vessels and special models are needed to account for the observed rheological properties of blood (Fung, 1997).

Analytical approaches have incorporated the above assumptions to derive parameters that dictate the fundamental flow characteristics in various settings. For instance, the Womersley number α has been shown to be a valuable dimensionless index for describing pulsatile flow in arteries (Fung, 1997; Nichols and O'Rourke, 2005). The Womersley number represents the ratio of oscillatory inertial forces to shear forces and is defined as

$$\alpha = D\sqrt{\frac{\omega\rho}{\mu}}\ , \tag{1.1}$$

where D is the vessel diameter, ω is the oscillatory frequency, ρ is the fluid density, and μ is the fluid viscosity.

Arterial flows have also been analyzed by methods similar to those used for electrical circuits and the concept of impedance has a similarly crucial role in understanding pressure-flow relationships (Fung, 1997; Nichols and O'Rourke, 2005). Computational approaches have included attempts to represent the many components of the cardiovascular system using lumped parameter models. More detailed finite element models have been used to describe the fluid flow related to left ventricular filling, branching arterial geometries, and prosthetic cardiac valves. Fluid-structure interaction models have been developed that directly couple the dynamics of the cardiac valves with the dynamics of blood flow through and around them (Thiriet, 2008b).

A variety of experimental approaches have also been used to obtain useful insights. Some of these involve the use of biological tissue samples or animal preparations, while others have utilized flow phantoms that mimic physiologic conditions. Biaxial testing of excised artery specimens has been used to determine elastic properties for utilization in computational models of pulsatile flow (Fung, 1993). Pulsatile flow simulators with rigid acryclic chambers have been used to estimate the shear stresses experienced by mechanical and tissue prosthetic cardiac valves (Chandran et al., 2007). Doppler ultrasound has been used in a large variety of experimental and clinical settings, especially related to flow across cardiac valves and in the large arteries (Feigenbaum et al., 2005). Accurate measurement of multi-component velocity vectors remains an important challenge to achieving detailed visualization of flow patterns and properly understanding the fundamental flow phenomena that are present. Several existing approaches for obtaining flow velocities and spatial flow patterns are discussed below.

Specific details regarding left ventricular and abdominal aortic flows will also be discussed in later sections.

C. Ultrasound Physics and Imaging

Ultrasound refers to sound waves with frequencies greater than those that can be heard by humans. Medical ultrasound typically utilizes frequencies ranging from 1 to 10 MHz (Webb, 2003). Transducers made from piezoelectric crystals are used to transmit and receive ultrasound pulses that can provide information regarding the tissue into which they are transmitted. These pulses propagate through the surrounding medium as longitudinal sound waves. Reflections occur whenever there are changes in acoustic impedance at either stationary or moving interfaces. These backscattered ultrasound signals are recorded by the receiving transducer and, after signal processing that includes envelope detection using a quadrature filter or Hilbert transform, are converted into visual representations that can be used to interpret the anatomy and physiology of the subject. The use of

ultrasound to image cardiac structures is termed echocardiography. Historically, A-mode ("amplitude" mode) was used to display reflected signal spikes at different depths along a single beam. For current clinical examinations, the most common visualizations include M-mode ("motion" mode), B-mode ("brightness" mode), spectral velocity displays (from either continuous wave Doppler or pulsed wave modes), and color flow imaging. Examples of such images are shown in Figures 1-2 through 1-5. While each of these image types provides useful clinical information, two-dimensional B-mode imaging provides the best combination of spatial and temporal resolution. Note that pulsed wave velocity measurements are often referred to as pulsed wave Doppler measurements, but this is actually a misnomer since the Doppler effect is not directly utilized (Cobbold, 2007).

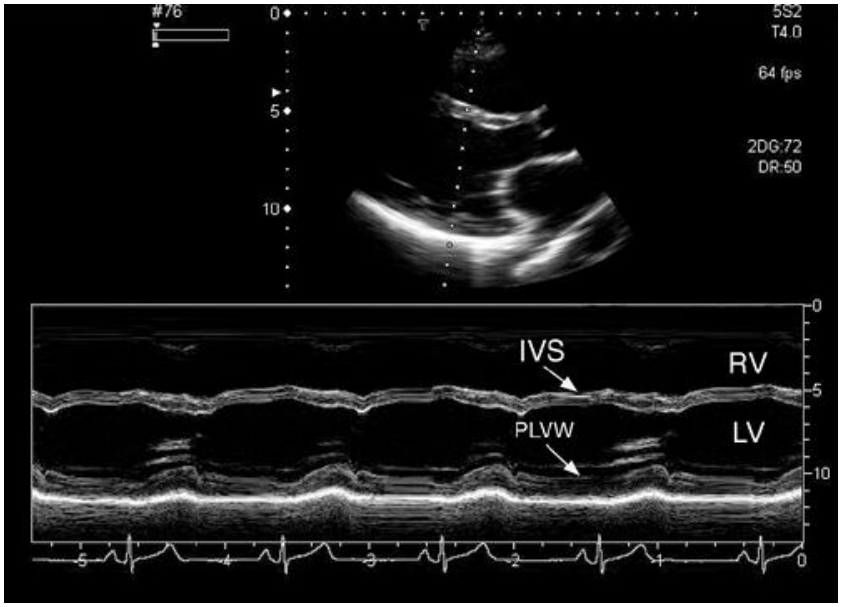

Figure 1-2. M-mode display (at the bottom of the panel) is shown along with the two-dimensional image and beam orientation from which it was derived. Abbreviations: IVS, interventricular septum; PLVW, posterior left ventricular wall; RV, right ventricle; LV, left ventricle. Reprinted with permission from Feigenbaum et al. (2005).

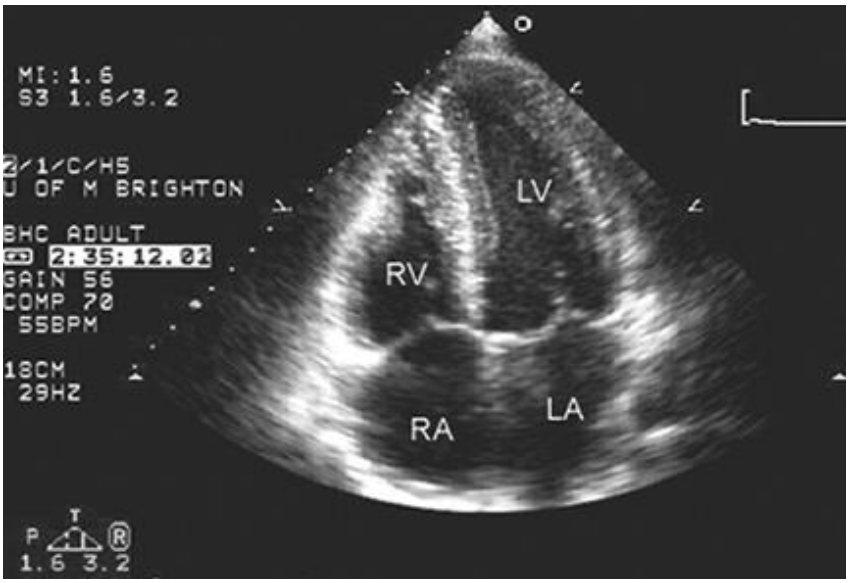

Figure 1-3. Two-dimensional B-mode image acquired from apical four-chamber transducer position. Abbreviations: RV, right ventricle; LV, left ventricle; RA, right atrium; LA, left atrium. Reprinted with permission from Feigenbaum et al. (2005).

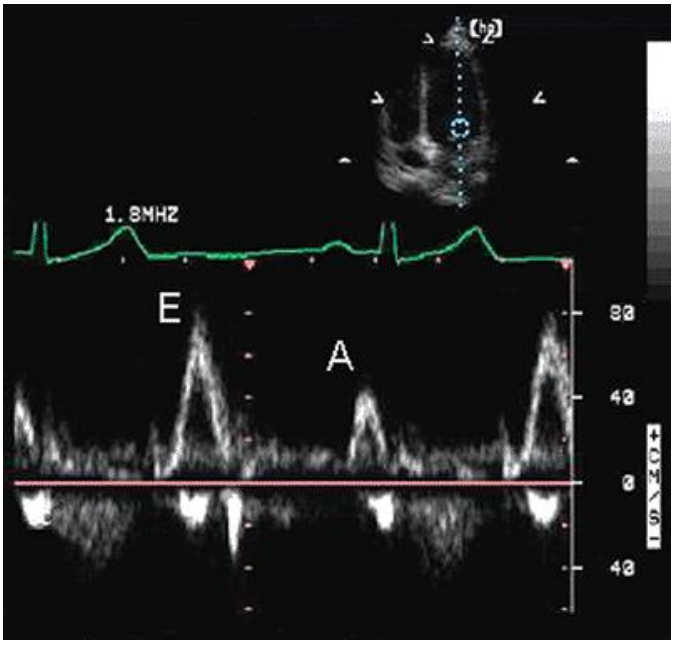

Figure 1-4. Pulsed wave spectral display of mitral inflow velocities. E-wave (due to ventricular relaxation) and A-wave (due to atrial contraction) are labeled. Reprinted with permission from Feigenbaum et al. (2005).

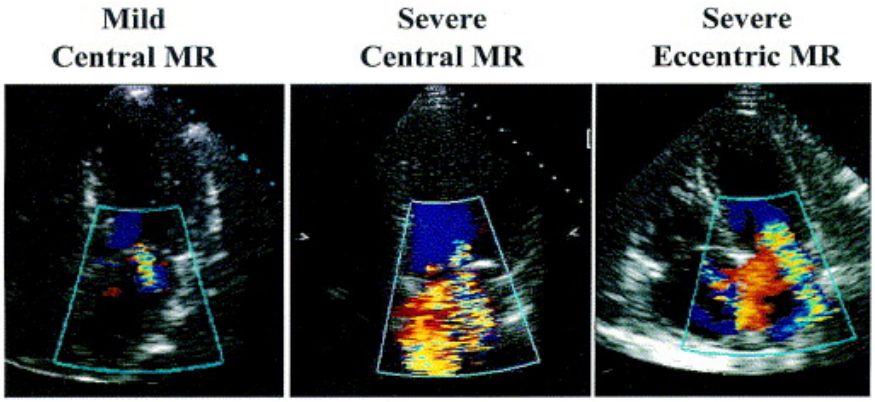

Figure 1-5. Color flow imaging from apical views showing mitral regurgitation jets with varied appearances and degrees of severity. Reprinted with permission from Zoghbi et al. (2003).

B-mode image characteristics are influenced by several factors including depth, width, focus position, transmit frequency, and scan line density. Ultimately, this is due to the influence of these factors on temporal as well as axial and lateral spatial resolution. It should be noted that while B-mode images resemble photographic snapshots, they are, in fact, reconstructed frames from multiple scan lines that are acquired at slightly different times (see Figures 1-6 and 1-7). For clinical purposes, it is assumed that each reconstructed frame represents a single instant in time. Practically, however, there is always a trade-off between temporal and spatial resolution related to the factors that dictate the scan time requirements for each frame (i.e., depth, width, and scan line density).

Ultrasound transducer behavior can be illustrated by considering an unfocused single element transducer (Webb, 2003). There is a near-field, or Fresnel, region with a complicated and oscillating axial pressure distribution but a relatively constant beam width. This is followed by a far-field, or Fraunhofer, region where the axial pressure distribution decays exponentially and the beam width gradually increases according to a transducer specific angle of deviation. Weaker side lobes are generated that propagate at different angles relative to the

main beam, but can result in imaging artifacts if there are strong reflectors in any of those directions.

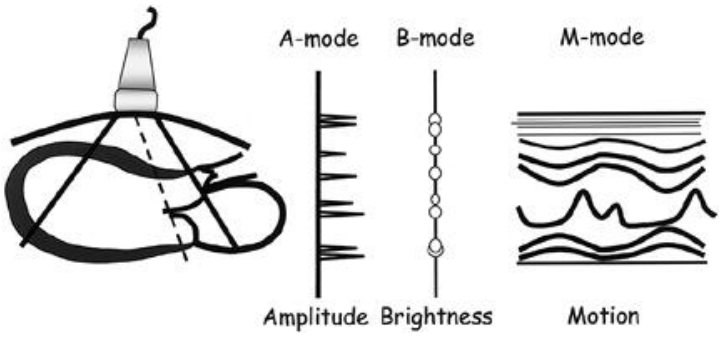

Figure 1-6. Ultrasound signals are displayed by using information from scan line acquisitions. The amplitude envelope is derived from the backscattered radiofrequency signal obtained from a single scan line. This envelope is used to assign grayscale intensity values along a scan line over time (in M-mode) or for multiple sequentially acquired scan lines (in a composite two-dimensional B-mode image.) Reprinted with permission from Feigenbaum et al. (2005).

Ultrasound beams can be focused in order to improve lateral (also known as azimuthal) resolution in a desired region. This can be achieved by placing a lens on the transducer surface, using a curved transducer element, or using staggered pulse sequences (in the case of multi-element phased array transducers). The desired level of beam focusing power involves a compromise between achieving the narrowest beam width (and improved lateral resolution) at the cost of increased beam divergence after the focal plane (leading to a smaller depth-of-field or overall region for which there is good lateral resolution).

The lateral resolution of the transmitted ultrasound beam depends upon the center frequency, bandwidth, effective aperture diameter, beam focusing strength, distance from the transducer, scan line density, and tissue attenuation properties. Using a multiple element transducer array allows both transmit and receive beam focusing characteristics to be modified in a complementary fashion (Szabo, 2004).

The best lateral resolution for a focused transducer is at the focal depth where the beam width is smallest and on the order of about one millimeter (see Table 1-1). While there are several possible approaches to evaluate this, one is to consider the full width at half maximum ($FWHM$) amplitude for the ultrasound beam at any given depth (Cobbold, 2007). For a focusing disk transducer (with a concave single element), this can be calculated at the focal depth F using

$$FWHM = 1.4\lambda \frac{F}{D} \approx 1.4\lambda \frac{R}{D} , \tag{1.2}$$

where λ is the wavelength of the ultrasound center frequency, F is the focal length, D is the aperture diameter, and R is the radius of curvature. The focusing strength can be described, as in optics, using

$$f\text{-number} = \frac{F}{D} . \tag{1.3}$$

Frequency (MHz)	λ In Tissue (mm)	*R* (cm)	*a* (cm)	*f*-Number	FWHM (mm)	DOF (mm)
1.5	1.0	2	1	1	1.1	11.9
1.5	1.0	3	1	1.5	1.7	20.5
1.5	1.0	5	1	2.5	2.8	37.5
1.5	1.0	10	1	5	5.6	79.8
5	0.31	2	2	1	0.3	3.6
5	0.31	3	2	1.5	0.5	6.1
5	0.31	5	2	2.5	0.8	11.2
5	0.31	10	2	5	1.7	24.0

Table 1-1. Lateral focusing properties of various transducer and lens combinations. Lateral resolution is best at the focal plane and listed in the column labeled FWHM. The *f*-number is defined as *R/2a*. Abbreviations: *R*, lens radius of curvature; *a*, radius of transducer element; FWHM, full-width at half maximum amplitude; DOF, depth of focus. Reprinted with permission from Webb (2003).

As described earlier, beam width is markedly increased in the far-field of a focused ultrasound beam since there is significant divergence after the focal

plane. For a multiple element transducer, it is possible for scan line density to become the limiting factor for lateral resolution in certain portions of the image. This occurs if the scan line spacing exceeds the beam width at any given depth. For a phased array transducer, in particular, scan line density decreases with depth. Commonly used multiple element array transducers can achieve focal plane lateral resolutions of approximately two wavelengths of the transmit center frequency. This equals approximately 1.2 mm for a 2.5 MHz transducer with an assumed speed of sound of 1540 m/sec (Szabo, 2004).

Axial resolution is directly related to the pulse duration, which is, in turn, related to the center frequency and bandwidth of the transducer as well as tissue attenuation properties. Theoretically, the axial resolution AR is dependent upon the ultrasound wavelength λ and the number of cycles per pulse (which is inversely related to the bandwidth). It is equal to half of the spatial pulse length (Webb, 2003), so

$$AR = \frac{1}{2} n\lambda \,, \tag{1.4}$$

where n is the number of cycles per pulse. For a 2.5 MHz transducer with $n = 2$, the axial resolution $AR \approx 0.6$ mm (Suetens, 2009; Webb, 2003). Technically, however, the axial resolution will be slightly worse at increased depth since the center frequency and bandwidth decrease due to frequency-dependent tissue attenuation (Shung, 2006). Other factors, such as transducer design (including crystal damping and electronic processing behavior) as well as video monitor quality, have important effects also. In practice, commonly used transducer and display systems achieve axial resolutions on the order of about two wavelengths of the transmit center frequency or approximately 1.2 mm for a 2.5 MHz transducer (Szabo, 2004). While the best achievable lateral resolution may technically be similar (see above), that is only true near the focal plane depth since ultrasound images have spatially variant resolution.

Ultrasound beams have a finite slice thickness that can be referred to as the elevational thickness or beam width. This can lead to the misleading appearance of nearby "out-of-plane" structures within an image. An example would be artifactual echodensities that appear to mimic tissue or debris within a cystic fluid-filled structure. This phenomenon can be considered to be analogous to the partial volume effects seen with volumetric cross-sectional imaging modalities such as computed tomography or magnetic resonance imaging. In a similar fashion, this decreases the effective spatial resolution of ultrasound images, especially in the far-field region where both lateral and elevational beam widths are relatively large.

Speckle refers to the grainy texture that is generated in ultrasound images of tissues containing multiple sub-wavelength scatterers per unit volume. This situation applies to scatterers located within the myocardium and also, more weakly, to red blood cells located in the heart or vasculature. This phenomenon is known as diffusive, or Rayleigh, scattering (Jensen, 1996; Szabo, 2004). The alternating constructive and destructive interference of the composite backscattered signal leads to the speckle pattern. While it is sometimes referred to as speckle "noise," the generated pattern is deterministic rather than random. Its appearance is dictated by the interaction of transducer characteristics with any specific distribution of scatterer locations (Foster et al., 1983; Szabo, 2004; Wagner et al., 1983). For a stationary tissue or tissue-mimicking phantom, returning the specimen to the same exact location relative to the transducer will produce an identical speckle pattern. While speckle is considered undesirable with respect to image contrast, it can be exploited for tissue or tracer tracking in certain situations that will be discussed further below.

D. Blood Flow Imaging with Velocity Estimation

1. Magnetic Resonance Phase-Contrast Velocity Mapping

Magnetic resonance (MR) imaging can be used to evaluate blood flow through the use of phase-contrast velocity-encoded pulse sequences (Chai and Mohiaddin, 2005; Gatehouse et al. 2005). With this technique, a reference phase image is subtracted from a velocity-encoded phase image in order to obtain a phase-contrast image (also known as a velocity map). The resultant phase shift at each pixel in the phase-contrast image is directly proportional to the velocity of that material element in the direction of the magnetic field gradient.

There has been interest in phase-contrast velocity mapping of cardiovascular blood flows for several decades (Bryant, 1984; Van Dijk, 1984). This technique has been used for flow quantification across valves for cardiac output and valvular regurgitation assessments. Phase-contrast MR imaging has also been used to visualize flow patterns in cardiac chambers (Kilner et al., 2000; Wigstrom et al. 1999) as well as in aortic aneurysms (Hope, 2007).

Limitations of this approach include suboptimal temporal resolution requiring ECG-based gating and long breath holds by patients to avoid motion artifacts. There is a risk of aliasing if velocities are too high for a given set of acquisition parameters. Misalignment can occur between the true direction of flow and the magnetic gradients used to obtain through-plane velocities. Background phase correction is also required to avoid errors in velocity measurements (Buonocore and Bogren, 1992). Generally, patients with implanted internal defibrillators or permanent pacemakers are not allowed to have MR scans due to safety concerns.

2. Doppler Ultrasound and Color Flow Imaging

The Doppler principle can be exploited in order to estimate flow velocities towards or away from an ultrasound transducer. This is due to the fact that

moving objects will change the frequency of reflected sound waves compared to incident waves by an amount that is proportional to the speed of those objects. In mammals, the red blood cells that carry oxygen throughout the circulatory system act as ultrasound scatterers and can, under most conditions, be considered as tracer particles of the fluid motion.

Cobbold (2007) described that the frequency shift, Δf, caused by scatterers moving away from the transducer can be determined using

$$\Delta f \approx -\frac{2v}{c} f_0 \cos\theta \,, \tag{1.5}$$

where v is the scatterer velocity, c is the speed of sound in blood, f_0 is the transmitted frequency, and θ is the angle of incidence. The relevant geometry is depicted in Figure 1-7. Equation (1.5) is derived with the assumptions that the speed of the scatterer is much less than the speed of sound ($v \ll c$) and that the flowing medium has a uniform velocity profile. The negative sign arises because the reflected frequency from a scatterer moving away from the transducer will be lower than the transmitted frequency. If the scatterer is moving towards the transducer, then the frequency shift is determined using

$$\Delta f \approx \frac{2v}{c} f_0 \cos\theta \,. \tag{1.6}$$

Transducers are designed to detect velocities using either continuous wave (CW) Doppler or pulsed wave (PW) ultrasound modes. With CW transmission, separate transmitter and receiver elements operate simultaneously. No depth discrimination is possible because backscattered signals are received simultaneously from scatterers at all positions along the beam line. At every time point during the acquisition, the spectrum of detected frequency shifts (i.e., Doppler shifts) correlates to the spectrum of velocities along the beam line.

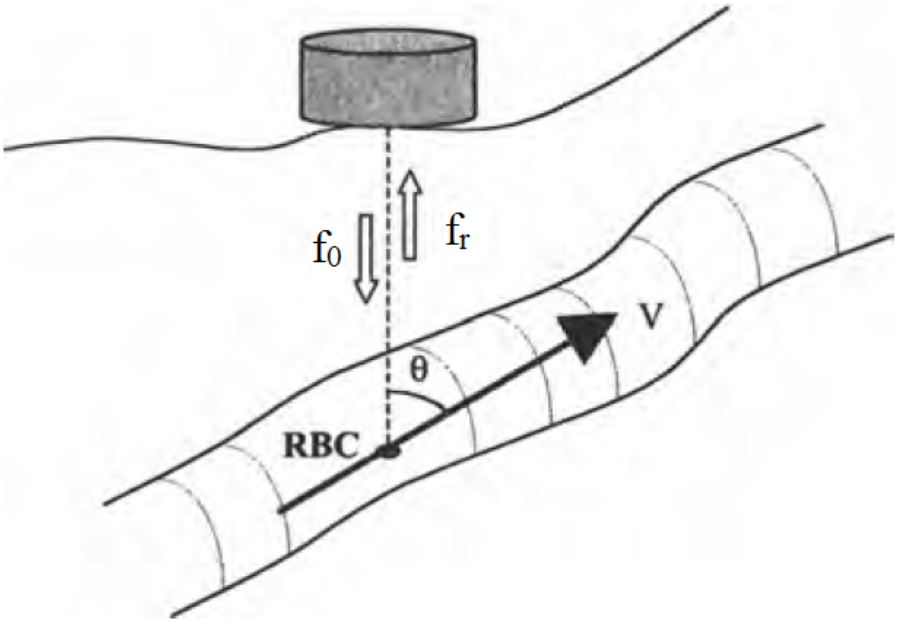

Figure 1-7. A typical arrangement of ultrasound transducer, blood vessel and moving red blood cells that act as scatterers where f_0 is the transmitted frequency and f_r is the reflected frequency. Adapted with permission from Webb (2003).

With PW transmission, short radiofrequency (RF) pulses are transmitted and then followed by a receiving period. PW techniques do not involve the detection of Doppler frequency shifts. Instead, the backscattered waveforms received after successive pulses are assumed to be unchanged and, typically, the relative time delays or phase shifts between them are used to determine the scatterer velocities at the depth of the chosen sample volume or range gate (Cobbold, 2007). Therefore, in contrast to CW techniques, PW velocity measurements are associated with specific locations. This comes at the expense of having a maximum detectable, or aliasing, velocity that is related to the Nyquist limit of the pulse repetition frequency that is used.

Color flow imaging also does not actually detect Doppler frequency shifts and, instead, utilizes sequential transmissions where each backscattered signal

that is received is separated into multiple range gates. The truncated waveforms for each range gate are compared sequentially for time delays or phase shifts in order to determine the velocity (in similar fashion to PW techniques). These velocities are superimposed using a color-coded scale upon anatomic B-mode images that are concurrently obtained (as shown in Figure 1-5).

The primary limitation of CW Doppler and PW techniques is that velocities can only be measured along the axial direction of the transmitted ultrasound beam. No information is available regarding the velocity component perpendicular to the ultrasound beam (in the lateral direction). For this reason, alignment of the transducer with the primary direction of the flow being evaluated is critical for accurate measurements (although this is not always achievable). As mentioned earlier, CW Doppler does not allow spatial discrimination of velocities. PW (and color flow imaging) techniques do allow spatial interrogation, but can be limited by aliasing. In addition, PW techniques generally require a compromise between the axial resolution and signal-to-noise ratio of the velocity measurements (Cobbold, 2007).

Accordingly, while traditional ultrasound techniques are often useful for one-dimensional velocity measurements and qualitative descriptions, they are quite limited with regard to allowing detailed flow analyses. Multi-component velocity measurements that can be superimposed upon anatomic images are required for true quantitative flow visualization.

3. Digital Particle Image Velocimetry

Development of robust velocimetry techniques has been of vital importance to research in fluid mechanics. Whole field measurement techniques allow for quantitative flow visualization and improved understanding of the spatial characteristics of complex flows. Particle image velocimetry (PIV) was introduced as a means to perform statistical tracking of groups of particles and avoid the labor-intensive tracking of individual particles associated with particle

tracking velocimetry (PTV). A complete description of the fundamental principles and historical development of PIV can be obtained from the excellent references by Raffel et al. (2007), Adrian (2005), and Westerweel (1997).

The basic concept involves attempting to track the displacement of small groups of particles forming particle image patterns that are assumed to be unchanged over short time intervals. Typically, multi-frame single-exposure image acquisitions are obtained. The interframe displacement for a given particle group is estimated by performing cross-correlations between the original particle image pattern and all of the possible displacements within the interrogation window. The displacement giving the highest cross-correlation coefficient is then used to determine the interframe velocity for a representative particle located at the center of the original particle image pattern. Experimental arrangements are typically similar to the one shown in Figure 1-8.

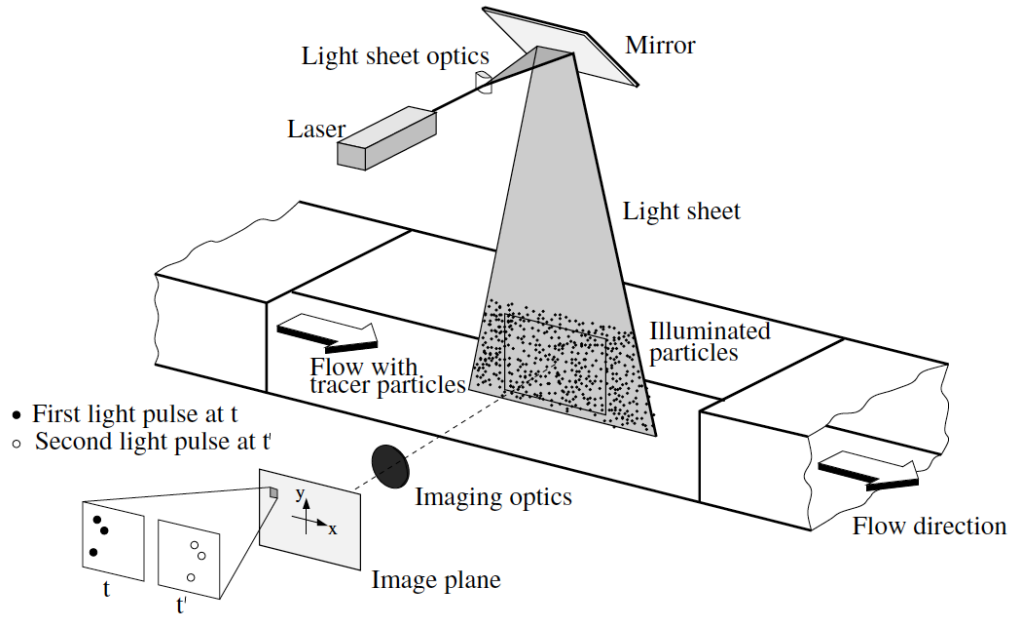

Figure 1-8. Schematic illustrating a typical experimental setup for particle image velocimetry data acquisition. Reprinted with permission from Raffel et al. (2007).

The introduction of digital particle image velocimetry (DPIV) by Willert and Gharib (1991) addressed several important technical challenges. First, acquisition and processing of images was performed with digital rather than photographic techniques. Second, a novel methodology was introduced for the determination of cross-correlation peaks that involved performing the computations in the frequency, rather than spatial, domain and using the fast Fourier transform (FFT) rather than the discrete Fourier transform (DFT) during that process. This took advantage of the fact that the cross-correlation of two spatial functions is equivalent to the complex conjugate multiplication of their respective Fourier transforms. The conceptual scheme is illustrated in Figure 1-9. As described by Brigham (1988) and Raffel et al. (2007), the number of required multiplication operations is reduced from $O(N^4)$ to $O(N^2 \log_2 N)$.

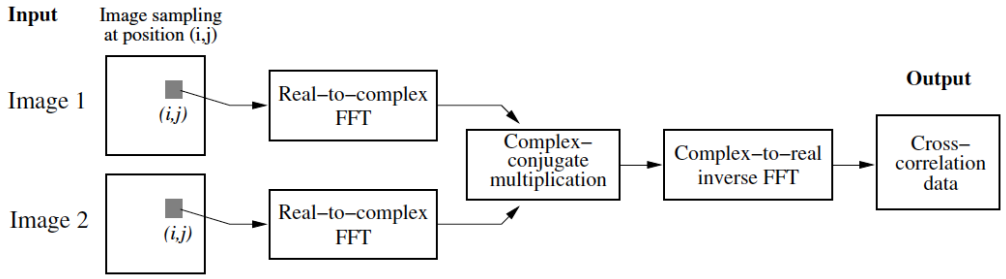

Figure 1-9. Block diagram depicting cross-correlation computation by frequency domain approach utilizing the fast Fourier transform. Reprinted with permission from Raffel et al. (2007).

Willert and Gharib (1991) also introduced the use of a three-point Gaussian peak fit for estimation of the correlation peak with better accuracy compared to using center-of-mass centroiding. Westerweel et al. (1997) later showed that using a window offset obtained from an initial estimate of the displacement lead to further improvement in accuracy. These techniques have been shown to result in average measurement errors that are typically much less

than a single pixel in magnitude. Several other computational refinements have since been developed that have increased the reliability and applicability of DPIV even further (Adrian, 2005; Raffel et al., 2007). The term PIV is now often used interchangeably with DPIV since the technique is almost exclusively performed digitally.

The development of an accurate and experimentally feasible whole field velocimetry technique proved to be a major advance for the field of fluid mechanics. A myriad of applications have been explored involving aeronautical, mechanical, chemical, civil, and biomedical engineering. Related principles have been used to devise three-dimensional velocimetry techniques, such as defocusing DPIV or DDPIV (Pereira and Gharib, 2002; Pereira et al., 2000).

While conventional DPIV involves the use of optical tracers and image acquisition, there has recently been interest in using ultrasound-generated images to estimate velocities in a similar fashion. Further details will be discussed in the next section.

4. Ultrasound Speckle Tracking and Fluid Velocimetry Techniques

The concept of using ultrasound speckle patterns to track material elements within a fluid or solid continuum is commonly referred to as speckle tracking. Early publications related to fluid flow included those by Robinson et al. (1982), Trahey et al. (1987), and Trahey et al. (1988). Speckle tracking can be performed on either radiofrequency (RF) or envelope-detected ultrasound data acquisitions (Bohs et al., 2000). Typically, the latter approach is taken and performed by dividing two-dimensional B-mode images into subregions and mapping frame-to-frame displacements of the corresponding speckle patterns. This can be done when the speckle patterns are relatively stable between frames. An effective technique is to find the displacement for each speckle pattern that gives the maximum normalized cross-correlation between consecutive images. It should be noted that while speckle tracking measurements are much less angle-

dependent than Doppler measurements, they are not entirely angle-independent due to the spatially-variant nature of the ultrasound images.

A major initial obstacle was the significant computational burden of performing multiple direct cross-correlations. In order to facilitate real-time speckle tracking capabilities, a number of alternative correlation algorithms and scanning protocols were suggested. Bohs and Trahey (1991) suggested using a sum-absolute-difference (SAD) algorithm, rather than direct cross-correlation, as a way to increase efficiency. As alternatives to correlation of actual intensity values, Wang and Shung (1996) tested several bit-pattern correlation approaches that involved counting the number of matching pixels with coincident intensity characteristics such as sign or amplitude between sequential image samples. Sandrin et al. (2001) described a technique, referred to as ultrasonic speckle velocimetry, capable of achieving extremely high temporal resolution. However, this was limited to one velocity component and required a special transducer. Other approaches have used multiple transducers simultaneously to obtain multi-directional velocity components or even tried to use speckle pattern decorrelation as an indirect measure of fluid velocities (Bohs et al., 1995, Friemel et al., 1998; Jensen, 1996, 2000).

Crapper et al. (2000) described the direct application of PIV analysis software to ultrasound imaging of sediment-laden flow. Scan converted B-mode ultrasound images were acquired using a curvilinear array transducer and digitized at the limited frame rates available with videotape.

Work by our research group expanded the use of DPIV analysis principles to biomedical ultrasound imaging. In general, it cannot be assumed that ultrasound speckles will have a one-to-one correlation with the acoustic reflectors that generate them. Accordingly, our approach was described as digital ultrasound speckle image velocimetry (DUSIV) rather than digital ultrasound PIV. For brevity, we will henceforth refer to our implementation as ultrasound speckle image velocimetry (USIV). Simulated aortic blood flow was studied in a flow

phantom (Gharib and Beizaie, 2003) as well as *in vivo* left ventricular intracavitary flow in a porcine open-chest preparation (Lin et al., 2003). The latter experiments will be described further in Chapter 4. Ultrasound data was acquired in polar coordinates using a phased array transducer and, after scan conversion of the detected B-mode data, images were exported at native acquisition frame rates. FFT-based cross-correlation was then performed of the ultrasound speckle patterns in order to obtain displacements and velocities.

Kim, Hertzberg, and Shandas (2004) and Kim, Hertzberg, et al. (2004) tested a similar approach that was described as echo PIV. Their implementation differed slightly in that they used harmonic imaging and the FFT-based cross-correlations were performed on polar B-mode data without scan conversion. Rather than finding correlations over two orthogonal spatial dimensions, they performed correlations across the dimensions of axial position (on the vertical axis) and scan line number (on the horizontal axis). Delaying scan conversion until after performing cross-correlations was felt to decrease outliers, but meant that the final vector field resolution was spatially variant.

Sengupta et al. (2007) performed FFT-based cross-correlations on scan converted B-mode data from *in vivo* porcine left ventricular intracavitary flow. They referred to this approach as ultrasonic DPIV. The experimental results showed that altering the myocardial activation sequence through epicardial pacing led to changes in the intracavitary flow patterns during isovolumic contraction.

Hong et al. (2008) applied a similar approach, referred to as vector PIV, to *in vivo* left ventricular intracavitary flow in humans. They quantified vortical flow parameters in patients with abnormal left ventricular systolic function as well as controls with normal function. Statistically significant differences were noted in relation to the position, size, and strength of vortical structures seen during left ventricular filling.

E. Motivation and Objectives

Routine clinical assessment of blood flow velocities currently relies upon Doppler ultrasound techniques that are limited to providing a single velocity component along the axial direction of the ultrasound beam. Even for a simple and nearly linear flow, accurate measurements require optimal transducer alignment with the main flow direction. More complex multi-dimensional flows can only be interrogated in a limited fashion, often using relatively primitive visualization by color flow imaging.

There would be tremendous value in being able to routinely and accurately utilize noninvasive ultrasound imaging to obtain multiple flow velocity components simultaneously. Applications include furthering knowledge of basic cardiovascular pathophysiology as well as improving medical device design and understanding of device failure mechanisms. Specific examples that will be discussed in later sections include the role of low or oscillating shear stresses in the development of atherosclerosis and aortic aneurysms as well as the role of vortex ring formation in left ventricular filling.

While there has certainly been interest in using PIV techniques with ultrasound imaging, there is an incomplete understanding of the technical factors that affect accuracy when using acoustic, rather than optical, images. For our USIV implementation, we chose to utilize a commercially available ultrasound transducer and imaging platform so that our findings would be broadly applicable.

The first objective of the current project was to study USIV system performance and characteristics under controlled *in vitro* conditions. The second objective was to document the feasibility of the technique in specific experimental *in vivo* models relevant to cardiac and arterial fluid mechanics. The implications of these results for further development of the USIV technique will be discussed.

C h a p t e r 2

IN VITRO EXPERIMENTS: UNIFORM TRANSLATION OF SPECKLE PHANTOM

A. Introduction

We designed a series of experiments to allow systematic characterization of the ultrasound speckle image velocimetry (USIV) technique. The first group of experiments involved creating a gelatin phantom that was seeded with ultrasound-scattering targets. When imaged with an ultrasound system, this phantom created a textured speckle pattern. We created an experimental apparatus that allowed us to translate the speckle phantom at a variety of known constant velocities.

As discussed earlier, digital particle image velocimetry (DPIV) is a well-characterized technique for fluid flow velocity measurements. There is a robust body of relevant literature and various refinements to the algorithms have been introduced in order to achieve improved accuracy. USIV is conceptually very similar to DPIV, in that images are acquired at known time intervals and local intensity patterns within images are tracked frame-to-frame in order to estimate displacements of the underlying fluid elements.

There are fundamental differences, however, in the nature of how these images are produced and, therefore, what factors will affect the image pattern characteristics. DPIV relies upon optical images produced using transient laser sheet illumination of a particle-seeded fluid medium. USIV relies upon images reconstructed from multiple ultrasound scan line acquisitions. Accordingly, USIV results will be dependent upon transducer and environmental characteristics that affect the quality of ultrasound imaging. While some researchers have explored tracking ultrasound speckle patterns to obtain fluid flow velocities (as discussed in Section 1.D.4), there have been multiple implementation variations and our understanding of the technical factors affecting USIV accuracy is incomplete.

The objective of this set of experiments was to perform a validation of the USIV technique and characterize the most relevant parameters affecting accuracy. We sought to compare velocity measurements by USIV against the known velocities that the speckle phantom was being moved by during each of the experiments. These experiments were performed for different combinations of transducer and image acquisition parameters.

B. Methods

1. Speckle Phantom Construction

We created a speckle phantom by suspending 120 mg of fluorescent polymer spheres (80 μm average diameter, Eastman Kodak Company, Rochester, NY) in 750 mL of consumer-grade gelatin solution (Knox Gelatine, Kraft Foods Group, Northfield, IL). The suspension was used to fill a flat molded plastic flask and then kept refrigerated in gel form throughout all experiments so that there would be no relative motion between particles during phantom displacements. The small polymer spheres acted as ultrasound-scattering particles during imaging. While several phantoms were made with different particle concentrations, the one described above was chosen because preliminary testing revealed the most satisfactory speckle pattern formation for tracking.

2. Linear Translation Apparatus

We created an experimental apparatus to allow us to translate the speckle phantom at constant linear velocities. To do so, we fabricated a metal specimen platform that was secured to a linear traverse connected to a stepper motor (Bodine HY-Sync AC Synchronous/DC Stepping Motor Type 23T3BEHH, Bodine Electric Company, Chicago, IL). The motor was driven using a Velmex 8300 Series controller (Velmex, Inc., East Bloomfield, NY). A photograph of the setup is shown in Figure 2-1.

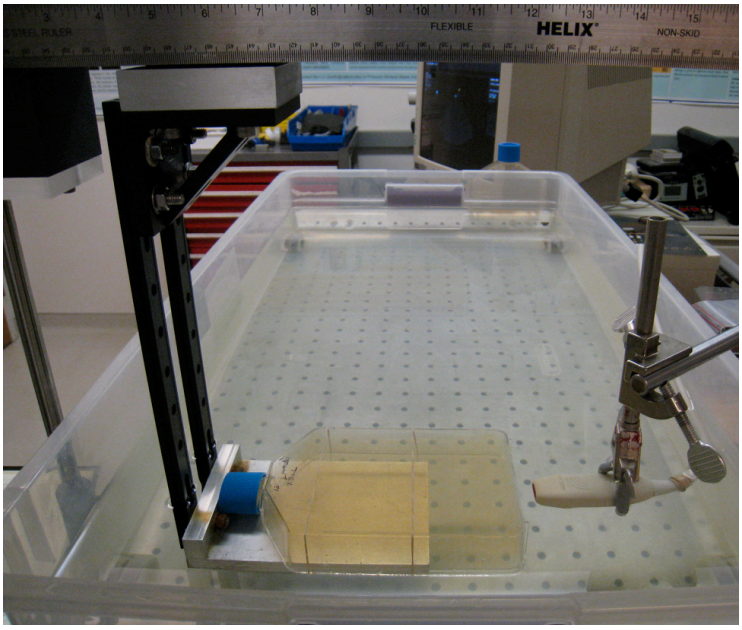

Figure 2-1. Experimental setup for linear translation of speckle phantom. In this photograph, the apparatus is configured for axial translation of the phantom towards and away from the ultrasound transducer (flat phased array transducer is shown).

During imaging sessions, the speckle phantom was securely fixed to the specimen platform. The ultrasound transducer was positioned to allow full field imaging during horizontal motion. Linear translations were performed at constant velocities of either 2 or 4 cm/sec. These reference speeds were confirmed using a ruler mounted to the linear traverse.

3. Ultrasound Imaging

B-mode images were obtained using a General Electric (GE) Vingmed System FiVe ultrasound machine (GE Vingmed Ultrasound, Horten, Norway). A 2D flat phased array transducer (with beam steering) was used with center frequency at 10 MHz for various acquisitions at approximately 83 frames/sec.

Ultrasound acquisition and experimental parameters were varied in order to test their respective influences on the accuracy of USIV results. These included transducer focal depth as well as translational velocity direction and magnitude.

We also obtained images at various known displacements from the starting position and planned to estimate these displacements by USIV analysis of static images (without moving scatterers). However, even for displacements as small as 0.25 cm, there was too much decorrelation of the speckle patterns for this to be feasible.

The relevant parameter options that were actually analyzed are summarized in Table 2-1. The specific combinations of imaging and experimental parameters that were used for each test case are listed in Table 2-2.

Transducer type	Flat phased array
Image depth (frame rate)	10 cm (83.3 frames/sec)
Focal depth	3, 5 or 7 cm
Translational direction	Towards left or right within imaging field
Velocity magnitude	2 or 4 cm/sec

Table 2-1. List of ultrasound acquisition and experimental parameters that were used for uniform translation experiments.

4. USIV Analysis

B-mode ultrasound cineloop files in Digital Imaging and Communications in Medicine (DICOM) format were converted to sequenced individual bitmap images using EchoMAT software version 2.0 (GE Vingmed Ultrasound, Horten, Norway). This script was used with MATLAB software version 5.3 (The MathWorks, Inc., Natick, MA). Processing included scan conversion of the image scan line data from polar coordinates (as initially acquired by the phased array transducer) to Cartesian coordinates for further analysis.

Test Case	Transducer	Image Depth (Frame Rate)	Focal Depth	Horizontal Translation Velocity Magnitude	Direction
1	FPA	10 cm (83.3 fps)	3 cm	2 cm/sec	Left
2	FPA	10 cm (83.3 fps)	3 cm	2 cm/sec	Right
3	FPA	10 cm (83.3 fps)	5 cm	2 cm/sec	Left
4	FPA	10 cm (83.3 fps)	5 cm	2 cm/sec	Right
5	FPA	10 cm (83.3 fps)	7 cm	2 cm/sec	Left
6	FPA	10 cm (83.3 fps)	7 cm	2 cm/sec	Right
7	FPA	10 cm (83.3 fps)	3 cm	4 cm/sec	Left
8	FPA	10 cm (83.3 fps)	3 cm	4 cm/sec	Right
9	FPA	10 cm (83.3 fps)	5 cm	4 cm/sec	Left
10	FPA	10 cm (83.3 fps)	5 cm	4 cm/sec	Right
11	FPA	10 cm (83.3 fps)	7 cm	4 cm/sec	Left
12	FPA	10 cm (83.3 fps)	7 cm	4 cm/sec	Right

Table 2-2. Combinations of imaging and experimental parameters used for specific test cases studied in uniform translation experiments. Abbreviations: FPA (flat phased array), fps (frames per second).

The scan converted images were imported into a particle image velocimetry (PIV) software package for further analysis (PIVview version 3.6, PIVTEC, Gottingen, Germany). Each ultrasound frame was acquired during a 12 ms time interval (corresponding to 83.3 fps), but image pairs were chosen to optimize the interframe displacements (relative to sampling window dimensions) and make them similar for both translation speeds tested. The interframe time intervals used were 48 ms for 2 cm/sec and 24 ms for 4 cm/sec translations. An image mask was used to exclude regions outside of the ultrasound image field

from the analyses. Displacement and velocity vectors were calculated using a Fast Fourier Transform (FFT)-based cross-correlation algorithm. Multi-pass interrogation with window shifting was performed using 32 x 32 pixel sampling windows (corresponding to a physical window size of approximately 0.50 x 0.50 cm). The step size was 32 x 32 pixels. Correlation peaks were detected using a three-point Gaussian fit and outlier detection (without removal, interpolation, or smoothing) was performed after each pass. Further details regarding these procedures can be found in Willert and Gharib (1991), Westerweel et al. (1997), and Raffel et al. (2007). Instantaneous velocities, time-averaged velocities, and the mean of the time-averaged velocities within a central region of interest (in order to avoid edge artifacts) were calculated.

C. Results

A representative frame from ultrasound imaging is shown in Figure 2-2. The effective spatial resolution of the ultrasound speckle image is better in the near-field (closer to the transducer at the top of the image) than in the far-field (further away from the transducer). Throughout the image, there appears to be a transition in spatial resolution near the focal depth along every individual axial beam direction.

The representative frame from Figure 2-2 is combined with a subsequently acquired frame into a “double exposure” composite image that is shown in Figure 2-3. This composite image allows visualization of the interframe displacement of speckle patterns. In the near-field, the translation of individual speckles can easily be seen. In the far-field, the speckle patterns from the initial frame appear horizontally “smeared,” reflecting the decreased spatial resolution and increased difficulty in discerning individual intensity peaks in that region.

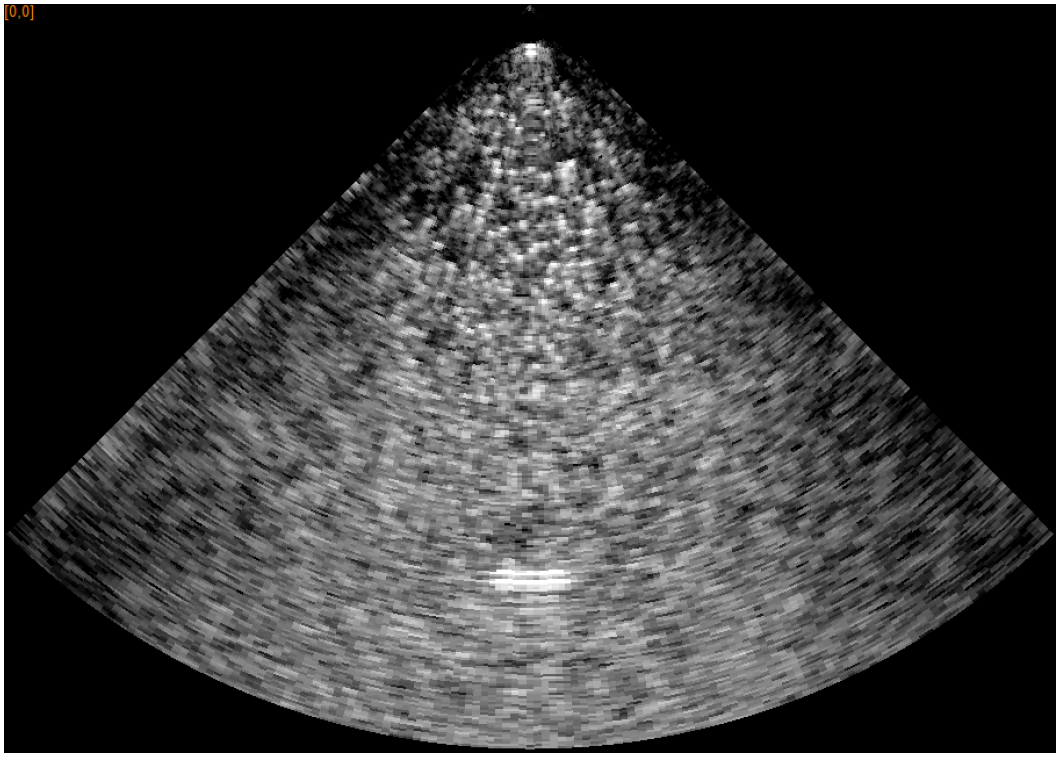

Figure 2-2. Example of exported frame from ultrasound imaging used for USIV processing. Image depth was 10 cm, focal depth was 5 cm, and horizontal translation velocity was 2 cm/sec in this case. Ultrasound transducer and near-field region are towards the top of the image.

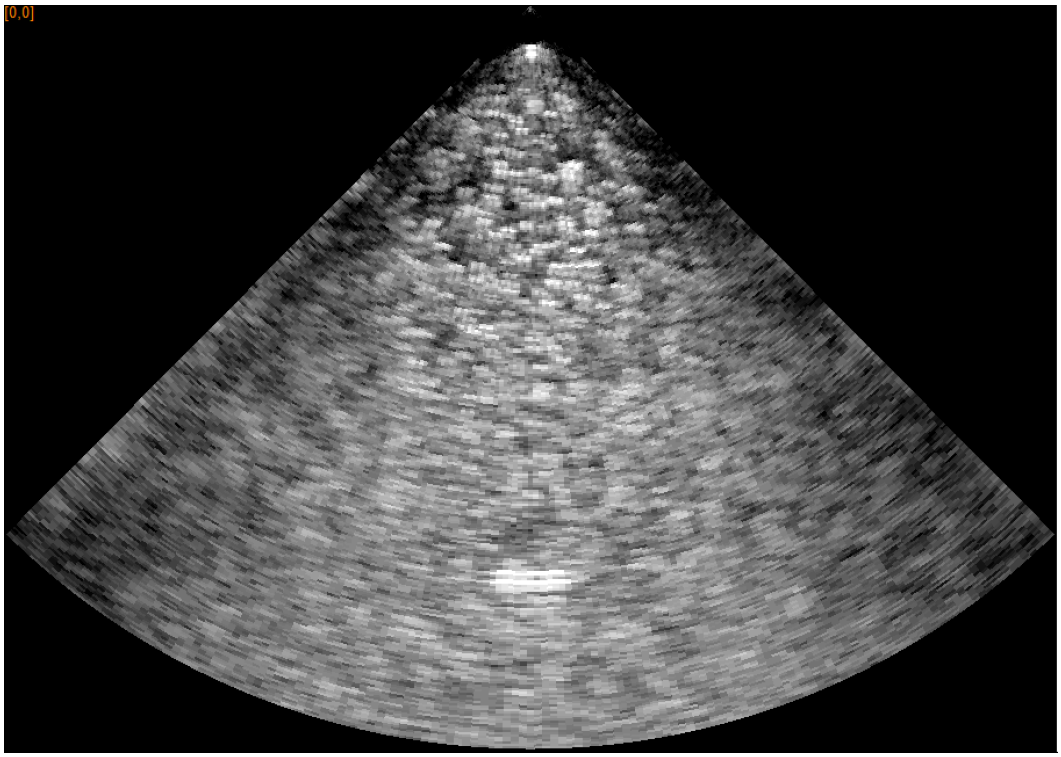

Figure 2-3. Example of "double exposure" composite image that allows visualization of the interframe displacement of speckle patterns. Image depth was 10 cm, focal depth was 5 cm, translation velocity was 2 cm/sec, and interframe time interval was 48 ms in this case.

Representative examples of instantaneous velocity fields obtained with USIV are shown below. Figures 2-4 and 2-5 show velocity fields from experiments where horizontal translation was performed at 2 cm/sec to the right and to the left, respectively. Figures 2-6 and 2-7 show velocity fields from experiments where horizontal translation was performed at 4 cm/sec to the right and to the left, respectively.

Overall, the velocity fields were fairly uniform (especially with lower speed motion) and the velocity magnitudes were clustered around the expected values. Several types of spatial variation, however, were commonly seen. Randomly located outlier vectors could be seen with spurious directions and

magnitudes, especially with higher speed motion. In addition, some vectors appeared to have systematic biases that were different depending on their locations either along the edges of the image or away from the edges. Each of these sources of error will be further explored in the Discussion section below.

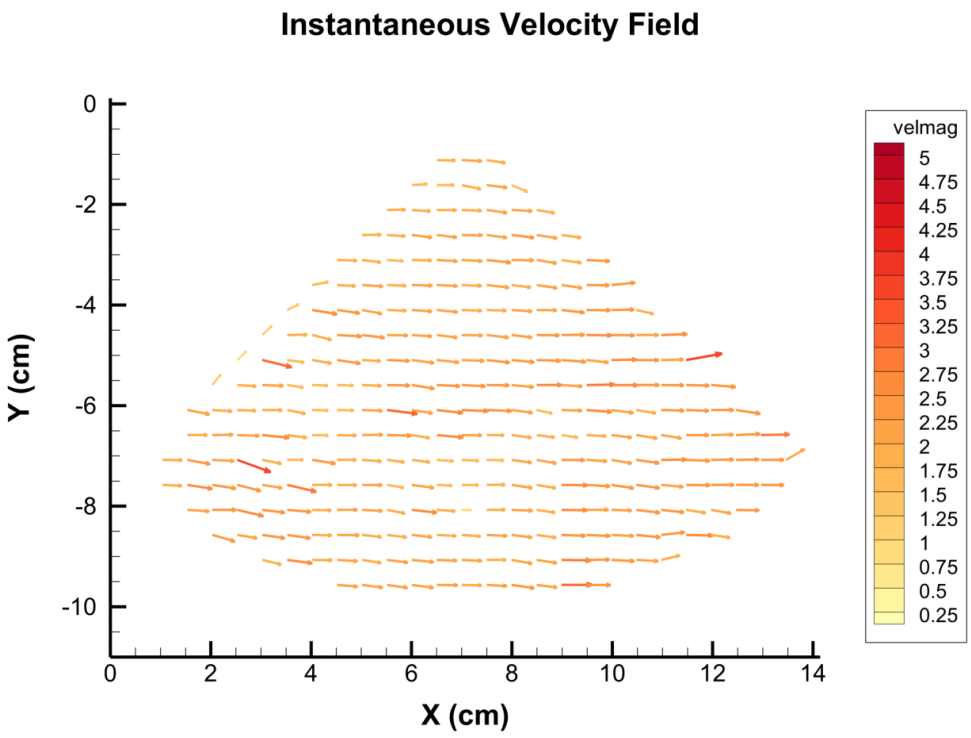

Figure 2-4. Representative example showing instantaneous velocity field measurements for horizontal translation to the right at 2 cm/sec. Image depth was 10 cm, focal depth was 5 cm, and interframe time interval was 48 ms in this case.

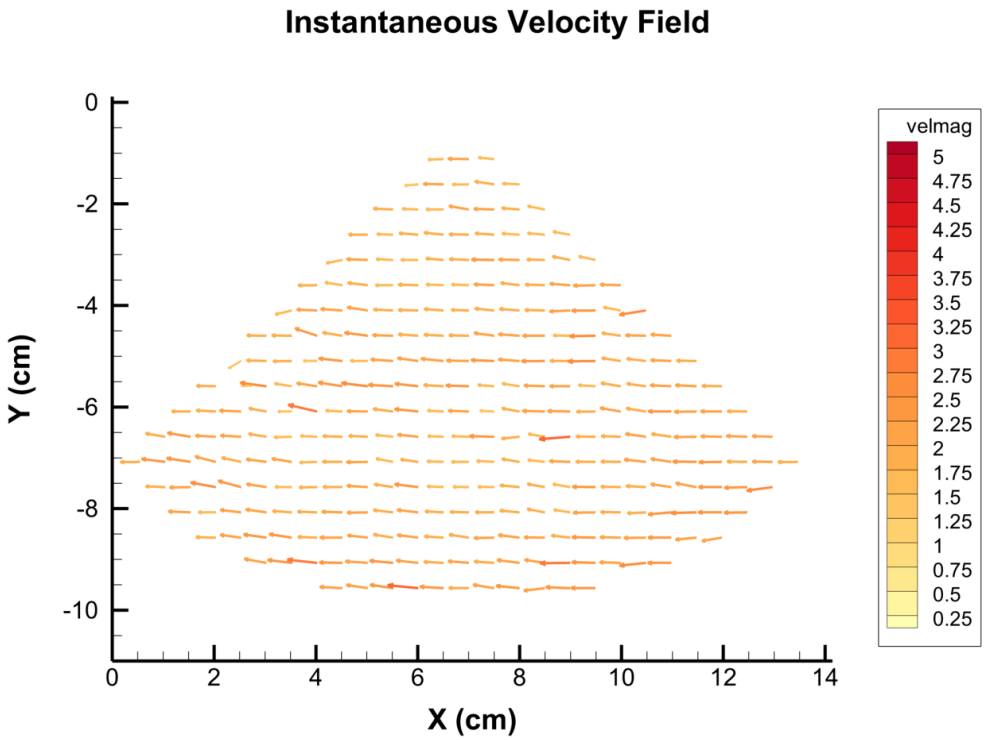

Figure 2-5. Representative example showing instantaneous velocity field measurements for horizontal translation to the left at 2 cm/sec. Image depth was 10 cm, focal depth was 5 cm, and interframe time interval was 48 ms in this case.

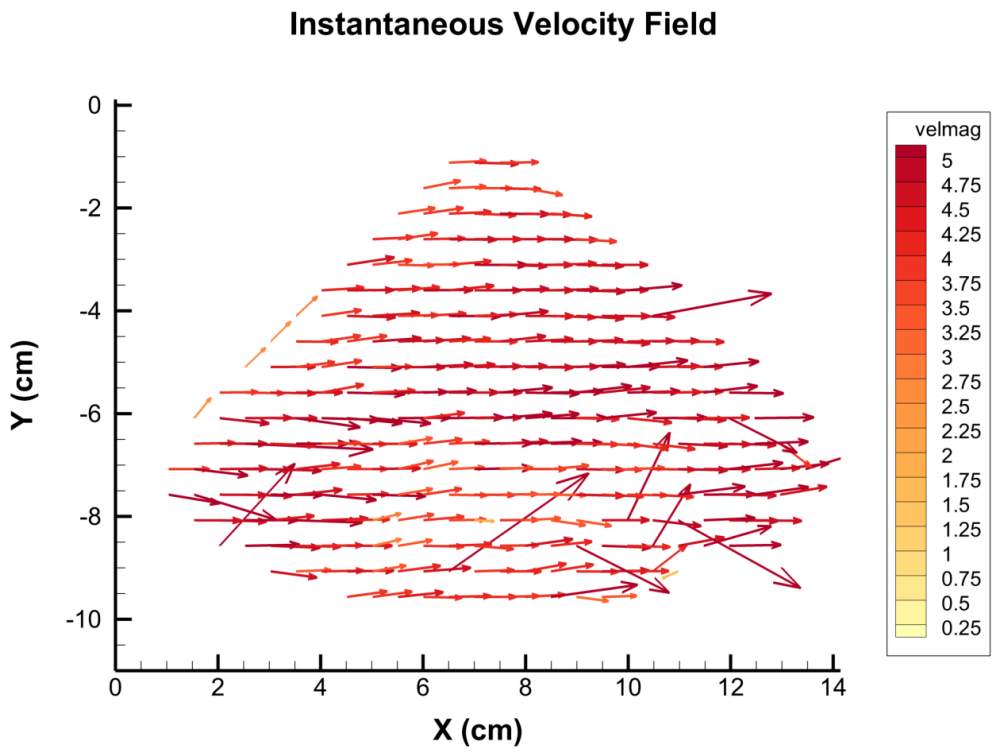

Figure 2-6. Representative example showing instantaneous velocity field measurements for horizontal translation to the right at 4 cm/sec. Image depth was 10 cm, focal depth was 5 cm, and interframe time interval was 24 ms in this case.

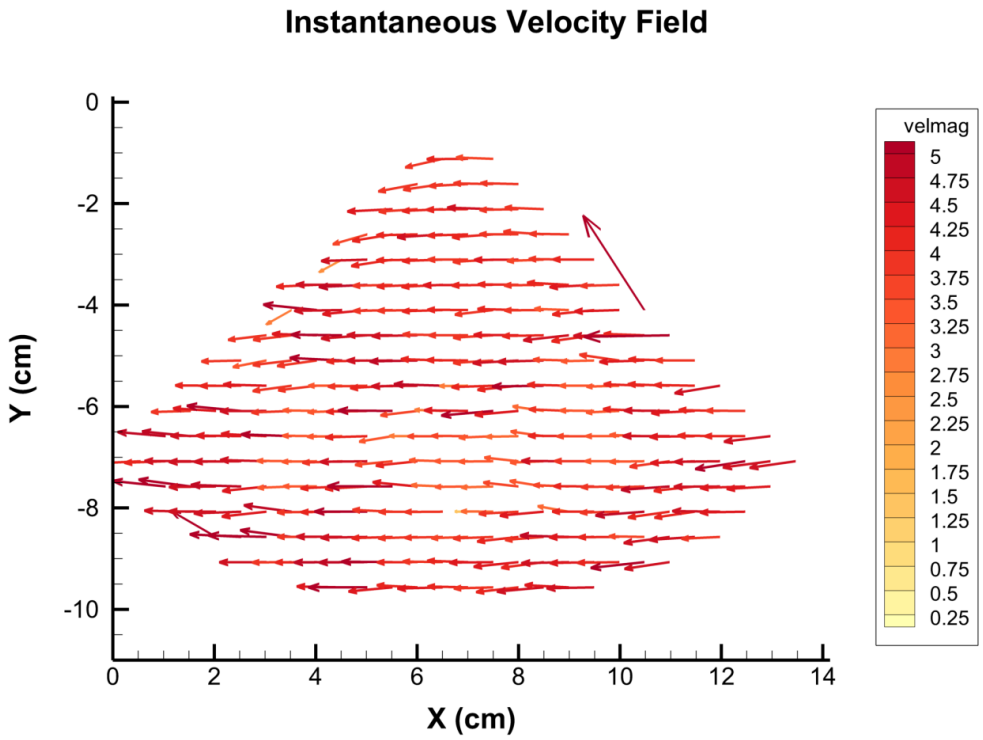

Figure 2-7. Representative example showing instantaneous velocity field measurements for horizontal translation to the left at 4 cm/sec. Image depth was 10 cm, focal depth was 5 cm, and interframe time interval was 24 ms in this case.

Representative examples of time-averaged velocity fields (within a central region of interest) obtained with USIV are shown below. Figures 2-8 and 2-9 show velocity fields from experiments where horizontal translation was performed at 2 cm/sec to the right and to the left, respectively. Figures 2-10 and 2-11 show velocity fields from experiments where horizontal translation was performed at 4 cm/sec to the right and to the left, respectively.

Overall, the time-averaged velocity fields were highly uniform (especially with lower speed motion) and the velocity magnitudes were clustered around the expected values. Some minor spatial variation was still seen after the averaging operations, though, primarily near the region where the images had stationary

reverberation artifacts. This source of error will be further explored in the Discussion section below.

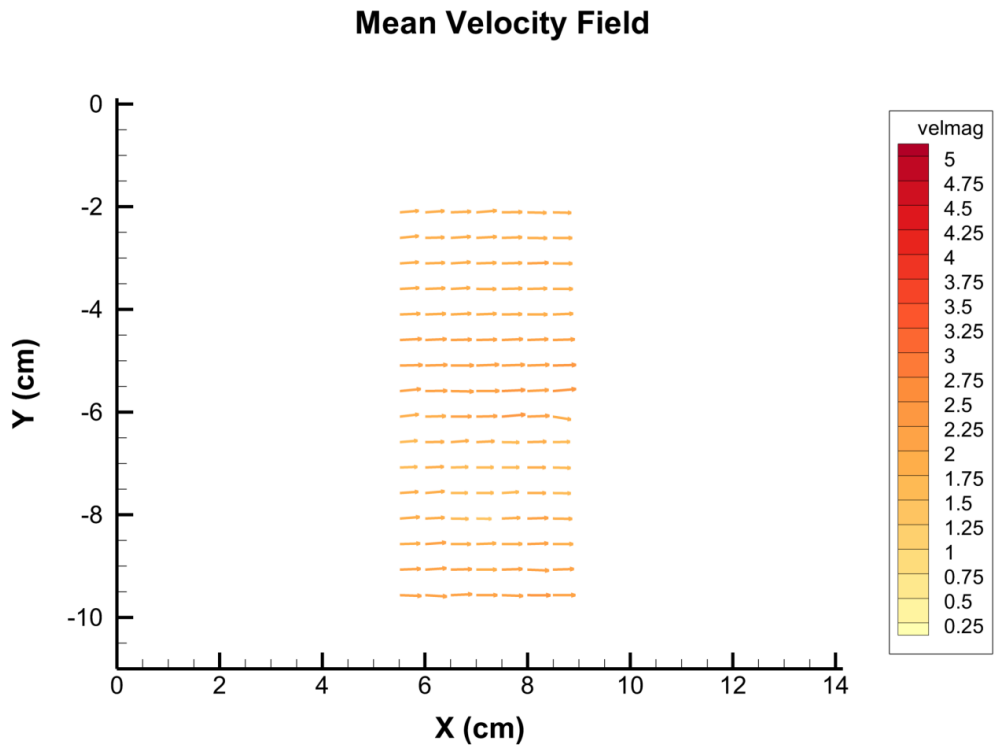

Figure 2-8. Representative example showing time-averaged velocity field measurements for horizontal translation to the right at 2 cm/sec. Image depth was 10 cm, focal depth was 5 cm, and interframe time interval was 48 ms in this case.

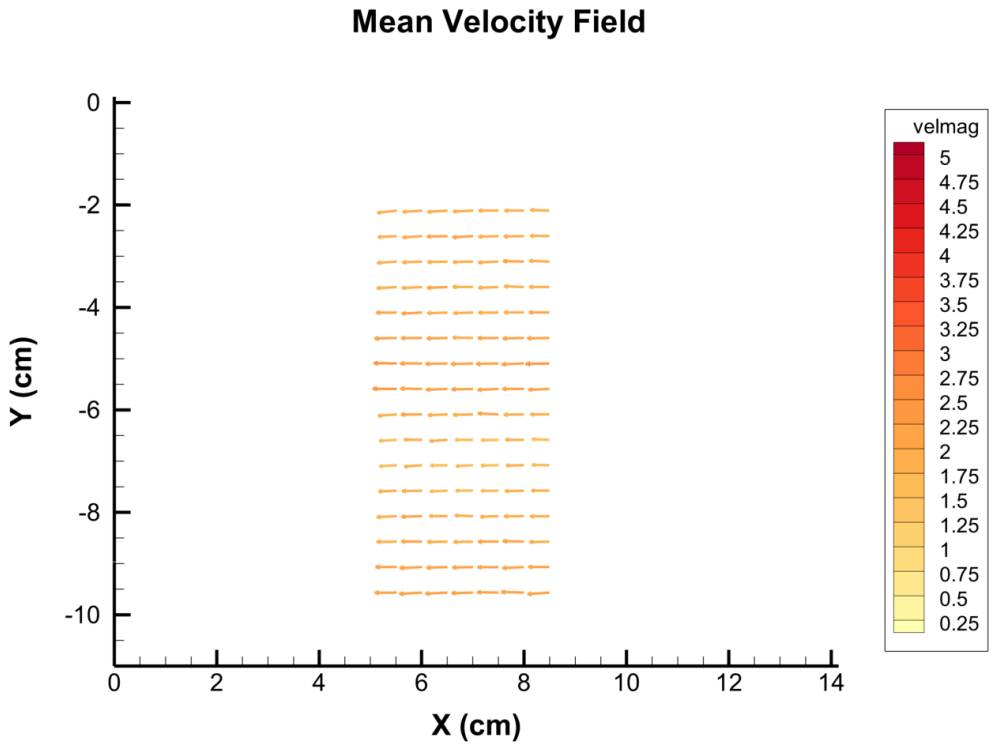

Figure 2-9. Representative example showing time-averaged velocity field measurements for horizontal translation to the left at 2 cm/sec. Image depth was 10 cm, focal depth was 5 cm, and interframe time interval was 48 ms in this case.

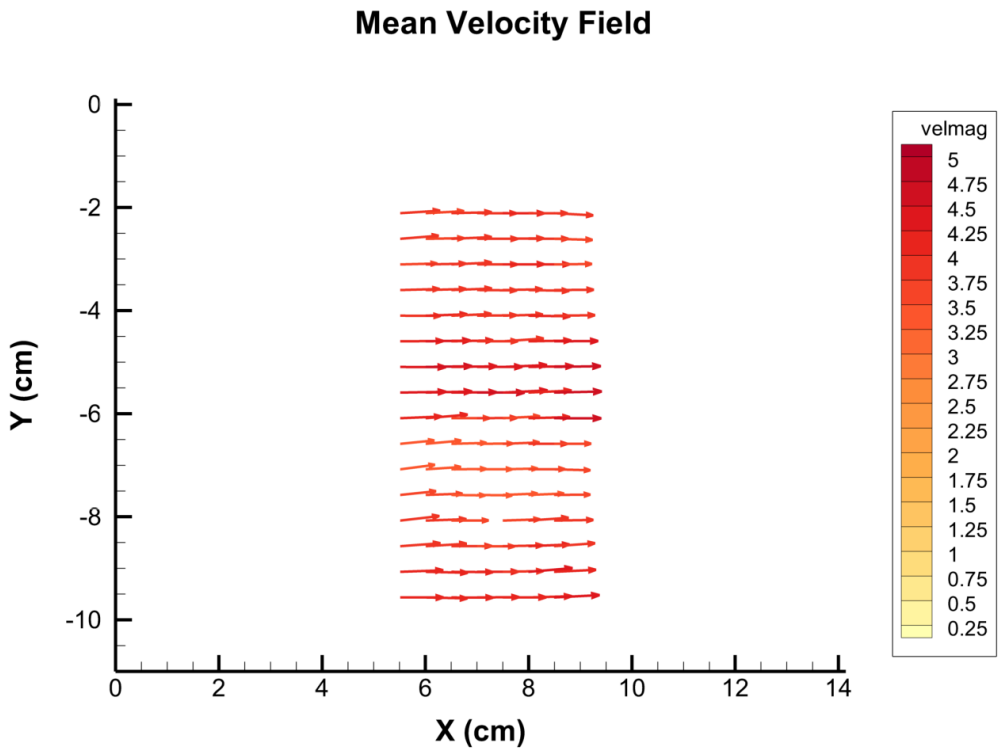

Figure 2-10. Representative example showing time-averaged velocity field measurements for horizontal translation to the right at 4 cm/sec. Image depth was 10 cm, focal depth was 5 cm, and interframe time interval was 24 ms in this case.

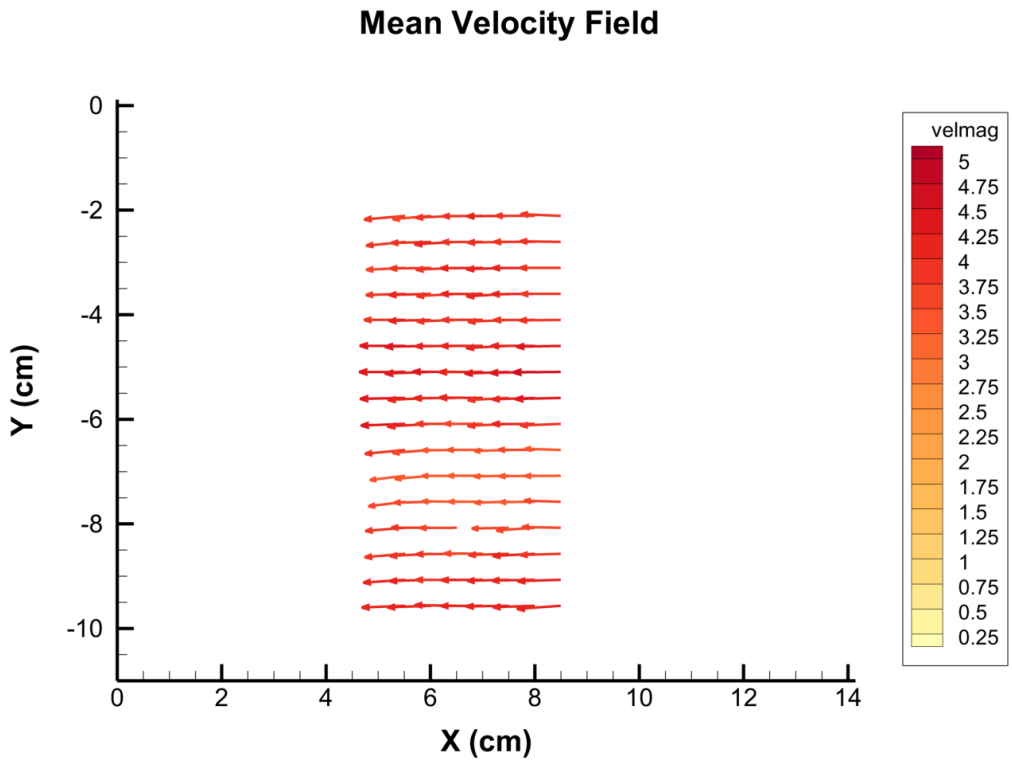

Figure 2-11. Representative example showing time-averaged velocity field measurements for horizontal translation to the left at 4 cm/sec. Image depth was 10 cm, focal depth was 5 cm, and interframe time interval was 24 ms in this case.

Mean time-averaged horizontal and vertical velocity measurements (with standard deviations and error percentages) over the central region of interest for each test case are listed in Table 2-3 and described in the following paragraphs. The mean time-averaged horizontal velocity measurements are also shown in graphical form in Figure 2-12.

Test Case	Focal Depth	Horizontal Translation Velocity Magnitude	L/R	Horizontal Velocity with SD (cm/sec)	Horizontal Velocity Magnitude Error	Vertical Velocity with SD (cm/sec)
1	3 cm	2 cm/sec	L	-2.14 ± 0.18	7.0 %	-0.04 ± 0.13
2	3 cm	2 cm/sec	R	2.15 ± 0.21	7.5 %	0.03 ± 0.09
3	5 cm	2 cm/sec	L	-1.97 ± 0.15	-1.5 %	-0.04 ± 0.06
4	5 cm	2 cm/sec	R	1.96 ± 0.16	-2.0 %	0.05 ± 0.07
5	7 cm	2 cm/sec	L	-1.89 ± 0.14	-5.5 %	-0.04 ± 0.07
6	7 cm	2 cm/sec	R	1.90 ± 0.14	-5.0 %	0.01 ± 0.07
7	3 cm	4 cm/sec	L	-4.44 ± 0.50	11.0 %	-0.06 ± 0.16
8	3 cm	4 cm/sec	R	4.27 ± 0.38	6.8 %	0.15 ± 0.13
9	5 cm	4 cm/sec	L	-3.92 ± 0.29	-2.0 %	-0.09 ± 0.12
10	5 cm	4 cm/sec	R	3.93 ± 0.32	-1.8 %	0.09 ± 0.12
11	7 cm	4 cm/sec	L	-3.80 ± 0.27	-5.0 %	-0.08 ± 0.12
12	7 cm	4 cm/sec	R	3.74 ± 0.30	-6.5 %	0.12 ± 0.14

Table 2-3. Mean time-averaged horizontal and vertical velocity measurements over central region of interest for various test cases. Abbreviations: L (left), R (right), SD (standard deviation).

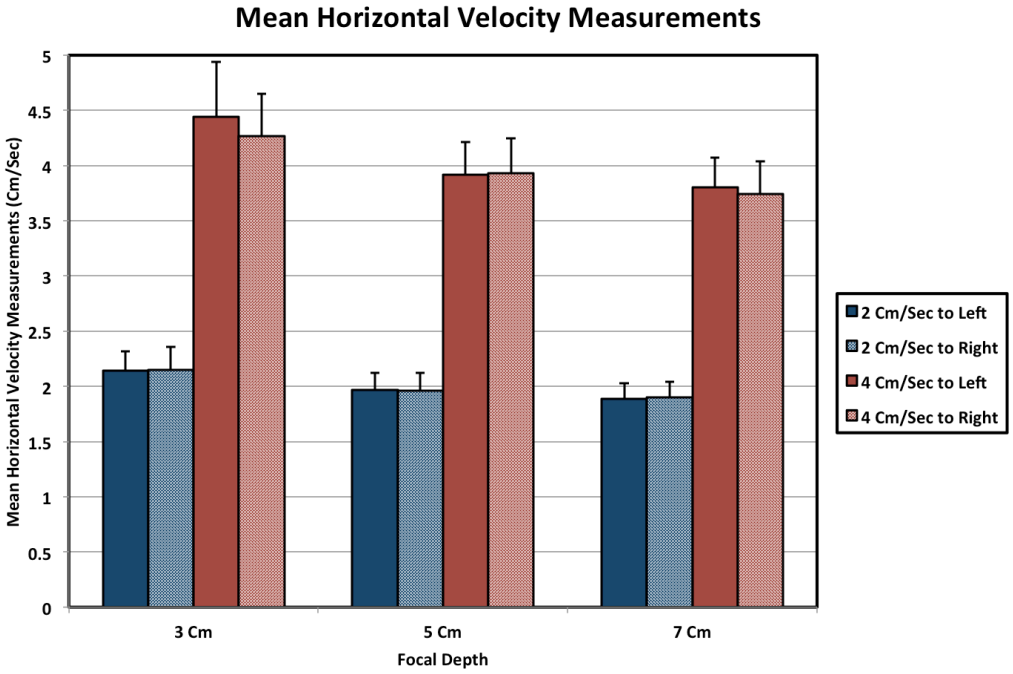

Figure 2-12. Mean time-averaged horizontal velocity measurements over central region of interest for various test cases. Error bars indicate standard deviation.

Mean time-averaged horizontal velocity measurements varied with focal depth (for a constant image depth of 10 cm) and were closest to the reference velocities when the focal depth was 5 cm. At this setting, the magnitude errors were small and measurements showed little difference whether the translation occurred towards the left or the right of the image. For a horizontal translation velocity magnitude of 2 cm/sec, the mean horizontal velocity measurements (and standard deviations) to the left and right were -1.97 ± 0.15 and 1.96 ± 0.16 cm/sec, respectively. The magnitude errors were -1.5 and -2.0%, respectively. For a horizontal translation velocity magnitude of 4 cm/sec, the mean horizontal velocity measurements (and standard deviations) to the left and right were -3.92 ± 0.29 and 3.93 ± 0.32 cm/sec, respectively. The magnitude errors were -2.0 and -1.8%, respectively.

When the focal depth was 7 cm (towards the bottom of these images and further from the transducer), there was a slightly increased systematic underestimation of velocities. For a horizontal translation velocity magnitude of 2 cm/sec, the mean horizontal velocity measurements (and standard deviations) to the left and right were -1.89 ± 0.14 and 1.90 ± 0.14 cm/sec, respectively. The magnitude errors were -5.5 and -5.0%, respectively. For a horizontal translation velocity magnitude of 4 cm/sec, the mean horizontal velocity measurements (and standard deviations) to the left and right were -3.80 ± 0.27 and 3.74 ± 0.30 cm/sec, respectively. The magnitude errors were -5.0 and -6.5%, respectively.

When the focal depth was 3 cm (towards the top of these images and closer to the transducer), there was a mild systematic overestimation of velocities. For a horizontal translation velocity magnitude of 2 cm/sec, the mean horizontal velocity measurements (and standard deviations) to the left and right were -2.14 ± 0.18 and 2.15 ± 0.21 cm/sec, respectively. The magnitude errors were 7.0 and 7.5%, respectively. For a horizontal translation velocity magnitude of 4 cm/sec, the mean horizontal velocity measurements (and standard deviations) to the left and right were -4.44 ± 0.50 and 4.27 ± 0.38 cm/sec, respectively. The magnitude errors were 11.0 and 6.8%, respectively.

D. Discussion

Instantaneous velocity fields generally showed good agreement with the expected reference velocity values. More randomly located outliers were seen for the 4 cm/sec compared with 2 cm/sec experiments, however. Since the expected displacements were made equal by adjusting interframe time intervals, the number of speckles lost from the imaging plane or interrogation window should also have been roughly equal. The ultrasound beam sweep speed, though, remained the same. Therefore, the higher number of outliers was most likely due to increased speckle pattern decorrelation at the increased translation velocity

(relative to the constant beam sweep speed). This is a source of potential error that is unique to USIV as compared to DPIV.

In certain regions of the image field, some of the calculated vectors seemed to have systematic biases. The most prominent of these were related to the stationary reverberation artifacts in the middle of the image field for these experiments (as can be seen in Figure 2.2). This created strong correlation peaks for small but non-zero displacements outside of the self-correlation detection threshold (2.0 pixels for these analyses). Correlation peaks from the true displacements within those interrogation windows were also degraded due to masking of the speckle patterns by the stationary image artifacts. This is an error that can affect DPIV processing as well, but may be more common with certain ultrasound imaging arrangements that could be used with USIV.

Errors were sometimes seen near the borders of the image field where velocity vectors were spuriously directed almost parallel to the image mask. These artifactual vectors are easily seen in Figures 2-4 and 2-6 and are likely similar in origin to known errors that can occur when performing DPIV analyses near walls or interfaces (Theunissen et al., 2008).

Occasionally, a small vertical bias was seen for vectors throughout an instantaneous velocity field. This appeared to be related to small vertical oscillations of the apparatus as it was translated horizontally. Obviously, this type of confounding factor could influence instantaneous measurements for both USIV and DPIV, but would not be expected to have a significant effect on time-averaged velocity results.

For calculation of time-averaged horizontal velocities, a central rectangular region of interest was chosen for the analyses in order to avoid influence from edge artifacts. A systematic bias remained towards velocity underestimation in the portion of the image field with stationary reverberation artifacts. Overall, though, the time-averaged horizontal velocity fields within these regions showed very good agreement with the reference velocity values.

Mean time-averaged horizontal velocity measurements were calculated within the central region of interest. For the 10 cm image depth used in these experiments, agreement with the reference horizontal velocities was excellent (magnitudes underestimated by 2.0% or less) when the focal depth was set at 5 cm. There was an interesting and consistent dependence on focal depth seen for the 2 cm/sec as well as 4 cm/sec experiments. In both sets of experiments, shifting the focal depth further away (to 7 cm from the transducer) slightly increased the magnitude of underestimation to 5.0-6.5%. However, shifting the focal depth closer (to 3 cm from the transducer) led to a larger change with the magnitudes now overestimated by 6.8-11.0%. Changing the focal depth setting clearly alters the spatially variant point spread function throughout the image. This can be seen subjectively when visualizing images acquired with different focal depths. Our results suggest that, for a given ultrasound imaging arrangement, there likely exists an optimal focal depth allowing for the most accurate overall velocity estimations throughout the central region of the image field.

For a couple of test cases (specifically 4 cm/sec translation with focal depths of either 3 cm or 7 cm), a small difference was seen between velocity magnitude estimates depending on whether the translation was towards the left or right of the image. Since this trend was not consistently seen for all test cases, it was most likely due to experimental variation in the setting of increased speckle pattern decorrelation at the higher translation speed. However, there is an important theoretical explanation that should be considered that involves the relative motion of particles with respect to the transducer orientation.

This potential error can be explained by considering the difference between optical image acquisitions and the reconstruction of ultrasound images from backscattered signals. All regions within optical images are acquired simultaneously. Furthermore, optical DPIV images can be considered to be instantaneous acquisitions since the laser sheet pulses are so short. After a particle image displacement vector $\Delta\mathbf{s}$ is estimated, the associated average velocity vector

$\mathbf{v}$ can be calculated by using the known temporal offset Δt between successive laser pulses as shown in Equation (2.1).

$$\mathbf{v} = \frac{\Delta \mathbf{s}}{\Delta t} \tag{2.1}$$

The situation is different for reconstructed ultrasound images. For a typical two-dimensional image, the ultrasound beam is swept sequentially from one side of the image field to the other. For a linear array transducer, this leads to a set of parallel scan lines that are acquired with a temporal offset between each that is dependent upon the sweep speed. For a phased array transducer, these scan lines originate from a common origin and are arranged in a polar coordinate system. The sweep speed is primarily dependent upon the time it takes for an ultrasound pulse to travel the distance to and from the maximum depth of the image.

For the current implementation of USIV, we calculate velocities using a similar basic approach as for DPIV. Specifically, Equation (2.1) is also used for USIV, but now the denominator is estimated using

$$\Delta t = \frac{1}{FR} \ , \tag{2.2}$$

where FR is the ultrasound imaging frame rate in Hz.

Equation (2.2) does not account for the fact that speckle patterns within an ultrasound image are obtained sequentially rather than simultaneously. The true temporal offset between the two instances when a speckle pattern is imaged in consecutive ultrasound frames depends upon the timing with which incident ultrasound beams from each respective frame acquisition encounter the relevant scatterers. If we assume that the ultrasound beam sweeps the image field in a unidirectional manner (e.g., from left to right), then the true temporal offset will vary depending on whether a speckle pattern is displayed closer or farther from the initial (i.e., leftmost) scan line in the second frame.

For example, a speckle pattern that is displayed further *towards the right* in the second frame than in the first frame will have been imaged at a time that is equal to the frame rate-derived temporal offset with an additional delay. This delay is due to the time required to obtain additional scan lines before the swept ultrasound beam encounters the scatterers at their new lateral position. If, instead, there has been relative lateral motion *towards the left* between frames, then the true temporal offset will be less than that derived from the overall frame rate.

The true temporal offset will also vary due to changes in the relative axial position (or axial distance from the transducer) between successive frames, although this effect will be small since the axial time correction will never be greater than the time it takes to acquire a single scan line.

Accordingly, the true temporal offset is actually

$$\Delta t_{true} = \frac{1}{FR} + \Delta t_{corr} \ . \tag{2.3}$$

The correction term Δt_{corr} can be expressed in terms of contributions from changes in either the lateral or axial positions between images as

$$\Delta t_{corr} = \Delta t_{lateral} + \Delta t_{axial} \ . \tag{2.4}$$

We can note that

$$\Delta \mathbf{s} = \mathbf{s}_2 - \mathbf{s}_1 \ , \tag{2.5}$$

where $\mathbf{s}_1$ and $\mathbf{s}_2$ are position vectors for the center of a given speckle pattern in successive frames. In Cartesian coordinates,

$$\begin{gathered} \mathbf{s}_1 = x_1\hat{\mathbf{x}} + y_1\hat{\mathbf{y}} \\ \text{and } \mathbf{s}_2 = x_2\hat{\mathbf{x}} + y_2\hat{\mathbf{y}} \ , \end{gathered} \tag{2.6}$$

where $\hat{\mathbf{x}}$ and $\hat{\mathbf{y}}$ are unit vectors for the horizontal and vertical axes, respectively. The displacement $\Delta\mathbf{s}$ can be represented in vector form as

$$\begin{aligned} \Delta\mathbf{s} &= \Delta x\hat{\mathbf{x}} + \Delta y\hat{\mathbf{y}} \\ &= (x_2 - x_1)\hat{\mathbf{x}} + (y_2 - y_1)\hat{\mathbf{y}} \ . \end{aligned} \tag{2.7}$$

The positive x-axis points in the direction of the ultrasound beam sweep (e.g., horizontally to the right) and the positive y-axis points in the direction of increasing depth from the transducer.

For a linear array transducer, the temporal correction term can then be written as

$$\begin{aligned} \Delta t_{corr} &= \Delta t_{lateral} + \Delta t_{axial} \\ &= \frac{\Delta x}{\sigma_x} + \frac{\Delta y}{c} \ , \end{aligned} \tag{2.8}$$

where σ_x is the ultrasound beam lateral sweep speed and c is the speed of sound in water (which determines the transit time for any given axial length). Both σ_x and c use m/sec as the units of measurement.

The position vectors $\mathbf{s}_1$ and $\mathbf{s}_2$ can, alternatively, be described in polar coordinates as

$$\begin{aligned} \mathbf{s}_1 &= (r_1, \theta_1) \\ &= (\sqrt{x_1^2 + y_1^2}, \tan^{-1}\left\{\frac{x_1}{y_1}\right\}) \\ \text{and } \mathbf{s}_2 &= (r_2, \theta_2) \\ &= (\sqrt{x_2^2 + y_2^2}, \tan^{-1}\left\{\frac{x_2}{y_2}\right\}) \ . \end{aligned} \tag{2.9}$$

The origin is assigned to the point in the image plane that corresponds to the center of the transducer face. As defined earlier, the positive y-axis points in the direction of increasing depth from the transducer. θ is defined as zero along the positive y-axis and as positive in the direction of the ultrasound beam sweep (defined earlier as the positive x-direction).

The displacement $\Delta\mathbf{s}$ can then be described as changes in scalar polar coordinates using

$$\begin{aligned} \Delta r &= r_2 - r_1 \\ &= \sqrt{x_2^2 + y_2^2} - \sqrt{x_1^2 + y_1^2} \\ \text{and } \Delta\theta &= \theta_2 - \theta_1 \\ &= \tan^{-1}\left\{\frac{x_2}{y_2}\right\} - \tan^{-1}\left\{\frac{x_1}{y_1}\right\} . \end{aligned} \tag{2.10}$$

For a phased array transducer, the temporal correction term is most easily described using polar variables as

$$\begin{aligned} \Delta t_{corr} &= \Delta t_{lateral} + \Delta t_{axial} \\ &= \frac{\Delta\theta}{\sigma_\theta} + \frac{\Delta r}{c} , \end{aligned} \tag{2.11}$$

where σ_θ is the ultrasound beam sweep speed (in radians/sec for this type of transducer) and c is again the speed of sound in water (in m/sec).

For a fixed transducer orientation, reversing the horizontal flow direction will reverse the sign of the temporal error. In other words, using an interframe time interval calculated only from the frame rate (without the Δt_{corr} term) will either overestimate or underestimate the true velocity depending on whether the particles have a velocity component aligned with or opposite to the beam sweep direction, respectively. With a phased (rather than linear) array transducer, the magnitude (but not the sign) of the error for a horizontal flow will be spatially variant. This is because a linear horizontal displacement Δx will correspond to different $\Delta\theta$ values (or angular coordinate changes) depending on the initial and final locations within the image field.

For these experiments, Figure 2-3 shows that the angular coordinate changes are small for the uniform displacements present throughout the image. The relative importance of such errors is made even less significant by the fact that the image pairs were chosen to have interframe time intervals that were either two or four times the acquisition time for individual frames. (Interframe intervals

were 24 ms for 4 cm/sec and 48 ms for 2 cm/sec translations, while individual frames were acquired over 12 ms.) The lack of a consistent difference between velocity estimates from translations directed to the left or to the right suggests that the discrepancies seen in two of the test cases were more likely related to experimental variation. However, for faster scatterer velocities or slower frame rate acquisitions, the temporal error due to sequential ultrasound beam scanning may need to be accounted for.

A limitation of these experiments was the use of a phantom that simulated only idealized uniform flow without velocity gradients. The presence of velocity gradients within the sampled interrogation windows may introduce biases into the results. In addition, only velocities up to 4 cm/sec were tested here. For higher speed flows, increased decorrelation of speckle patterns and temporal error from sequential ultrasound beam scanning could have larger effects than for these experiments. We explored each of these issues further in the set of experiments described in the next chapter.

E. Conclusions

In this first set of experiments, we validated the USIV technique using uniform translation of a speckle phantom at known velocities. Overall, USIV performed well and very good agreement was seen for time-averaged velocity measurements compared with reference values. Standard sources of error that affect DPIV with optical images were also confirmed to be relevant with USIV. These included the influence of stationary artifacts as well as compromised performance near interfaces or borders in the images. Additional factors specific to the use of ultrasound-derived images were also identified. For any specific ultrasound imaging arrangement, there is likely an optimal focal depth in terms of achieving the best overall accuracy throughout the image. Theoretically, there will also be an effect related to sequential ultrasound beam scanning, but this may only

be important when scatterer velocities are high relative to beam sweep speeds (or frame rates).

C h a p t e r 3

IN VITRO EXPERIMENTS: STEADY TUBE FLOW WITH NON-AXISYMMETRIC VELOCITY PROFILE

A. Introduction

The second group of experiments was designed to characterize ultrasound speckle image velocimetry (USIV) measurements obtained in a relatively simple fluid flow setting. We created a transparent flow phantom apparatus that allowed both ultrasound and optical imaging to be performed. This enabled a comparison of USIV against a reference standard of digital particle image velocimetry (DPIV) measurements made under identical flow conditions.

For these studies, we focused on steady flow through a cylindrical vessel after a sudden expansion (or confined axisymmetric backward-facing step). We also incorporated 90-degree turns proximal and distal to the expansion in order to create a non-axisymmetric velocity profile. Our motivation was to create simple approximations of two important features that can contribute to flow patterns in large arteries. The sudden expansion was intended to simulate the presence of an atherosclerotic stenosis in the proximal (upstream) portion of the test chamber. The 90-degree turns were intended to simulate the fact that some degree of curvature is present throughout most of the arterial vasculature. Creation of a non-axisymmetric velocity profile also presented the opportunity to examine the ability of USIV to resolve smaller scale flow characteristics.

It should be noted that blood flow in the arteries is clearly more spatially and temporally complex than the experimental setup we used here. Additional details regarding this subject are briefly described in Sections 1.B and 5.B. With this understanding, our primary goal was to create a flow phantom that could be used to directly compare USIV against conventional DPIV analysis while providing a rough approximation of some physiologically relevant flow features.

B. Methods

1. Flow Phantom Apparatus

An experimental setup was constructed allowing both USIV and DPIV measurements to be made on the same imaging plane within an *in vitro* flow phantom (see Figure 3-1 for schematic). The system consisted of a cylindrical test chamber within a transparent silicone tube (1-inch inner diameter) mounted within a water-filled acrylic tank. The test chamber was clamped between two polyvinyl chloride (PVC) pipe elbows with 90-degree clockwise turns. Flow straighteners were placed at the proximal and distal ends of the silicone tube resulting in a unidirectional non-axisymmetric inflow velocity profile. A short acrylic tube (1-inch outer diameter) was inserted into the proximal portion of the test chamber in order to create an axisymmetric backward-facing step. The wall thickness (and step height) of the acrylic tube was 1/4-inch and created a sudden expansion from a 1/2-inch inner diameter to a 1-inch inner diameter. A steady flow pump was used to circulate water seeded with fluorescent polymer spheres (80 μm average diameter, Eastman Kodak Company, Rochester, NY) through the flow loop. The small polymer spheres acted as ultrasound-scattering particles during ultrasound imaging and as fluorescent tracer particles during optical imaging. Flow rates ranged from 0.3 to 1.5 L/min. These flow rates corresponded to Reynolds numbers ranging from 500 to 2500, based on the upstream diameter and bulk velocity for water at 20 degrees Celsius.

2. Ultrasound Imaging

B-mode images were obtained using a General Electric (GE) Vingmed System FiVe ultrasound machine (GE Vingmed Ultrasound, Horten, Norway) and a 2D flat phased array transducer (with beam steering) at up to approximately 242 frames/sec with center frequency at 10 MHz. A water-resistant covering was secured around the transducer and cable junction. The ultrasound transducer was

submerged in the water-filled acrylic tank and fixed in a position that was aligned with the central horizontal plane of the test chamber.

Ultrasound acquisition and experimental parameters were varied in order to test their respective influences on the accuracy of USIV results. These included transducer focal depth and sector width (with associated frame rate changes) as well as volumetric flow rate. Image depth was held constant at 6 cm. The parameter options that were analyzed are summarized in Table 3-1. The specific combinations of imaging and experimental parameters that were used for each test case are listed in Table 3-2.

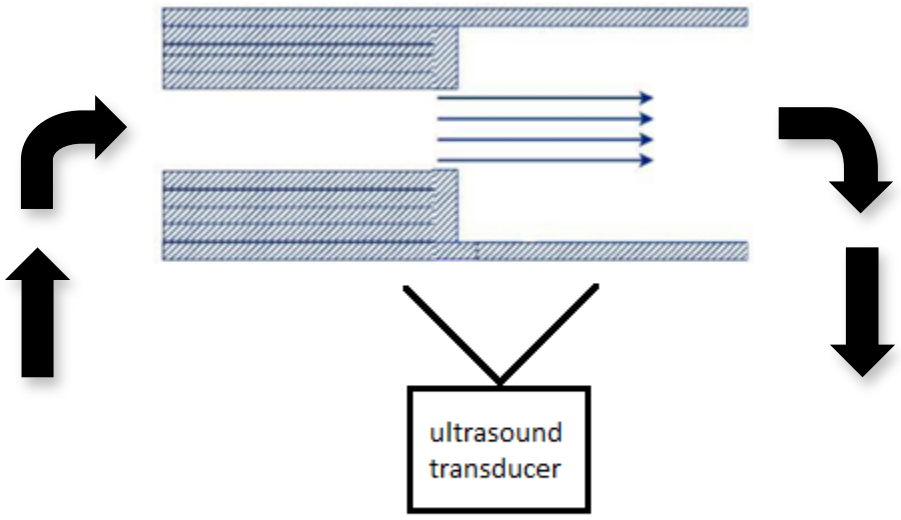

Figure 3-1. Schematic of the flow loop viewed from above and looking down on the horizontal imaging plane through the center of the test chamber (similar for both USIV and DPIV). Flow straighteners were placed at the proximal and distal ends of the test chamber. This arrangement created a unidirectional non-axisymmetric inflow velocity profile encountering a sudden expansion (or backward-facing step) within a cylindrical vessel.

Sector width (frame rate)	Wide (145.1 frames/sec) or narrow (241.8 frames/sec)
Focal depth	Focus at 2, 4, or 6 cm
Volumetric flow rate	0.3, 0.5, 1, or 1.5 L/min

Table 3-1. List of ultrasound acquisition and experimental parameters that were used for steady tube flow experiments.

3. USIV Analysis

B-mode ultrasound cineloop files in Digital Imaging and Communications in Medicine (DICOM) format were converted to sequenced individual bitmap images using EchoMAT software version 2.0 (GE Vingmed Ultrasound, Horten, Norway). This script was used with MATLAB software version 5.3 (The MathWorks, Inc., Natick, MA). Processing included scan conversion of the image scan line data from polar coordinates (as initially acquired by the phased array transducer) to Cartesian coordinates for further analysis.

The scan converted images were imported into a custom in-house DPIV software package for further analysis. Displacement and velocity vectors were calculated using a Fast Fourier Transform (FFT)-based cross-correlation algorithm. Multi-pass interrogation with window shifting was performed using 32 x 32 pixel sampling windows (corresponding to a physical window size of approximately 0.65 x 0.65 cm). The step size was 8 x 8 pixels. The sampling window size was chosen to balance the need to have distinguishable speckle pattern features that were present within the interrogation window for both frames of each image pair while trying to preserve spatial resolution. Correlation peaks were detected using a three-point Gaussian fit and outlier removal with replacement was performed after each pass. Further details regarding these procedures can be found in Willert and Gharib (1991), Westerweel et al. (1997),

and Raffel et al. (2007). Both instantaneous and time-averaged velocities were calculated.

Test Case	Transducer	Image Depth	Sector Width (Frame Rate)	Focal Depth	Volumetric Flow Rate
1	FPA	6 cm	Wide (145.1 fps)	2 cm	0.3 L/min
2	FPA	6 cm	Wide (145.1 fps)	2 cm	0.5 L/min
3	FPA	6 cm	Wide (145.1 fps)	2 cm	1 L/min
4	FPA	6 cm	Wide (145.1 fps)	2 cm	1.5 L/min
5	FPA	6 cm	Wide (145.1 fps)	4 cm	0.3 L/min
6	FPA	6 cm	Wide (145.1 fps)	4 cm	0.5 L/min
7	FPA	6 cm	Wide (145.1 fps)	4 cm	1 L/min
8	FPA	6 cm	Wide (145.1 fps)	4 cm	1.5 L/min
9	FPA	6 cm	Wide (145.1 fps)	6 cm	0.3 L/min
10	FPA	6 cm	Wide (145.1 fps)	6 cm	0.5 L/min
11	FPA	6 cm	Wide (145.1 fps)	6 cm	1 L/min
12	FPA	6 cm	Wide (145.1 fps)	6 cm	1.5 L/min
13	FPA	6 cm	Narrow (241.8 fps)	2 cm	0.3 L/min
14	FPA	6 cm	Narrow (241.8 fps)	2 cm	0.5 L/min
15	FPA	6 cm	Narrow (241.8 fps)	2 cm	1 L/min
16	FPA	6 cm	Narrow (241.8 fps)	2 cm	1.5 L/min
17	FPA	6 cm	Narrow (241.8 fps)	4 cm	0.3 L/min
18	FPA	6 cm	Narrow (241.8 fps)	4 cm	0.5 L/min
19	FPA	6 cm	Narrow (241.8 fps)	4 cm	1 L/min
20	FPA	6 cm	Narrow (241.8 fps)	4 cm	1.5 L/min
21	FPA	6 cm	Narrow (241.8 fps)	6 cm	0.3 L/min
22	FPA	6 cm	Narrow (241.8 fps)	6 cm	0.5 L/min
23	FPA	6 cm	Narrow (241.8 fps)	6 cm	1 L/min
24	FPA	6 cm	Narrow (241.8 fps)	6 cm	1.5 L/min

Table 3-2. Combinations of imaging and experimental parameters used for specific test cases studied for steady tube flow experiments. Abbreviations: FPA (flat phased array), fps (frames per second).

4. Optical Imaging

Optical images were obtained using laser sheet illumination of the central horizontal plane of the test chamber. This was the same target plane that was visualized during ultrasound imaging. A double-pulsed Nd:YAG laser (New Wave Research, Fremont, CA) was used to emit green light at a wavelength of 532 nm that was passed through a cylindrical lens to form the laser sheet. A PULNiX TM-9701 CCD camera (PULNiX Sensors, Sunnyvale, CA) was fixed at a perpendicular angle (looking down from above) in order to image the horizontal plane. An orange lens filter was used to selectively visualize the fluorescent polymer spheres. Image resolution was 768 x 480 pixels and the frame rate was 30 Hz. With the double-pulsed laser technique, the acquisition rate of paired frames was 15 Hz. Volumetric flow rates of 0.3, 0.5, 1 and 1.5 L/min were used. For each flow rate, paired frames at several different pulsing intervals were captured to allow optimization of the interframe displacements relative to the sampling windows.

5. DPIV Analysis

Raw image files captured by the PULNiX CCD camera were imported into the same custom in-house DPIV software package described above. Displacement and velocity vectors were calculated using an FFT-based cross-correlation algorithm. Multi-pass interrogation with window shifting was performed using 32 x 32 pixel sampling windows (corresponding to a physical window size of approximately 0.15 x 0.15 cm). The step size was 16 x 16 pixels. Correlation peaks were detected using a three-point Gaussian fit and outlier removal with replacement was performed after each pass. Further details regarding these procedures can be found in Willert and Gharib (1991), Westerweel et al. (1997), and Raffel et al. (2007). Both instantaneous and time-averaged velocities were calculated.

C. Results

Representative frames from ultrasound and optical imaging are shown in Figure 3-2 and illustrate that there was a significant difference in spatial resolution between these imaging techniques. For the particle concentration used in these experiments, individual particles could be resolved with optical imaging, but not with ultrasound imaging. It should be noted that the ultrasound images and USIV figures in this chapter have a reversed orientation compared to the last chapter with the transducer and near-field region now towards the bottom of the ultrasound images. This was done to facilitate comparisons between the USIV and DPIV results.

Characteristic findings were similar at all flow rates that were tested. Figure 3-3 shows representative examples of time-averaged velocity fields obtained using USIV and DPIV analyses at an identical flow rate. The coarser nature of the speckle pattern features from ultrasound imaging required interrogation windows for USIV that had larger physical dimensions compared to those used for optical imaging and DPIV. The spatial resolution for USIV was, therefore, decreased compared with DPIV. Nevertheless, the overall spatial pattern of velocity vectors was quite similar between techniques.

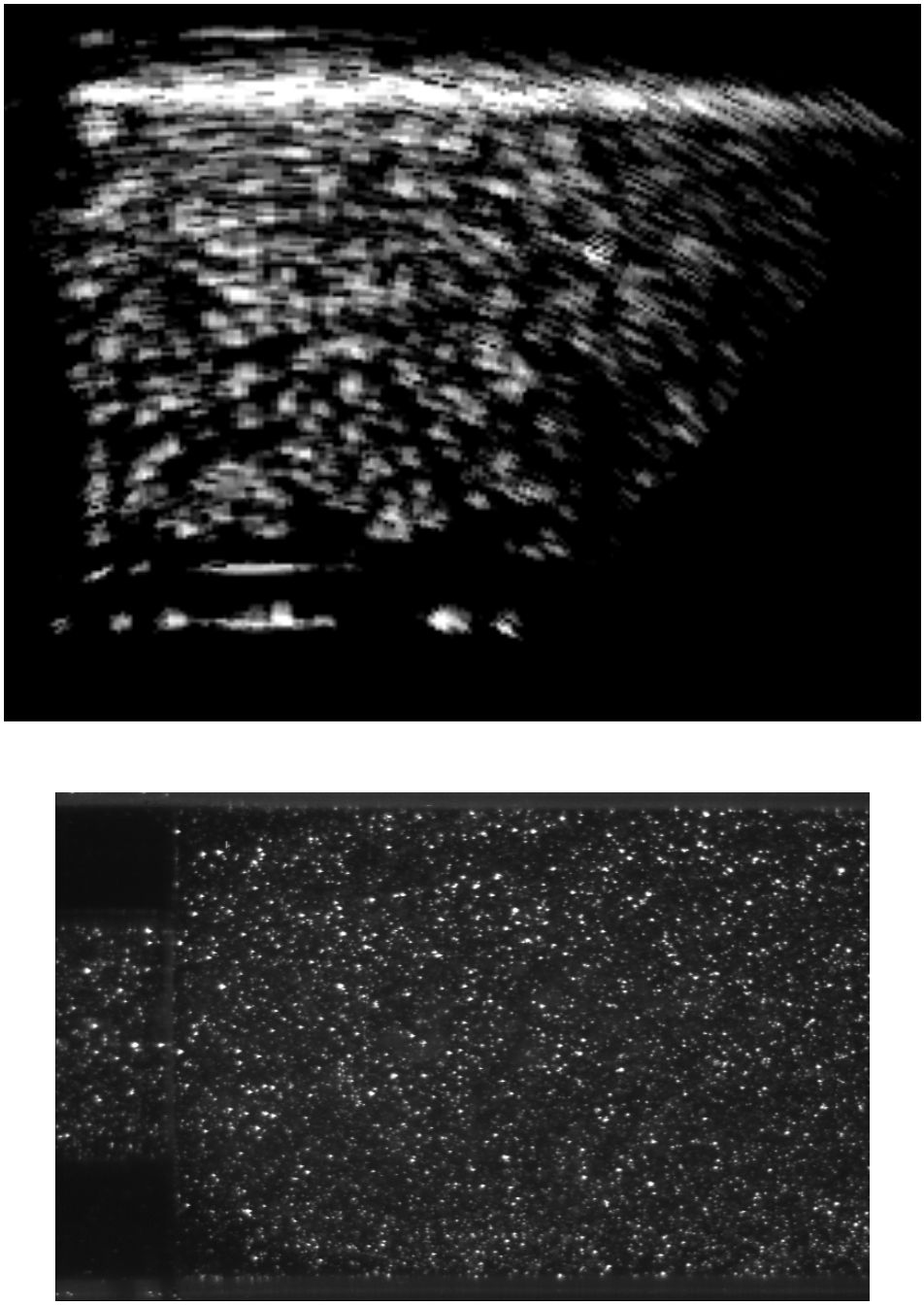

Figure 3-2. Examples of exported frames from ultrasound (top) and optical (bottom) imaging. Both panels have been scaled to show equal physical dimensions of the test chamber. Ultrasound transducer and near-field region are towards the bottom of the top panel.

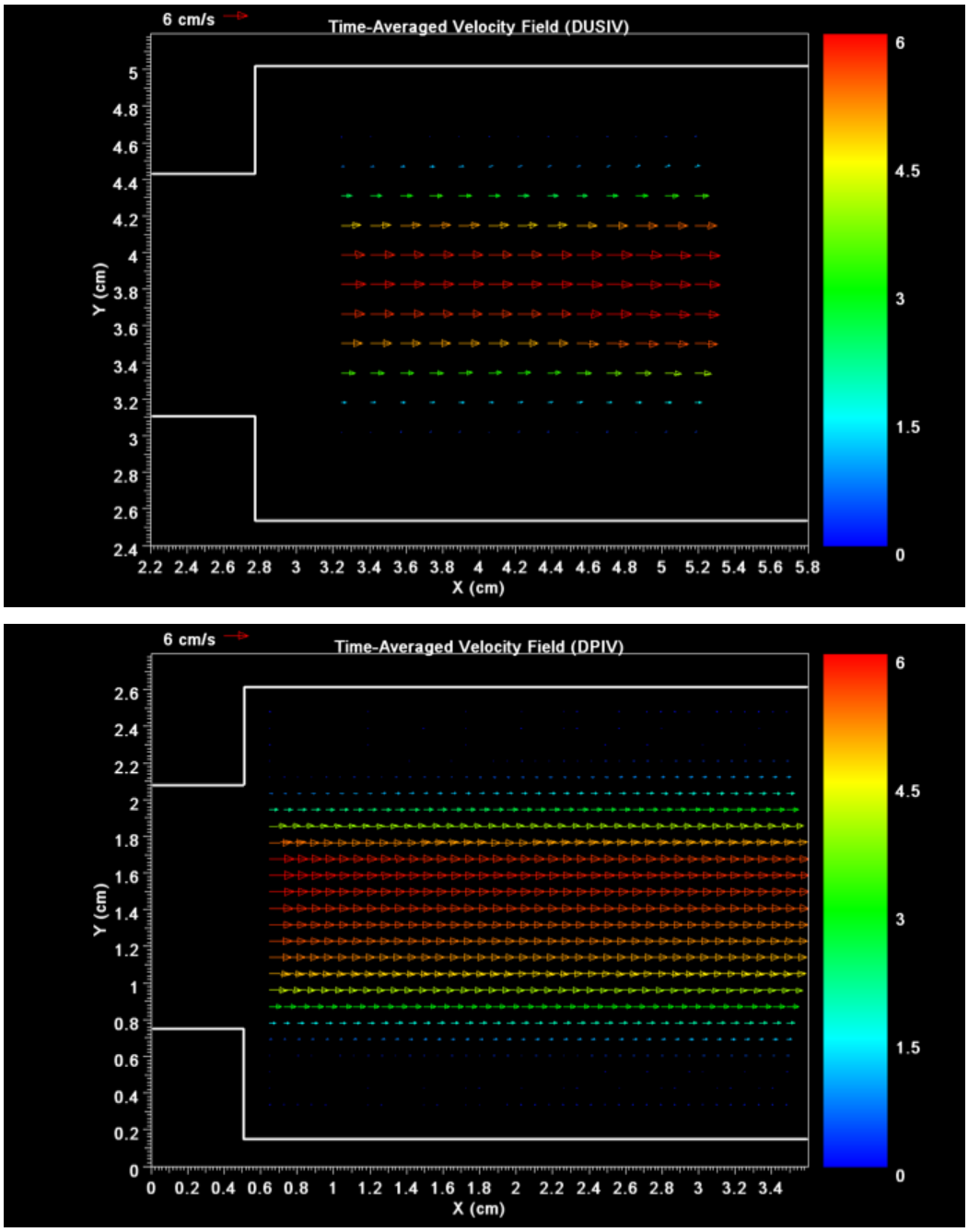

Figure 3-3. Representative examples showing comparison of USIV (top) and DPIV (bottom) time-averaged velocity field measurements. Flow rate was 0.3 L/min, ultrasound image depth was 6 cm, and ultrasound focal depth was 4 cm in this case. Location of the sudden expansion is outlined in each panel.

Representative time-averaged horizontal velocity profiles for USIV and DPIV at an identical flow rate and downstream position from the step are shown in Figure 3-4. The DPIV-derived velocity profile was asymmetric as expected with slightly higher forward velocities seen in the outer half of the cylindrical test vessel (in continuity with the greater curvature of the 90-degree bend). There were also small recirculation regions with low velocity backflow seen at the inner and outer borders of the vessel. The USIV-derived velocity profile showed very good agreement, although the velocity profile asymmetry and the recirculation regions were not detected. The ultrasound images used here were acquired with the focus set near the vessel centerline at a depth of 4 cm from the transducer. The forward flow magnitudes were almost identical in the outer third of the vessel (far-field region of the ultrasound images) and were slightly overestimated near the middle (focal) region. Larger discrepancies with underestimation of velocities were noted in the inner third of the vessel (near-field region of the ultrasound images).

Figure 3-5 shows representative examples using the data from above (including ultrasound images with focal depth at 4 cm) along with additional USIV time-averaged velocity profiles obtained from images with different ultrasound beam focal depths (at 2 and 6 cm from the transducer).

With focal depth near the transducer at 2 cm, the ultrasound beam was narrowest before encountering the vessel. The velocity profile changed very little compared with the profile obtained with focal depth at 4 cm. When compared with DPIV results, both of these profiles showed excellent agreement in the outer third of the vessel, slight overestimation near the vessel centerline, and increased discrepancies with velocity underestimation in the inner third of the vessel.

With focal depth far from the transducer at 6 cm, the ultrasound beam was narrowest after it had already passed through the vessel. The velocity profile showed decreases in the velocities at almost every position compared to the profile obtained with focal depth at 4 cm. Agreement with the DPIV-derived

velocity profile remained good in the outer third of the vessel. There was overall improvement near the vessel centerline, but some underestimation was then seen at the position with the peak velocity found by DPIV. In addition, the underestimation of velocities in the inner third of the vessel became more pronounced.

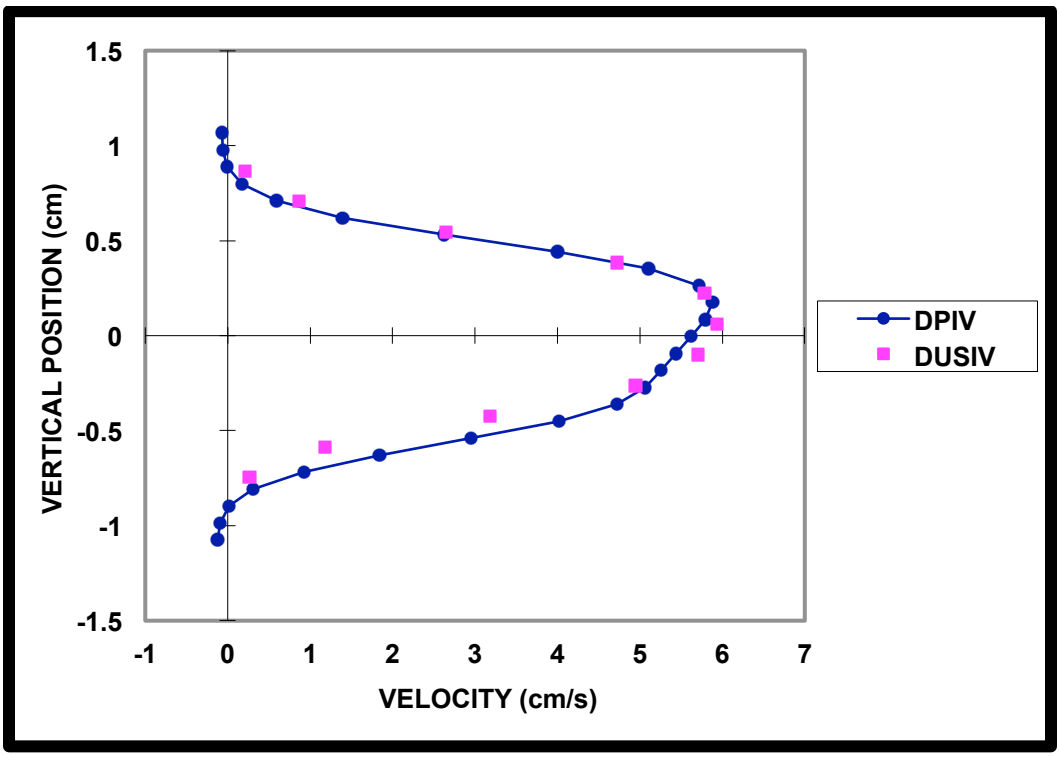

Figure 3-4. Representative example showing comparison of time-averaged horizontal velocity profiles for USIV (magenta squares) and DPIV (blue circles with line) at a position 1.5 cm downstream of sudden expansion. Vessel centerline was designated as the vertical axis origin and the outer half of the test chamber (with far-field region of ultrasound images) was defined as having positive vertical position. Flow rate was 0.3 L/min and ultrasound focal depth was placed near vessel centerline in this case (approximately 0.2 cm on positive vertical axis shown here).

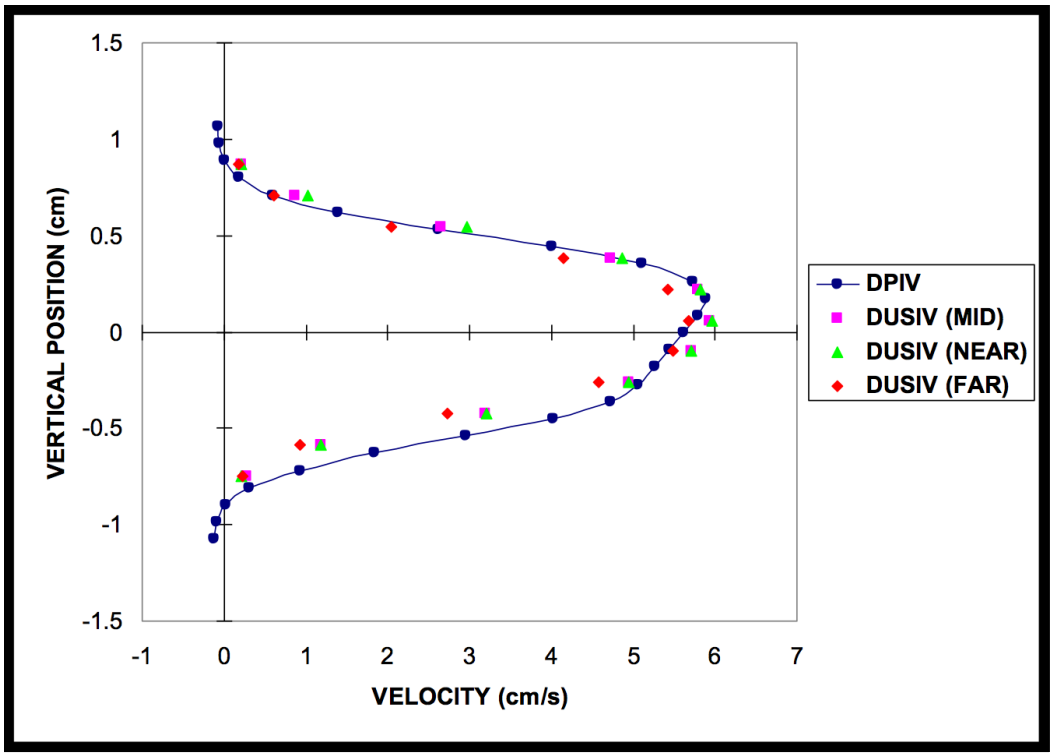

Figure 3-5. Representative example showing comparison of time-averaged horizontal velocity profiles for USIV with varied focal depths as well as DPIV at a position 1.5 cm downstream of sudden expansion. Vessel centerline was designated as the vertical axis origin and the outer half of the test chamber was defined as having positive vertical position. Flow rate was 0.3 L/min. Ultrasound focal depth was placed either near the vessel centerline (labeled as MID) at 0.2 cm on the vertical axis, near the transducer (labeled as NEAR) and before the vessel at -1.8 cm on the vertical axis, or far from the transducer (labeled as FAR) and after the vessel at 2.2 cm on the vertical axis.

D. Discussion

The representative frames shown in Figure 3-2 demonstrate the difference in spatial resolution between ultrasound and optical images. As discussed in Section 1.D.4, this illustrates the general situation where the “speckles” that are visualized do not represent individual particles and are the result of constructive

and destructive interference of the backscattered signals from many subresolution particles.

The representative velocity fields shown in Figures 3-3 and 3-4 demonstrate good overall agreement between USIV and DPIV velocity profiles. The different source image characteristics, though, resulted in a five-fold difference in spatial resolution of the respective velocity fields. The physical dimensions of the interrogation windows used were 0.65 x 0.65 cm for USIV compared with 0.15 x 0.15 cm for DPIV. Accordingly, some details present in the DPIV velocity profile were slightly different for USIV. The precise vertical position of the peak horizontal velocity and asymmetric shape of the velocity profile were not exactly captured by USIV. The USIV velocity profile was more symmetric in shape and slightly narrower in width. In addition, low velocity backflow in the small recirculation zones after the sudden expansion was not detected by USIV.

The narrower width of the USIV velocity profile was associated with velocity underestimation in the inner third of the vessel that was closest to the transducer. This finding is interesting and not necessarily intuitive. The near-field region might be expected to show better performance than the far-field region since lateral resolution worsens with beam divergence after the focal depth. However, Touil et al. (2008) performed simulations for ultrasound imaging of axial translation with both linear and beam-steered phased array transducers. They used spatially variant point spread functions that modelled depth-dependent transducer properties. As expected, larger displacements led to more decorrelation between speckle patterns generated before and after translation. Interestingly, though, decorrelation was significantly increased in the near-field compared with the focal region. This was attributed to the relatively rapid changes that occur for the point spread function in the near-field region close to the transducer. They found that the effect was even more pronounced with a beam-steered phased array transducer (using a polar imaging geometry) if the translation was oblique and,

therefore, included a component in the lateral direction. The presence of increased decorrelation likely caused the bias towards lower velocities in the near-field region seen in our results (as shown in Figure 3-4).

For our experiments, only small changes in velocity estimates were noted when the focal depth was moved closer to the transducer (from 4 to 2 cm). However, more significant changes were seen when the focal depth was moved away from the transducer (from 4 to 6 cm). In the latter situation, the focal depth was located outside of the cylindrical test vessel.

A possible explanation for these findings is suggested by considering the equation for the ultrasound beam width at its focal depth that was previously given in Section 1.C as

$$FWHM = 1.4\lambda \frac{F}{D} \approx 1.4\lambda \frac{R}{D} , \tag{3.1}$$

where $FWHM$ is the full width at half maximum amplitude, λ is the wavelength of the ultrasound center frequency, F is the focal length, D is the aperture diameter, and R is the radius of curvature. It should be noted that if the focal length is increased, then the beam width (which is narrowest at that position) also increases. Figure 3-6 illustrates this concept and shows that moving the focal depth past the second wall of the test vessel ("weak focusing" example) results in increased beam width and worsened lateral spatial resolution over the entire interrogation region within the vessel. It is plausible that uniformly worsened spatial resolution could be responsible for the decreased accuracy seen throughout the velocity profile when the focal depth was increased and moved outside of the test vessel.

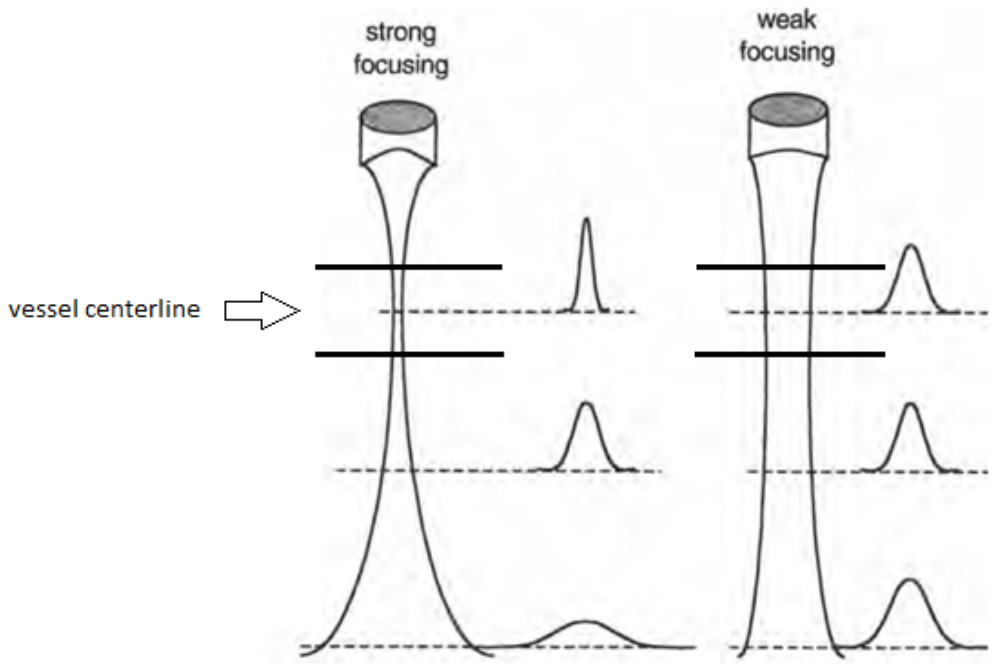

Figure 3-6. Schematic showing changes in lateral spatial resolution with changes in ultrasound transducer focusing strength. For the "strong focusing" example, the focal depth is at the centerline of the cylindrical test vessel. For the "weak focusing" example, the focal depth is outside of the vessel and there is worsened lateral resolution throughout the vessel profile (although there is shallower beam divergence far from the transducer). Adapted with permission from Webb (2003).

These results suggest that an optimal focal depth exists with regard to USIV performance for a given imaging and analysis configuration. This concept was previously discussed in Section 2.D based on the experimental results described there. The results from both the prior and current chapter imply that, for the regions of interest tested, the optimal focal depth was near the middle of the image field with respect to overall USIV performance. In Chapter 2, accuracy was best when the focal depth was set at 5 cm (with an image depth of 10 cm). For the experiments described in this chapter, accuracy was best when the focal depth was set at 4 cm (with an image depth of 6 cm).

This is not the same approach that is typically taught with regards to optimizing images during clinical acquisitions (where the focus is placed at the level of the deepest structure of interest). For example, when imaging a patient's left ventricle from an apical transthoracic approach, the focus would be placed at the level of the mitral valve annulus. This is intended to prevent significant beam divergence (and the associated degradation of lateral spatial resolution) for any part of the visualized left ventricle. Interestingly, optimizing images for USIV accuracy may, therefore, require a slightly different approach than is used when optimizing for visual interpretation in clinical settings.

Prior work in the literature has shown that the factors dictating the accuracy of speckle tracking approaches similar to USIV can be complicated and dependent upon implementation specifics. For instance, the amount of interframe speckle pattern decorrelation is influenced by the direction of scatterer movement (axial or lateral) relative to the transducer. Bohs et al. (1995) and Friemel et al. (1998) found increased speckle decorrelation for laminar flow in a cylinder if there was an axial velocity component (compared with flow only in the lateral direction). This was attributed to increased sensitivity of the speckle patterns to unequal scatterer displacements in the axial direction due to velocity gradients. For purely lateral flow, there was no significant relative axial motion of scatterers. Kim, Hertzberg, et al. (2004) showed results supporting this concept, with slightly decreased accuracy when flow deviated from being only in the lateral direction. In contrast to those studies, however, Ramamurthy and Trahey (1991) and Touil et al. (2008) found that speckle decorrelation was decreased when motion was purely in the axial direction. The latter studies, though, were performed in the setting of uniform scatterer translations without any velocity gradients present.

Of the five studies just described, almost all performed speckle tracking on scan line data from flat phased array transducers with beam steering that were displayed in polar coordinates (rather than scan converted to Cartesian coordinates). Ramamurthy and Trahey (1991), though, used a linear phased array

transducer instead that directly acquired data in Cartesian coordinates, while Touil et al. (2008) studied both linear and beam-steered phased array transducers (without scan conversion).

Kim, Hertzberg, and Shandas (2004) described in another study that there appeared to be more outliers when speckle tracking was performed on scan converted data compared with polar data, but a systematic accuracy comparison was not performed and their study utilized harmonic (rather than fundamental) imaging.

More information is available regarding the comparison of speckle tracking accuracy when performed on radiofrequency (RF) versus envelope-detected data. Initial observations by Ramamurthy and Trahey (1991) suggested that using RF data provided better results. Subsequent work by Bohs et al. (1995), however, showed better performance using envelope-detected data. Methodology differences between these two studies led Bohs et al. (2000) to suggest that the increased frequency content of RF data can potentially be leveraged to improve accuracy, but only when axial sampling rates are sufficiently high relative to the transmit frequency.

The implementation most similar to USIV has been referred to as echo PIV in a series of papers including those by Kim, Hertzberg, and Shandas (2004) and Liu et al. (2008). Methodological differences from USIV include ultrasound acquisition using harmonic imaging as well as the performance of analyses on polar, rather than Cartesian, data. Kim, Hertzberg, and Shandas (2004) showed fairly good agreement under certain conditions for echo PIV compared with the analytical solution for laminar pipe flow. Though not explicitly described, detailed inspection of the velocity vector field that was shown reveals that there was actually an asymmetry of velocities relative to radial position for their experiments also. Peak velocities were skewed towards the far-field region of the pipe and near-field velocities appear to have been biased towards lower values. The averaged velocity profile that is shown does not seem entirely consistent with

the velocity vector field shown, but the velocity profile is missing data for the outer fifth of the pipe. It is also not clear how the averaging was performed and how the spatial variation of vector positions along different beam lines was accounted for. Overall, it appears that their data are consistent with the trends that we observed regarding near-field and far-field performance.

Liu et al. (2008) suggested that, for the best accuracy with echo PIV, the focal depth should be set either in the center of or just beyond the region of interest. This was based upon the number of outliers seen with different settings and the concept of avoiding beam divergence after the focal depth. As described above, though, our quantitative evaluations in both the preceding chapter and this one suggest that the optimal focal depth is near the middle of the region of interest.

A limitation of the experiments described in this chapter was the testing of peak velocities only up to 6 cm/sec. In addition, we did not perform specific evaluations of whether USIV accuracy would change if axial (rather than lateral) flow was measured, if polar (rather than Cartesian) ultrasound data was used, if RF (rather than envelope-detected) ultrasound data was used, or if an echocardiographic contrast agent with harmonic (rather than fundamental) imaging was used. These topics would certainly be of interest for future work towards better understanding of the technique.

E. Conclusions

Overall, the USIV technique produced velocity estimates that were fairly similar to those obtained using the reference standard of DPIV. This was confirmed using an *in vitro* experimental setup with simple, but physiologically interesting, features that simulated arterial curvature and stenosis. The setup also allowed testing with a non-axisymmetric velocity profile that led to the presence of velocity gradients within the USIV interrogation windows. We found that USIV accuracy was slightly decreased in the near-field region and that the

optimal focal depth appeared to be near the center of the overall region of interest. This knowledge can aid in the rational design and interpretation of future experiments utilizing USIV measurements.

Chapter 4

IN VIVO EXPERIMENTS: FLOW IN THE LEFT VENTRICLE

A. Introduction

We performed a set of *in vivo* experiments in order to test the feasibility of the USIV technique for evaluating physiologic flow in the left ventricle. We used a porcine open-chest model with epicardial imaging in order to maximize image quality. An intravenous microbubble contrast agent was injected to improve intracavitary flow visualization. Our goal was to assess whether USIV analysis could be used to obtain additional flow details beyond conventional ultrasound imaging techniques and, therefore, allow improved understanding of left ventricular fluid dynamics.

B. Background Related to Left Ventricular Flow

Heart failure is a leading cause of morbidity and mortality throughout the world (Libby and Braunwald, 2008). This clinical syndrome can be caused by a variety of etiologies that include myocardial ischemia and infarction, valvular disease, arrhythmias, hypertension, genetic disorders, infections, inflammation, myocardial infiltration, pericardial disease, endocrine disorders and toxins. Symptoms may be related to acute or chronic decompensation and occur in the setting of either preserved or reduced systolic function. When global systolic function remains preserved, the inadequate cardiac performance is primarily attributed to diastolic dysfunction.

Ultimately, there are pathophysiologic changes in cardiac function that may lead to a vicious cycle of decreased cardiac output followed by ventricular remodeling that eventually leads to worsened ventricular dysfunction and further deleterious changes. Studying left ventricular mechanics in both healthy and disease states is clearly important for understanding the initially compensatory,

but eventually pathologic, responses to myocardial stress and injury. This type of knowledge can contribute towards the development of improved treatment strategies.

While much attention has been directed towards understanding myocardial tissue mechanics, it has long been recognized that cardiac fluid mechanics plays a crucial role as well (Fung, 1997; Thiriet, 2008a, 2008b). A number of interesting studies have been published that highlight many important concepts relevant to ventricular fluid dynamics. These factors influence the heart's ability to effectively drive blood (and oxygen) transport throughout the body.

One common clinical method used to evaluate left ventricular filling is echocardiographic pulsed-wave measurement of mitral inflow velocities. Peak velocities are measured during left ventricular suction (E-wave) and atrial contraction (A-wave). The ratio of peak E- and A-wave velocities, or E/A ratio, is used to help determine whether or not there is diastolic dysfunction and, if so, how severe it is (Nagueh et al., 2009). The E/A ratio is not used in isolation because it can become “pseudonormal” in the setting of moderate diastolic dysfunction. Other echocardiographic parameters are also considered such as left atrial size, mitral annular tissue velocities, and mitral inflow deceleration time. All of these measurements have limitations and can sometimes provide discordant categorizations of diastolic function. In addition, despite providing valuable hemodynamic information, these parameters provide little insight regarding spatial flow characteristics.

There has been interest in using flow visualization (either through noninvasive imaging or computational modeling) to better understand normal and abnormal intracavitary left ventricular flow. Using two-dimensional velocity-encoded phase-contrast magnetic resonance (MR) imaging, Mohiaddin (1995) found spatially abnormal inflow patterns in dilated ischemic left ventricles compared to controls. Kilner et al. (2000) used phase-contrast MR imaging to map intracavitary flow patterns in the right atrium, left atrium, and left ventricle

in healthy volunteers. They proposed that the spatial looping and asymmetries of adult human heart chambers allow for increased efficiency of blood flow redirection during the cardiac cycle. Figure 4-1 shows the typical flow pattern across the mitral valve during left ventricular filling. When viewed in an oblique long-axis plane, the early diastolic flow pattern includes two vortical structures with a larger one located anteriorly and a smaller one located posteriorly.

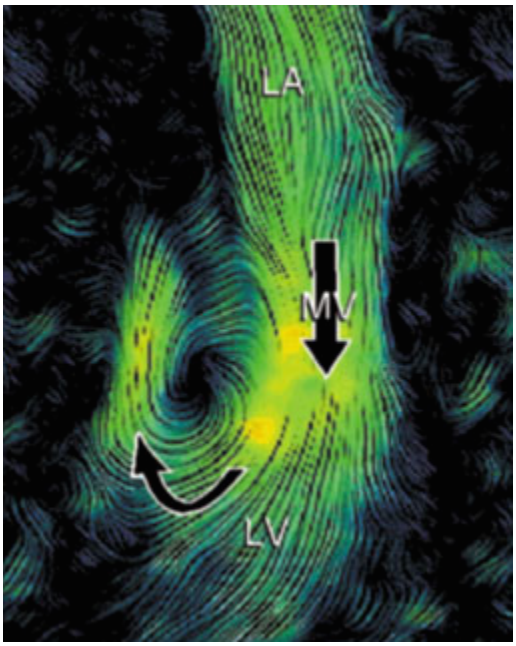

Figure 4-1. Streamlines during early diastolic left ventricular filling obtained by two-dimensional velocity-encoded phase-contrast magnetic resonance imaging. LA, left atrium; MV, mitral valve; LV, left ventricle. Reprinted with permission from Kilner et al. (2000).

These findings are consistent with those from a computational model of early and mid-diastolic filling by Domenichini et al. (2005). Physiologic parameters were chosen to model the ranges seen for normal hearts. Their results showed that the primary flow feature is development of a single asymmetric ring-shaped vortical structure that is larger anteriorly and smaller posteriorly.

The flow patterns described above are relevant to prior fundamental work by Gharib et al. (1998) detailing the physical principles governing vortex ring formation and suggesting that some biological systems benefit from optimization of this process. Their study was performed using a piston-cylinder apparatus to eject starting jets into quiescent fluid and create axisymmetric vortex rings (see Figure 4-2). The dimensionless vortex formation time VFT is equivalent to the stroke ratio of the ejected fluid column. This refers to the ratio of the piston stroke length L to the cylinder diameter D. This definition can be written as

$$\begin{aligned} VFT &= \frac{\overline{U}_p t}{D} \\ &= \frac{L}{D}, \end{aligned} \tag{4.1}$$

where $\overline{U}_p$ is the mean piston velocity and t is the ejection time period.

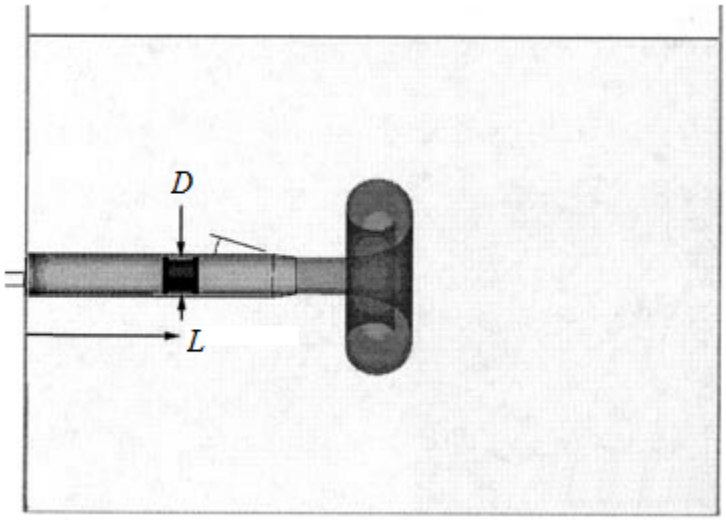

Figure 4-2. Piston-cylinder apparatus used to study vortex ring formation with cylinder diameter D and piston stroke length L. Adapted with permission from Gharib et al. (1998).

They observed that, under all conditions tested, there was a maximum circulation that the leading vortex ring could attain. This always occurred at a vortex formation time that was approximately equal to 4 (ranging from 3.6-4.5.) This specific value for the dimensionless vortex formation time was referred to as the "formation number." It corresponded to the time when the leading vortex ring could no longer increase in size and any additional ejected fluid would form a trailing jet. This phenomenon is illustrated in Figure 4-3. In the top panel, all of the fluid that was ejected (with $VFT = 2$) rolled up into a single vortex ring. Contrastingly, the bottom panel shows that for a large vortex formation time (with $VFT = 8$ at the time of the image) there was a leading vortex ring that was followed by a trailing jet. The middle panel shows a vortex ring formed from a piston-cylinder pulse that was stopped when the formation number ($VFT = 3.8$) was reached. Notably, this vortex ring was the same size as the leading vortex ring that had a trailing jet.

From the standpoint of biological transport phenomena such as left ventricular filling or pulsatile propulsion by squid and jellyfish, these findings suggest that there are energetic benefits to operating in the optimal range for vortex ring formation. It has been shown that mass and momentum transport for starting jets are most efficient when vortex rings with maximum circulation are ejected without the presence of trailing jets (Krueger et al., 2003; Dabiri and Gharib, 2004). This concept has motivated studies looking at clinical measurements of the left ventricular filling process that will be described in the following paragraphs.

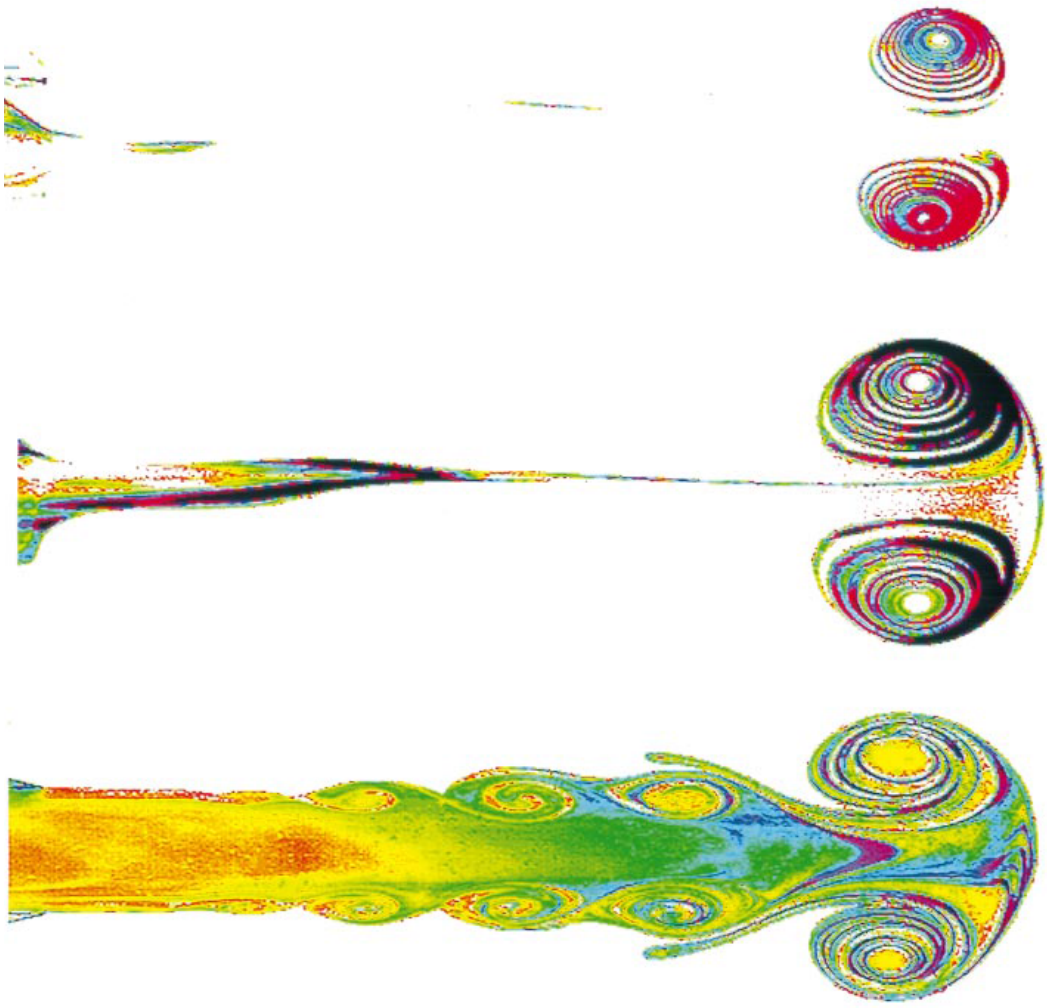

Figure 4-3. Flow visualization showing that maximum leading vortex ring size is achieved for vortex formation time VFT approximately equal to 4. VFT was 2 for top panel and 3.8 for middle panel. Bottom panel was obtained when VFT was equal to 8. Reprinted with permission from Gharib et al. (1998).

Gharib et al. (2006) used standard echocardiographic measurements to estimate vortex formation times during early diastolic filling in volunteers and patients with dilated cardiomyopathy. Figure 4-4 shows that for volunteers (ranging from approximately 20 to 90 years old) the estimated vortex formation times were clustered around values from 4 to 5. Contrastingly, patients with

known dilated cardiomyopathy had vortex formation times that were well below the range for volunteers without diagnosed heart disease. These findings are consistent with the hypothesis that vortex ring formation is optimized in normal cardiac function and becomes deranged in, at least some, disease states.

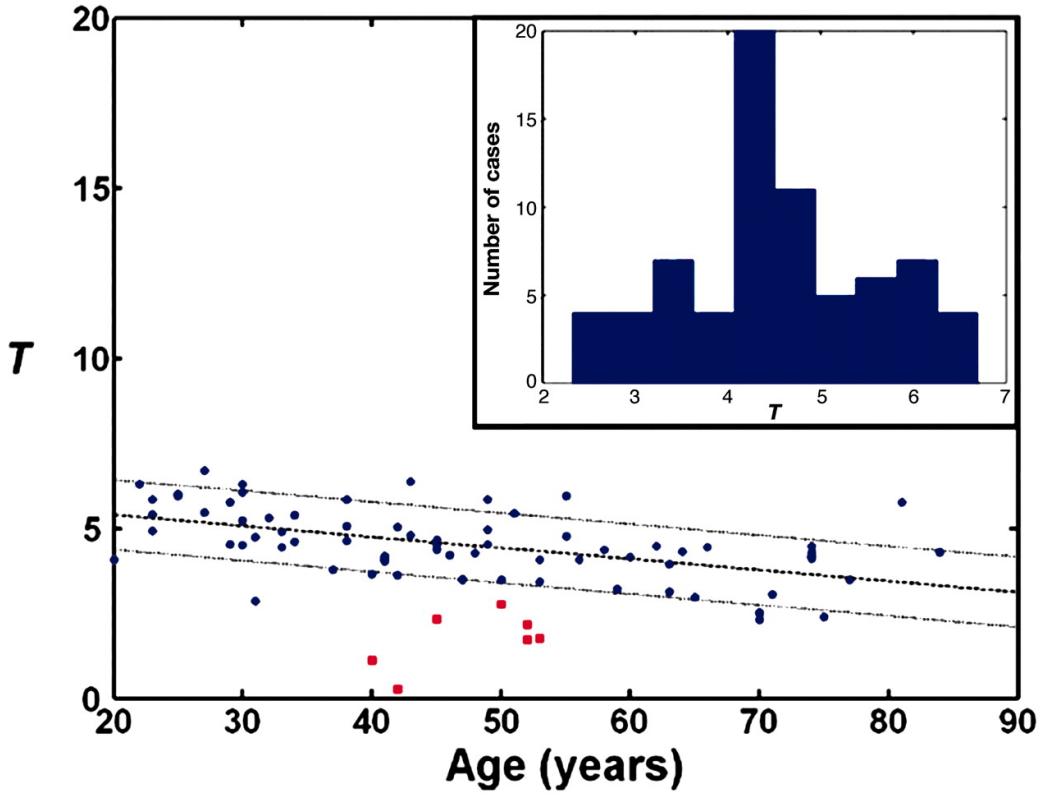

Figure 4-4. Estimates of vortex formation times from clinical echocardiographic measurements. Blue dots represent volunteers and red dots represent patients with dilated cardiomyopathy. Reprinted with permission from Gharib et al. (2006).

The clinical data above were obtained using B-mode echocardiography for anatomical measurements and Doppler echocardiography for velocity measurements. These methods did not involve flow visualization. When considering left ventricular vortex formation, however, direct measurements of vorticity and other parameters would be quite valuable. This requires a technique

that can give multicomponent velocity fields within the left ventricular cavity and, therefore, allow for quantitative flow visualization. As discussed in prior sections, there have been many studies using velocity-encoded phase-contrast magnetic resonance imaging to look at left ventricular velocity vector fields. That approach, however, suffers from the limited temporal resolution of magnetic resonance imaging.

While ultrasound imaging provides much improved temporal resolution, there have only been a few studies attempting to use standard ultrasound transducers to obtain *in vivo* multicomponent left ventricular velocity fields. These studies have generally used similar approaches to USIV, although there have been differences in the specific implementation details.

Sengupta et al. (2007) used an open-chest porcine model with intravenous microbubble contrast infusion in order to visualize intracavitary left ventricular flow. They referred to their approach as ultrasonic DPIV and observed the presence of large vortical structures during isovolumic contraction and relaxation. They also noted that these flow patterns were disrupted when the hearts were subjected to epicardial pacing and an altered sequence of myocardial activation.

Hong et al. (2008) performed echocardiography with intravenous microbubble contrast injections in patients with left ventricular dysfunction and in controls. Using a technique referred to as vector PIV, they measured velocity vectors and vorticity throughout the cardiac cycle and observed differences in vortical flow dynamics between the test groups.

Both of these studies described velocimetry techniques that were generally similar to USIV. Neither, however, made comments about potential differences in measurement accuracy that might occur when translating this type of approach from the *in vitro* setting to the *in vivo* setting. Our goal was to conduct a set of pilot experiments on animals with normal cardiovascular function in order to better understand the applicability of USIV for evaluating *in vivo* left ventricular intracavitary flow patterns.

C. Methods

1. Animal Preparation

The open-chest porcine model used in these experiments was similar to that described in Liakopoulos et al. (2006). Two Yorkshire-Duroc pigs (34-40 kg) were premedicated with ketamine (15 mg/kg) and diazepam (0.5 mg/kg) intramuscularly and anesthetized with 1.5% inhaled isoflurane throughout the procedure. Tracheotomy and endotracheal intubation were performed, followed by mechanical ventilation (Siemens Ventilator Servo 900 C, Siemens-Elema, Solna, Sweden). FiO2 and tidal volumes were adjusted to maintain a PaO2 above 100 mm Hg and PaCO2 in the range between 30-40 mm Hg. Invasive arterial pressure measurements were obtained after femoral artery cannulation. Pulmonary artery catheterization was performed through the right external jugular vein to allow measurements of pulmonary artery pressure, pulmonary capillary wedge pressure and cardiac output by thermodilution. Median sternotomy and then pericardiotomy were performed to allow direct epicardial access. A solid-state pressure transducer catheter (Model MPC-500, Millar Instruments, Houston, TX) was introduced into the left ventricle through a transapical approach.

The experimental protocol was approved by the Institutional Animal Care and Use Committee at the University of California at Los Angeles. All animals received humane care in compliance with the Guide for the Care and Use of Laboratory Animals (1996).

2. Ultrasound Imaging

Open-chest epicardial echocardiography was performed from an apical four-chamber view. B-mode and color flow images were obtained using a GE Vingmed System FiVe ultrasound machine (GE Vingmed Ultrasound, Horten, Norway) and a 2D flat phased array transducer (with beam steering) at up to 372 frames/sec with center frequency at 10 MHz.

To allow intracavitary left ventricular flow visualization, intravenous microbubble contrast consisting of perflutren (octafluoropropane) gas in an albumin shell (Optison, Amersham Health, Princeton, NJ) was injected in doses ranging from 0.01 to 0.03 mL/kg. As described in Porter et al. (2001), animals were prophylactically given ketorolac 60 mg IV and methylprednisolone 40 mg IV to prevent pulmonary hypertension.

3. USIV Analysis

B-mode ultrasound cineloop files in Digital Imaging and Communications in Medicine (DICOM) format were converted to sequenced individual bitmap images using EchoMAT software version 2.0 (GE Vingmed Ultrasound, Horten, Norway). This script was used with MATLAB software version 5.3 (The MathWorks, Inc., Natick, MA). Processing included scan conversion of the image scan line data from polar coordinates (as initially acquired by the phased array transducer) to Cartesian coordinates for further analysis.

The scan converted images were imported into a custom in-house DPIV software package for further analysis. Displacement and velocity vectors were calculated using a Fast Fourier Transform (FFT)-based cross-correlation algorithm. Multi-pass interrogation with window shifting was performed using 32 x 32 pixel sampling windows (corresponding to a physical window size of approximately 0.74 x 0.74 cm). The step size was 8 x 8 pixels. The sampling window size was chosen to balance the need to have distinguishable speckle pattern features that were present within the interrogation window for both frames of each image pair while trying to preserve spatial resolution. Correlation peaks were detected using a three-point Gaussian fit and outlier removal with replacement was performed after each pass. Further details regarding these procedures can be found in Willert and Gharib (1991), Westerweel et al. (1997), and Raffel et al. (2007). Instantaneous velocities within the left ventricle were

calculated throughout the cardiac cycle. Vorticity was derived from the two-dimensional velocity fields.

D. Results

Contrast echocardiography allowed both qualitative and quantitative flow visualization within the left ventricle. Figure 4-5 shows representative images from several phases of the cardiac cycle.

At the beginning of ventricular diastole, both mitral valve leaflets opened quickly and simultaneously. This was followed by entry of the early diastolic filling jet (E-wave) into the left ventricle. During that process, the appearance of two vortical structures was noted. The larger one was located anteriorly and adjacent to the anterior mitral valve leaflet, while the smaller one was located posteriorly and adjacent to the posterior mitral valve leaflet. During diastasis, the mitral valve leaflets became almost, but not completely, closed again and the two vortical structures continued to be the dominant features of the flow field. Upon atrial contraction, the late diastolic filling jet (A-wave) was ejected into the left ventricle with subsequent formation of new anterior and posterior vortical structures that were present briefly prior to the start of ventricular systole.

Figure 4-6 shows a representative velocity field during early diastolic filling. High magnitude velocity vectors comprising the inflow jet were seen crossing the mitral valve annular plane into the left ventricle. Small vortical flow structures were seen at the anterior and posterior borders of the jet that were consistent with roll-up of the shear layers adjacent to the anterior and posterior mitral valve leaflet tips. Figure 4-7 shows a corresponding vorticity plot showing the vorticity generated along the leaflet surfaces bounding the inflow jet at the entrance into the left ventricle.

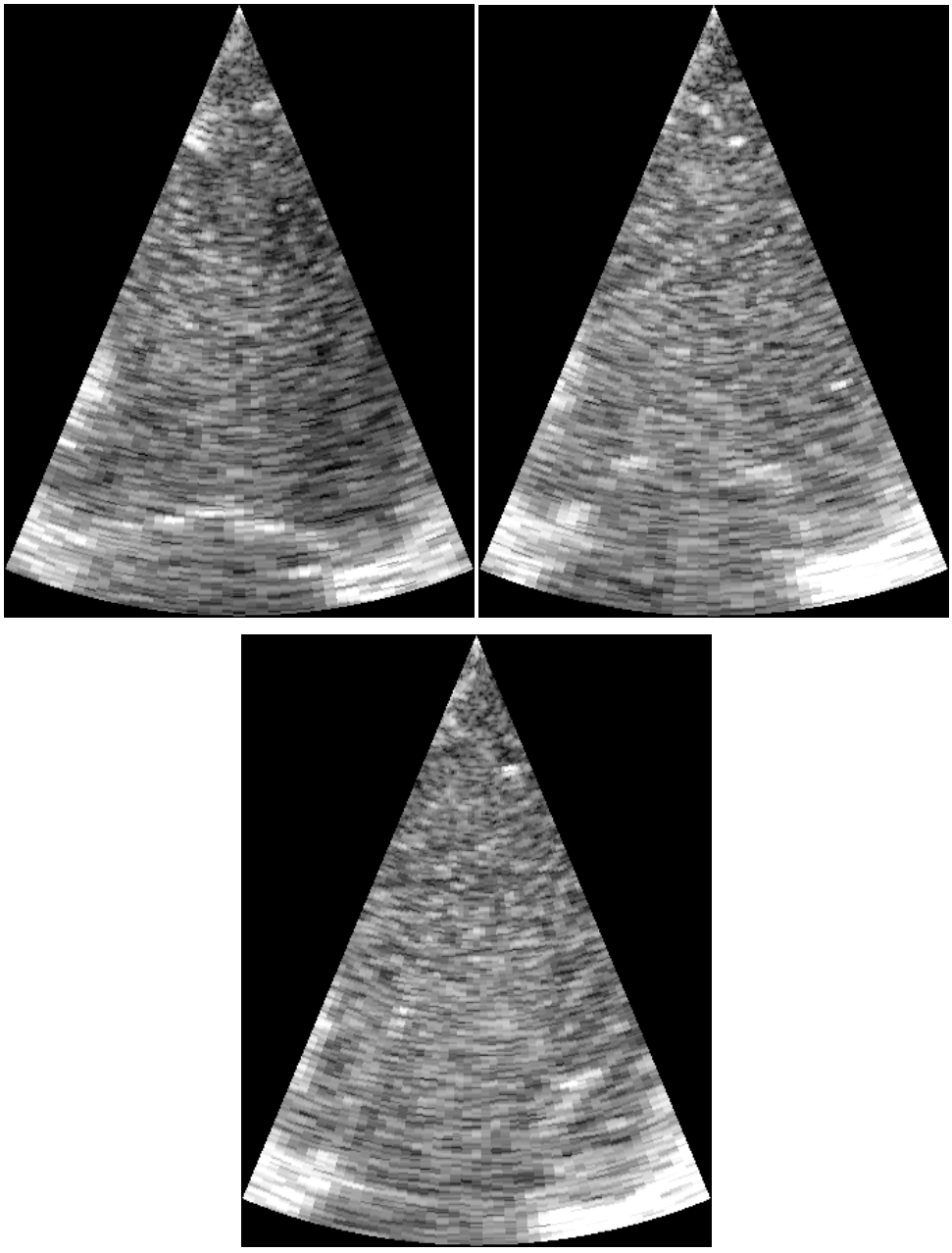

Figure 4-5. Contrast echocardiography images exported with EchoMAT showing end-systole (top left), early diastole during mitral valve opening (top right) and early diastole with mitral valve fully open (bottom).

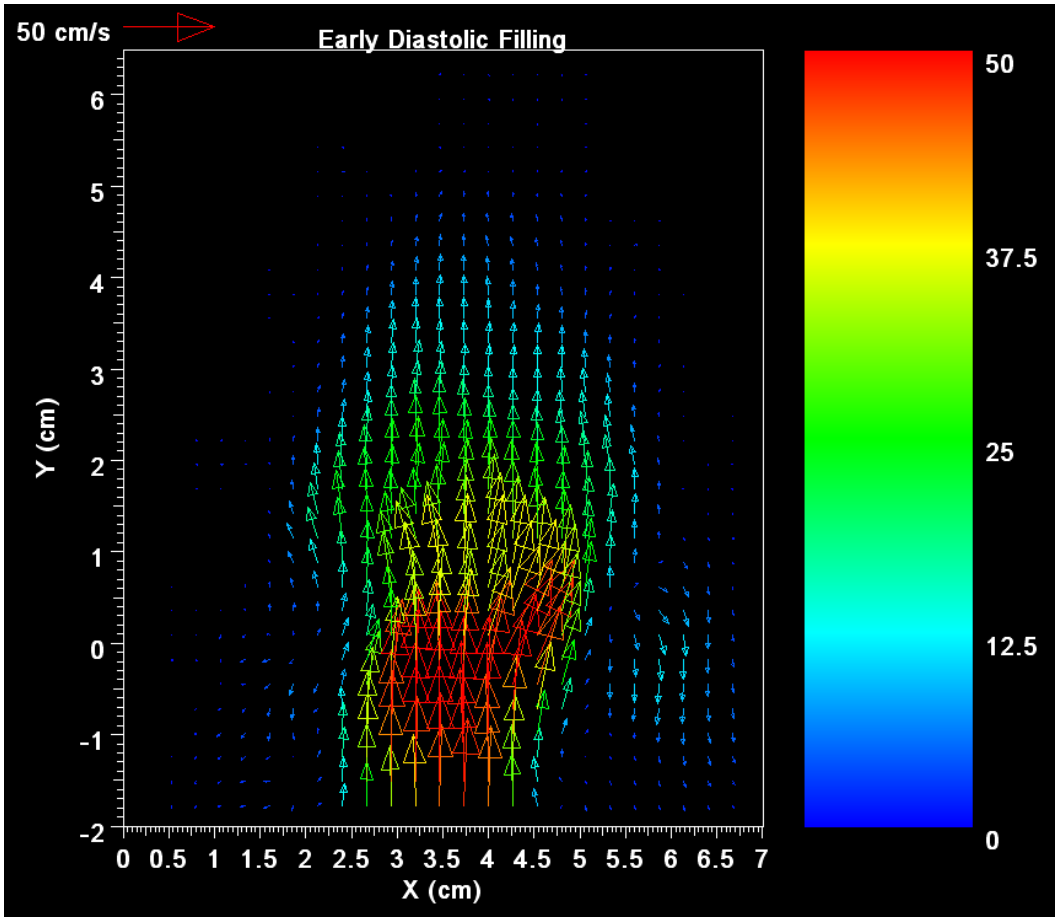

Figure 4-6.Instantaneous velocity field during early diastolic filling of the left ventricle.

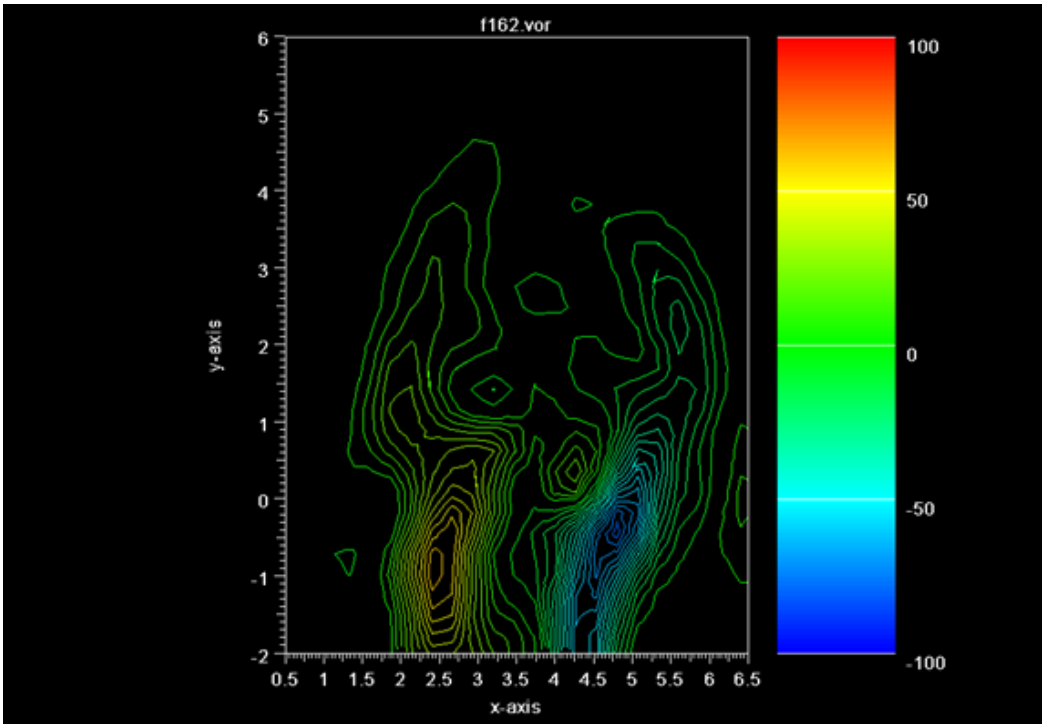

Figure 4-7. Instantaneous vorticity field during early diastolic filling of the left ventricle (shown at the same time point as for Figure 4-6). Unit for vorticity is sec^{-1}.

Figure 4-8 shows a representative velocity field during late systolic ejection. The highest magnitude velocity vectors are seen in the left ventricular outflow tract directed towards the aortic valve.

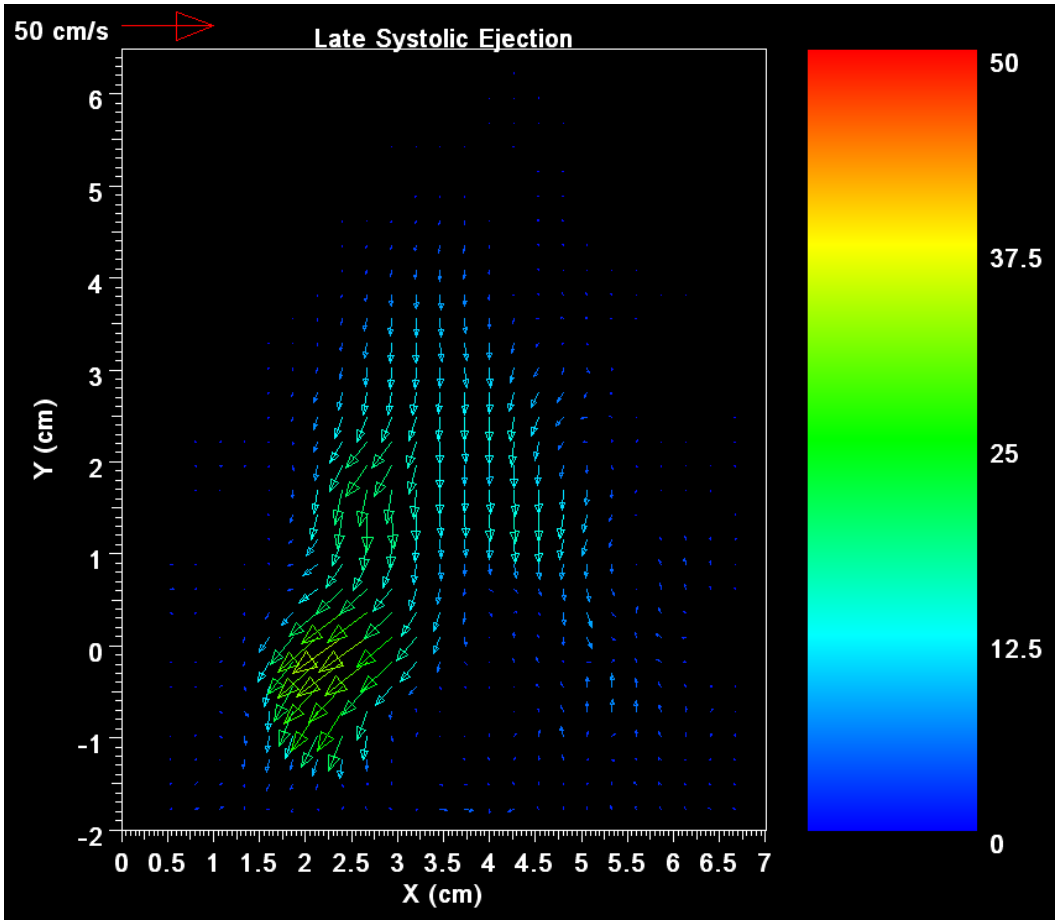

Figure 4-8. Instantaneous velocity field during late systolic ejection from the left ventricle.

E. Discussion

In an open-chest porcine model, we were able to obtain two-dimensional velocity fields as well as vorticity fields with high temporal resolution. The ability to acquire this type of data from *in vivo* imaging may provide valuable insights about left ventricular fluid dynamics that are not easily investigated using traditional imaging techniques. For instance, velocity-encoded phase-contrast magnetic resonance imaging can provide multi-component velocity vectors but has limited temporal resolution. It also requires ECG-based temporal gating, so it is likely to be inaccurate when arrhythmias are present.

The standard clinical approach currently used for determining flow velocities is Doppler echocardiography. While the temporal resolution is generally excellent, all of the different implementations of Doppler echocardiography (continuous-wave, pulsed-wave and color flow imaging) are limited to interrogation of velocities in the single dimension along the ultrasound beam direction. Each of these variations also has additional limitations. For instance, continuous-wave Doppler suffers from range ambiguity (i.e., velocities for all of the fluid elements along the interrogation line are measured.) Pulsed-wave velocity measurements will become aliased once the Nyquist limit for the pulse repetition frequency that is being used has been reached. Color flow imaging requires reduced velocity sampling durations in order to allow display overlays at reasonable frame rates onto B-mode anatomical images.

Although color flow imaging allows for spatial and temporal flow mapping, only coarse flow visualization is possible due to the unidirectional nature of the velocity measurements. The most useful clinical applications currently involve evaluation of valvular regurgitation jets and intracardiac shunts by visualizing the location, timing, and size of flow jets. High speed and turbulent jets are identified by the presence of aliasing and increased variance, respectively. Figure 4-9 shows examples of left ventricular intracavitary flow during diastolic filling and systolic ejection. While aliasing can suggest regions with increased velocities, it should be noted that detailed flow patterns cannot actually be identified in these images.

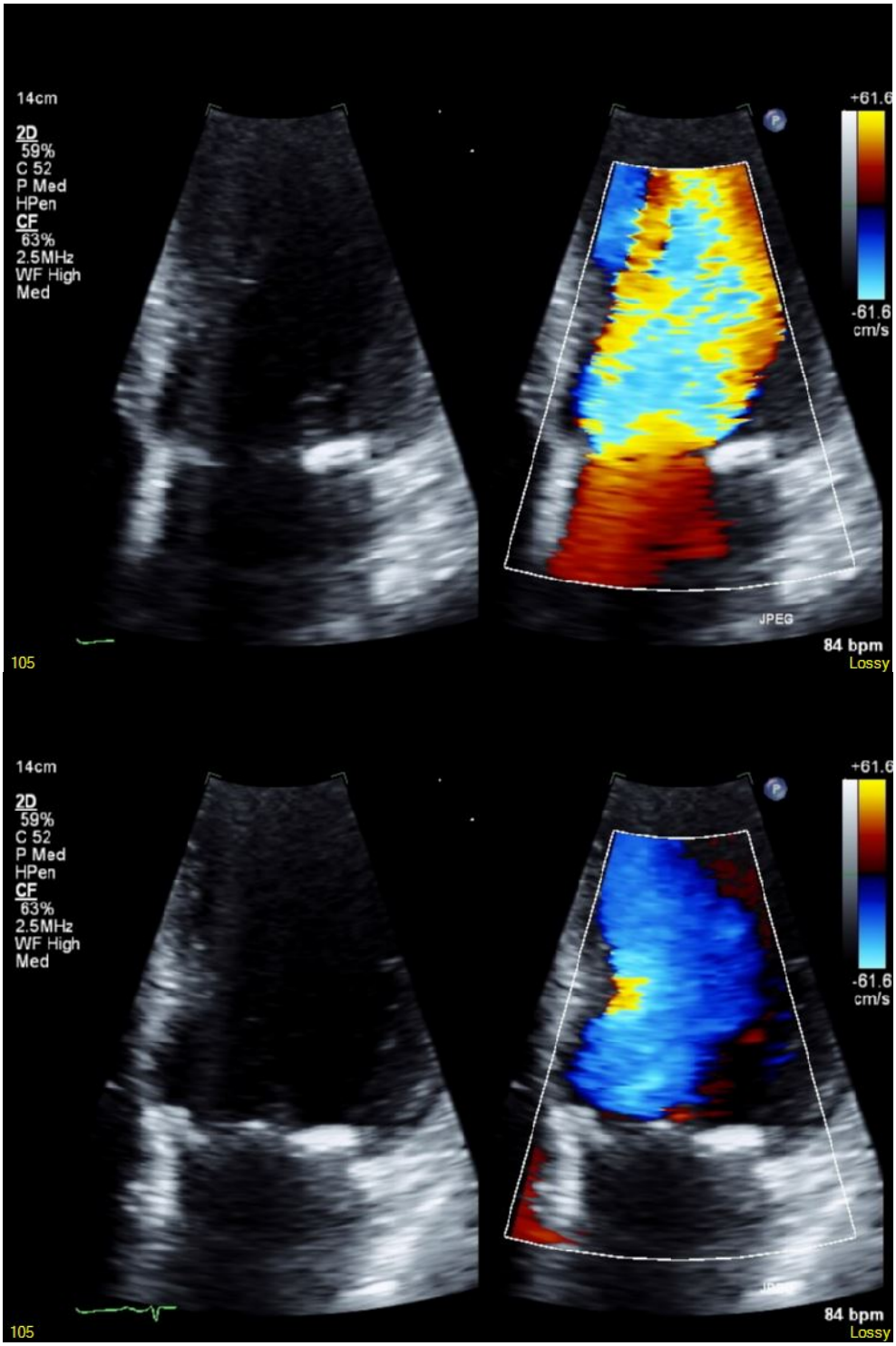

Figure 4-9. Examples of color flow imaging by echocardiography during left ventricular diastolic filling (top) and systolic ejection (bottom).

For our experiments, no true reference velocities were available for comparison. However, the normalized cross-correlation coefficients for interframe displacement estimates provided a gross measure of the expected reliability of the USIV results. Variability of the cross-correlation coefficient values was seen during the cardiac cycle. Not surprisingly, USIV appeared to be most reliable during phases of the cycle when the expected velocities were not extremely high. In contrast, USIV results were often associated with low correlation coefficients during the parts of the cycle when expected velocities were highest (specifically, peak diastole and peak systole). This finding was partially mitigated by imaging at increased frame rates. As with optical DPIV, USIV performs best when the interframe speckle pattern displacements are not large compared to the interrogation window sizes (to avoid the loss of speckles between frames). Increasing the frame rate decreases the interframe time interval and magnitude of displacements, but at the cost of having decreased sector width or depth and, therefore, a smaller region of visualization for each frame.

The interrogation window sizes used for this set of experiments were relatively large. This was related to the mean speckle sizes in the images and the goal of having at least three or four distinguishable "speckles" present in each interrogation window (Raffel et al., 2007) in order to increase the likelihood that valid displacements would be identified. In this setting, it was difficult to clearly identify vortical structures during early left ventricular filling. It is anticipated that this should become easier with advances in ultrasound instrumentation that result in improvements in effective spatial resolution. This might include advanced beamforming techniques or direct cross-correlation of backscattered radiofrequency signals rather than envelope-detected data.

While the prior *in vivo* studies using similar two-dimensional echocardiographic velocimetry approaches have identified several features of left ventricular intracavitary flow, it should be noted that the interrogation window sizes that were used were quite similar to those used here. Sengupta et al. (2007)

used windows on the order of 0.9 x 0.9 cm and Hong et al. (2008) used windows of 1.1 x 1.1 cm. Accordingly, those studies were also unable to make quantitative assessments regarding the vortex dynamics of the early diastolic inflow jet. Their most interesting findings were related to the larger scale vortical structures that were seen after the initial inflow phase.

A limitation of the current study was the use of an open-chest porcine model with median sternotomy and epicardial imaging. This model was chosen in order to evaluate USIV with ultrasound images of optimal quality. In clinical practice, however, patient-based factors such as body habitus or chronic pulmonary disease can potentially affect image quality and USIV performance. In addition, while porcine cardiovascular function is similar to that of humans, there are known differences in anatomy and physiology that could affect the translation of findings from the porcine model. Since induction and maintenance of general anesthesia can affect cardiovascular function, results also may differ somewhat from those that would be found in the awake resting state.

F. Conclusions

We performed flow visualization and USIV using open-chest epicardial echocardiography to examine *in vivo* left ventricular intracavitary flow in anesthetized pigs. Qualitative flow visualization provided initial insights on the left ventricular filling process in normal hearts. We then obtained two-dimensional velocity as well as vorticity fields with high temporal resolution. Limitations were noted regarding the length scales of flow structures that could be identified. This is most directly related to the spatial resolution available with current ultrasound systems. Excessive interframe speckle pattern decorrelation was also noted when peak blood flow velocities were present, leading to reduced USIV reliability during portions of the cardiac cycle.

Nevertheless, we demonstrated that USIV is feasible for studying *in vivo* left ventricular flow and can provide additional information when compared to the

velocimetry techniques most commonly used such as Doppler echocardiography and color flow imaging. We expect the potential utility of USIV in this setting to increase as advances are made in ultrasound instrumentation.

Chapter 5

IN VIVO EXPERIMENTS: FLOW IN THE AORTA

A. Introduction

We also performed a set of *in vivo* experiments in order to test the feasibility of the USIV technique for evaluating physiologic flow in the abdominal aorta. We used a porcine model with laparotomy followed by epiaortic imaging in order to maximize image quality. An intravenous microbubble contrast agent was injected to improve intraluminal flow visualization. Our goal was to assess whether USIV analysis could be used to obtain additional flow details beyond conventional ultrasound imaging techniques and, therefore, allow improved understanding of abdominal aortic fluid dynamics.

B. Background Related to Aortic Flow

The aorta is the blood vessel responsible for delivering oxygenated blood to the systemic circulation. Figure 5-1 shows a simplified depiction of the aorta and its major branches in humans. The aorta originates immediately distal to the aortic valve. The aortic root includes the valve leaflets and the sinuses of Valsalva. The proximal ascending aorta travels superiorly and then crosses transversely as the aortic arch. Branches originating from the aortic arch include the brachiocephalic trunk (or innominate artery), left common carotid artery, and left subclavian artery. The brachiocephalic trunk divides into the right common carotid and right subclavian arteries. After the arch, the main aortic vessel continues as the descending thoracic aorta and then as the abdominal aorta after it crosses the diaphragm. Several branches, including the right and left renal arteries, arise from the abdominal aorta before it finally divides into the right and left common iliac arteries.

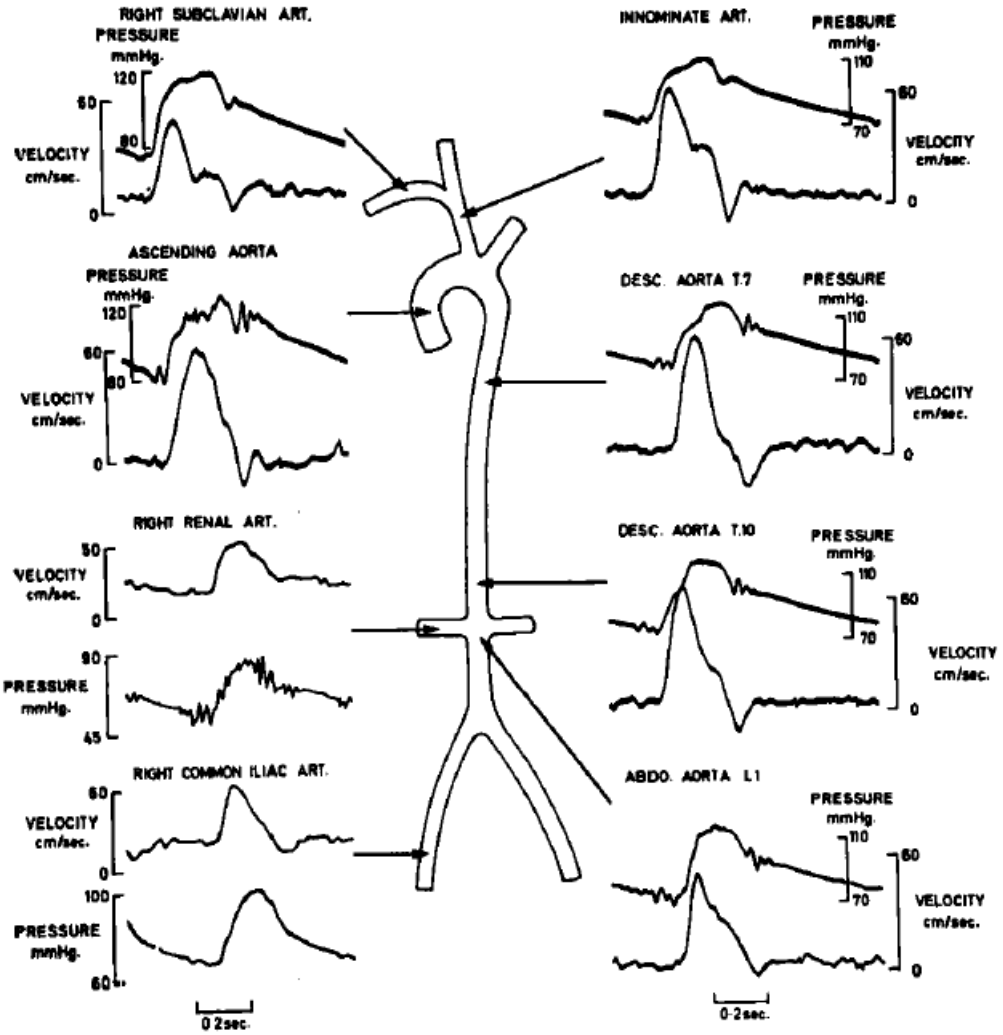

Figure 5-1. Simplified depiction of the aorta and its main branches. Pressure and velocity waveforms were measured in human subjects at various arterial sites. Reverse flow was present during part of the cardiac cycle at several locations. Reprinted with permission from Mills et al. (1970).

Throughout the arterial vasculature, blood flow is pulsatile in nature. Womersley (1955) and Hale et al. (1955) obtained an analytical solution for oscillating flow within a rigid tube and then used this to estimate arterial velocity profiles in a canine model. Figure 5-2 shows radial velocity profiles throughout

the oscillatory cycle for several different values of the Womersley number α. The Womersley number, defined below, is a dimensionless number that represents the ratio of unsteady inertial to viscous forces, defined as

$$\alpha = R\sqrt{\frac{\omega\rho}{\mu}}, \tag{5.1}$$

where R is the tube radius, ω is the angular frequency, ρ is the fluid density, and μ is the fluid viscosity. When the angular frequency and Womersley number are low, the velocity profile will intermittently bear resemblance to what is seen in fully developed Poiseuille flow. When the angular frequency and Womersley number are high, the flow does not significantly develop and the viscous boundary layers do not propagate very far from the tube wall. Typical values for the Womersley number in humans include 22.2 in the proximal aorta and 4.0 in the femoral arteries (Caro, 1978; Nichols and O'Rourke, 2005).

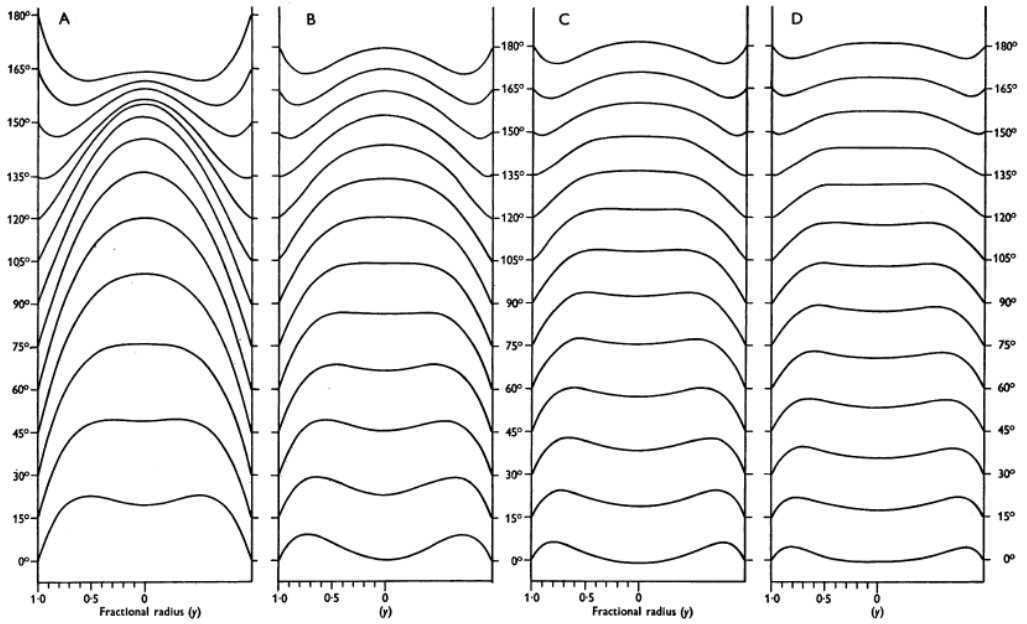

Figure 5-2. Velocity profiles for sinusoidally oscillating flow in a rigid tube for different values of Womersley number α as follows: (A) $\alpha = 3.34$, (B) $\alpha = 4.72$, (C) $\alpha = 5.78$, (D) $\alpha = 6.67$. Reprinted with permission from Hale et al. (1955).

In humans and multiple animal models, peak systolic blood pressures have been shown to increase while peak flow velocities decrease with distance along the aorta relative to the aortic valve (Nichols and O'Rourke, 2005). As shown in Figures 5-3 and 5-4, these waveforms undergo changes in contour and times to peak values as distance from the aortic valve increases. In certain locations and under certain conditions, reverse flow can be seen during ventricular diastole. This is shown in Figure 5-1 and is highly related to wave reflections from distal arterial sites (although severe aortic valve regurgitation can also contribute if present).

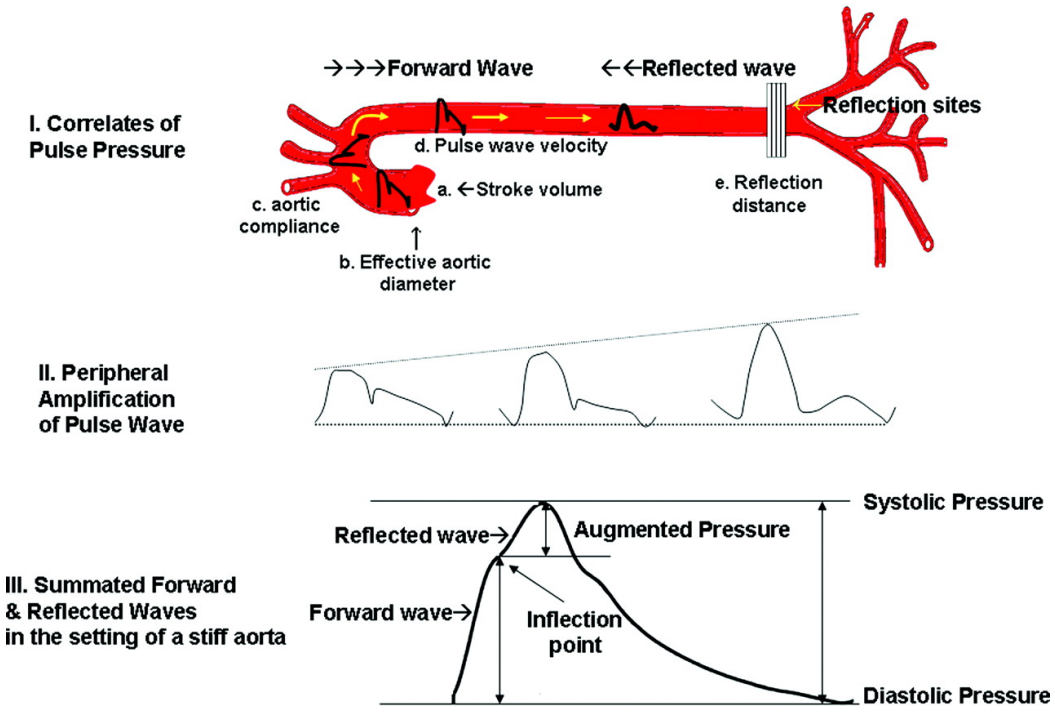

Figure 5-3. Illustration of pressure waveform changes along the arterial tree. Multiple factors are involved such as aortic size and compliance as well as wave reflections from distal sites. A typical pressure waveform from an individual with a stiff aorta is shown. Reprinted with permission from Vasan (2008).

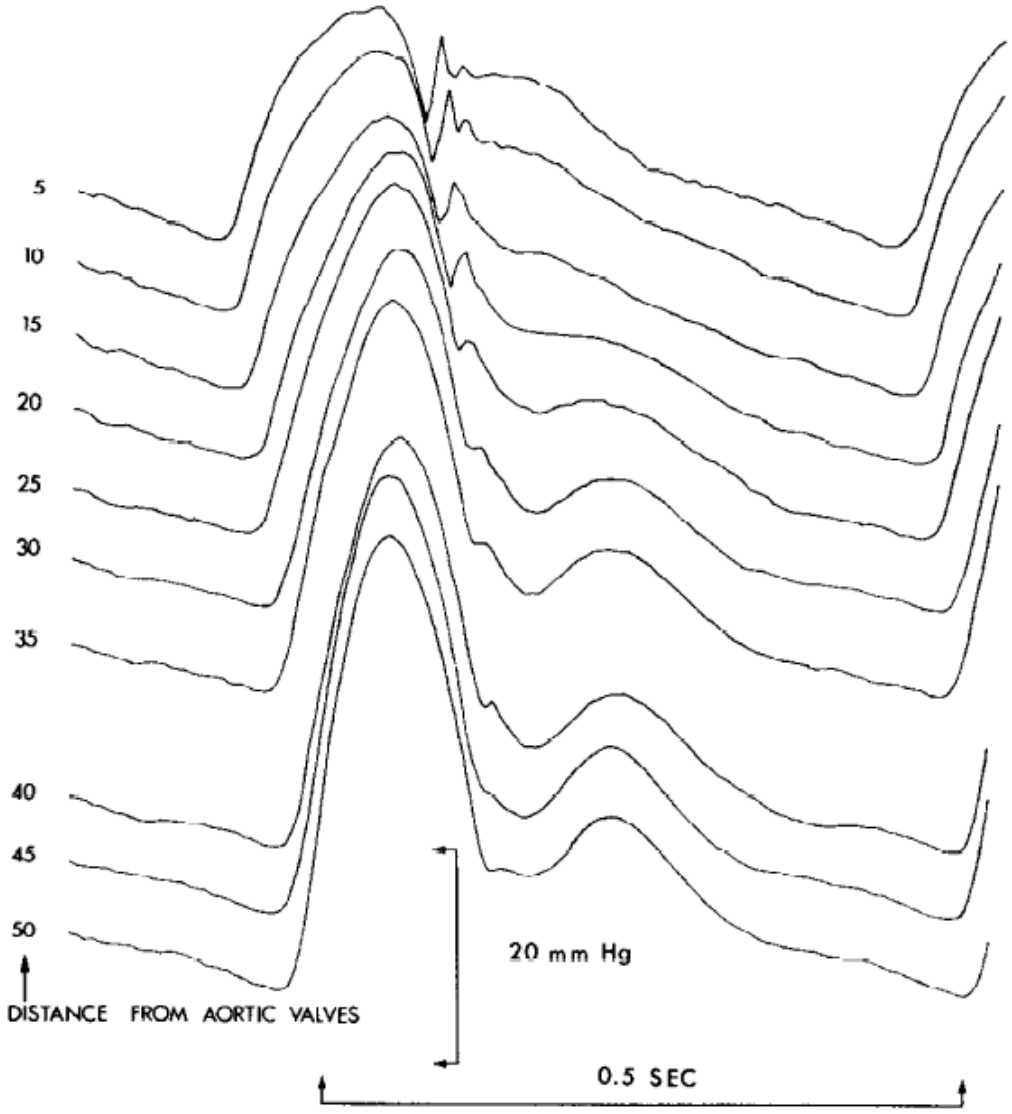

Figure 5-4. Pressure waveforms recorded in a wombat at closely spaced locations ranging from the aortic arch (top) to external iliac artery (bottom). Reprinted with permission from O'Rourke (1967).

Clearly, spatial and temporal blood flow patterns in the aorta are rather complex (Fung, 1997; Thiriet, 2008a, 2008b). The arch geometry, large branches and termination into a distal bifurcation have already been mentioned. Other anatomic details include multi-planar curvature, elastic arterial walls and tapering

of the vessel diameter in the downstream direction. In addition to unsteady flow with wave reflections, helical and retrograde flow patterns have been documented throughout the aorta.

Interestingly, both atherosclerosis and aneurysms have been associated with regions of low or oscillating wall shear stress. Such regions tend to be found at arterial branch points and bifurcations where there are often flow separation and recirculation zones. About 95% of abdominal aortic aneurysms are found to occur in the infrarenal aorta, suggesting the possible contribution of hemodynamic factors specific to that region. Multiple *in vitro*, *in vivo*, and computational studies have observed that the posterior wall of the infrarenal aorta is also typically subjected to oscillating wall shear stress due to significant periods of flow reversal in that region during each cardiac cycle (Kleinstreuer, 2006; Lasheras, 2007).

Moore et al. (1994) examined velocity profiles in the abdominal aorta using velocity-encoded phase-contrast MRI both *in vivo* with healthy volunteers and *in vitro* with a detailed flow model. They found bulk retrograde flow in the infrarenal aorta at end-systole and during early diastole. *In vivo* cross-sectional velocity profiles throughout the cardiac cycle (see Figure 5-5) showed that retrograde flow occurred primarily near the vessel walls and was most prominent along the posterior wall. Some degree of near-wall flow reversal was actually present for a longer portion of the cycle than was evident from the bulk flow measurements. While there was qualitative agreement between the *in vivo* and *in vitro* instantaneous velocity profiles and temporal waveforms, there were significant quantitative differences. Mean *in vivo* flow rates were two to four times higher than the corresponding *in vitro* measurements.

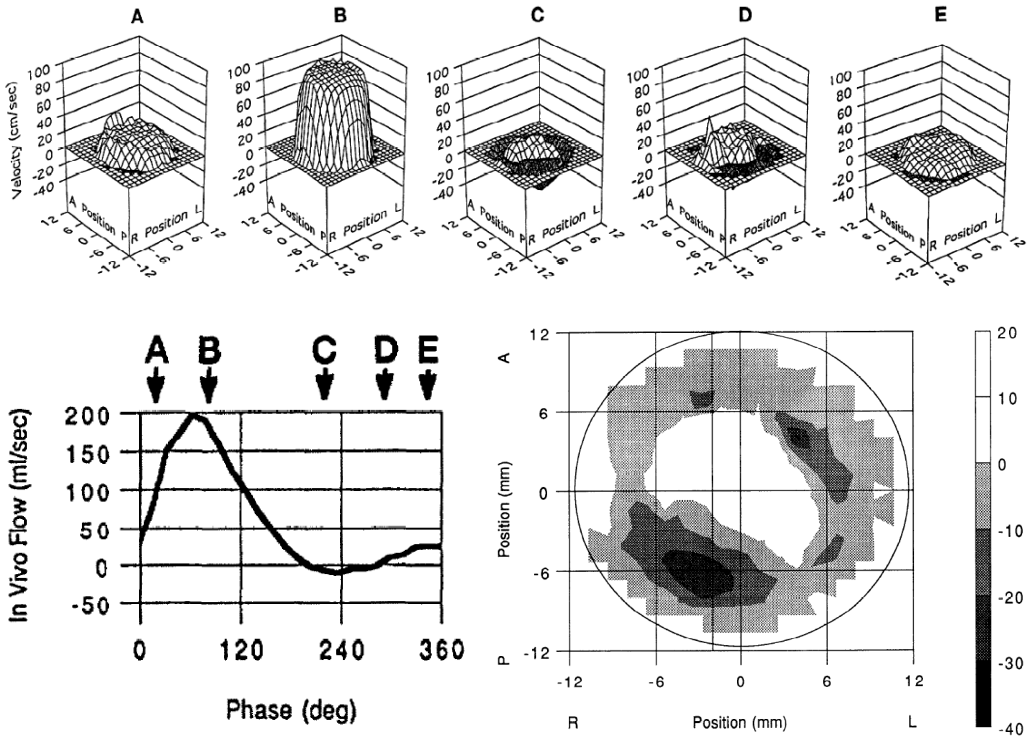

Figure 5-5. *In vivo* velocity measurements from the infrarenal aorta by velocity-encoded phase-contrast magnetic resonance imaging. Cross-sectional velocity profiles for multiple cardiac cycle phases (top panel) showed significant near-wall retrograde flow in early and mid-diastole. Mean cross-sectional velocities for the entire cardiac cycle are shown (bottom left) along with time points A-E corresponding to data in the top panel. Detailed cross-sectional velocity profile during early diastole (bottom right) showed that the most extensive retrograde flow occurred near the posterior wall. Reprinted with permission from Moore et al. (1994).

Gharib and Beizaie (2003) performed studies with an *in vitro* compliant aorta phantom that modeled the ascending aorta, aortic arch, and descending aorta without peripheral flow. They varied the stroke volume and frequency of a pulsatile pump to mimic changes in cardiac output and heart rate. This allowed them to vary Reynolds numbers from 470 to 4175 and Womersley numbers from 15.9 to 39. Descending aortic velocity fields were measured with USIV and

showed near-wall retrograde flow for a large portion of the Reynolds and Womersley number parameter space. An empiric curve could be drawn that delineated the transition between the zones with retrograde flow or no retrograde flow (see Figure 5-6). The values on this curve were converted to units of cardiac output and heart rate and then overlaid on a graph of the same parameters from clinical data for humans with and without heart failure. Interestingly, the retrograde-no retrograde transition curve matched the transition between moderate to severe heart failure (New York Heart Association [NYHA] Class III-IV) and mild or no heart failure (NYHA Class II and below). This suggested that there might be a link between the presence of retrograde descending aortic flow and the development of significant heart failure symptoms. Since it is known that endothelial dysfunction can contribute to myocardial depression (Qi et al., 1998; Qi et al., 1999), the results from Gharib and Beizaie (2003) led the authors to hypothesize that progressive heart failure may be related to endothelial dysfunction caused by negative wall shear stress.

Measuring accurate multicomponent velocities is critical to achieving a better understanding of the fluid dynamics involved in abdominal aortic flow and pathophysiology. While velocity-encoded phase-contrast MRI can provide important insights, its utility is limited due to suboptimal temporal resolution requiring ECG gating as well as the requirement for expensive scanner acquisition and maintenance costs. Conventional Doppler ultrasound techniques can only provide one-dimensional velocities and limited flow visualization. Our goal was to conduct a set of pilot experiments on animals with normal cardiovascular function in order to better understand the applicability of USIV for evaluating *in vivo* abdominal aortic flow patterns.

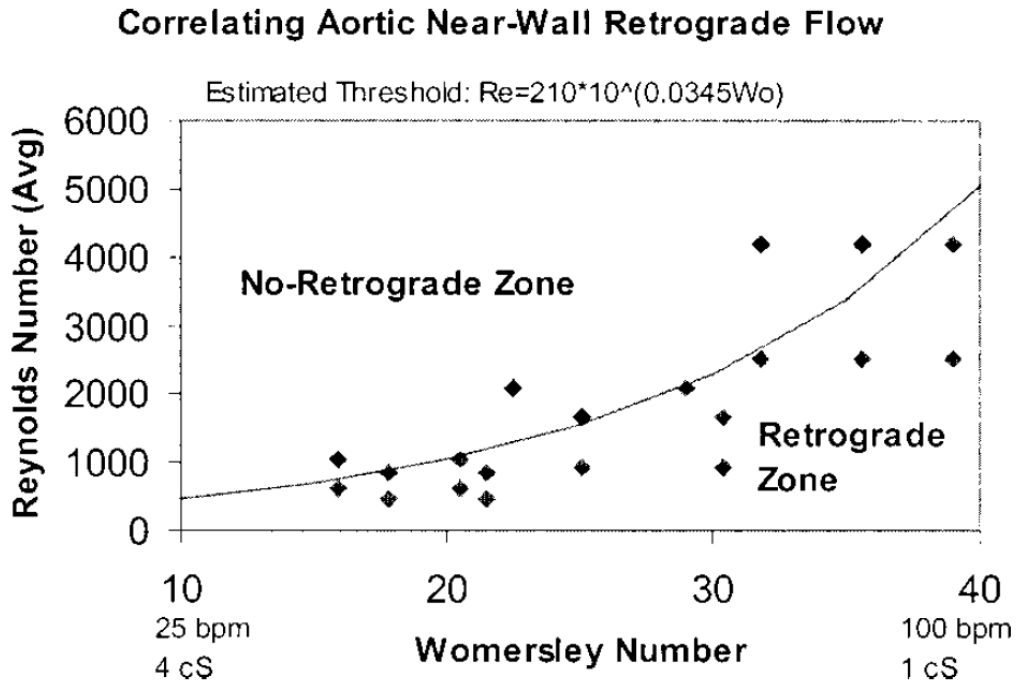

Figure 5-6. Experiments with or without observed retrograde flow plotted according to their respective Womersley and Reynold numbers. For any Womersley number, there appears to be a Reynolds number threshold above which retrograde flow is present. Reprinted with permission from Gharib and Beizaie (2003).

C. Methods

1. Animal Preparation

Two domestic pigs (average weight approximately 35 kg) were premedicated with ketamine (20 mg/kg) and atropine (0.05 mg/kg) intramuscularly and anesthetized with 1-2% inhaled isoflurane throughout the procedure. Endotracheal intubation was performed, followed by mechanical ventilation with oxygen monitoring and supplementation as necessary. Invasive arterial pressure measurements were obtained after carotid artery cannulation. A Doppler-based perivascular flow probe was placed around the infrarenal abdominal aorta (approximately 2 cm inferior to the renal arteries for the first pig

and 5 cm inferiorly for the second pig) to allow measurement of mean volumetric flow rates. The flow probe was attached to a Triton Model 100 flowmeter (Triton Technology, San Diego, CA). Hemodynamic signals were recorded using a BIOPAC MP100 system with AcqKnowledge software version 3.7.2 (BIOPAC Systems, Santa Barbara, CA). A median sternotomy was performed in order to allow direct epiaortic access. As part of a concurrent experiment, the first pig had a right femoral arteriovenous anastomosis with fistula creation prior to ultrasound imaging. That animal also was hypotensive before and during ultrasound imaging.

The experimental protocol was approved by the Institutional Animal Care and Use Committee at the University of California at Irvine. All animals received humane care in compliance with the Guide for the Care and Use of Laboratory Animals (1996).

2. Ultrasound Imaging

Epiaortic ultrasound imaging of the infrarenal abdominal aorta was performed in a sagittal longitudinal plane centered at approximately 4 cm inferior to the renal arteries for the first pig and 7 cm inferiorly for the second pig. B-mode and color flow images were obtained using a GE Vingmed System FiVe ultrasound machine (GE Vingmed Ultrasound, Horten, Norway) and a 2D flat phased array transducer (with beam steering) at up to 452 frames/sec with center frequency at 8 MHz.

To allow intraluminal aortic flow visualization, intravenous microbubble contrast consisting of perflutren (octafluoropropane) gas in an albumin shell (Optison, Amersham Health, Princeton, NJ) was injected in 0.5 mL boluses. As described in Porter et al. (2001), animals were prophylactically given ketorolac 60 mg IV and methylprednisolone 40 mg IV to prevent pulmonary hypertension.

3. USIV Analysis

B-mode ultrasound cineloop files in Digital Imaging and Communications in Medicine (DICOM) format were converted to sequenced individual bitmap images using EchoMAT software version 2.0 (GE Vingmed Ultrasound, Horten, Norway). This script was used with MATLAB software version 5.3 (The MathWorks, Inc., Natick, MA). Processing included scan conversion of the image scan line data from polar coordinates (as initially acquired by the phased array transducer) to Cartesian coordinates for further analysis.

The scan converted images were imported into a particle image velocimetry (PIV) software package for further analysis (PIVview version 3, PIVTEC, Gottingen, Germany). Image pairs were chosen using interframe intervals that optimized the displacement magnitudes relative to the sampling window dimensions. Displacement and velocity vectors were calculated using a Fast Fourier Transform (FFT)-based cross-correlation algorithm. Interrogation was performed using 128 x 32 pixel sampling windows (corresponding to a physical window size of approximately 0.50 x 0.13 cm). The step size was 32 x 16 pixels. The sampling window size was chosen to balance the need to have distinguishable speckle pattern features that were present within that window for both frames of each image pair while trying to preserve spatial resolution. Correlation-based correction was performed by detecting peaks after multiplication of adjacent correlation planes offset by 32 x 16 pixels. Correlation peaks were detected using a three-point Gaussian fit and outlier detection was performed. Further details regarding these procedures can be found in Willert and Gharib (1991), Hart (2000), and Raffel et al. (2007). Instantaneous velocities within a central region of interest (in order to avoid edge artifacts) were calculated throughout the cardiac cycle.

D. Results

Contrast ultrasound imaging allowed both qualitative and quantitative flow visualization within the infrarenal abdominal aorta. Figure 5-7 shows a representative image.

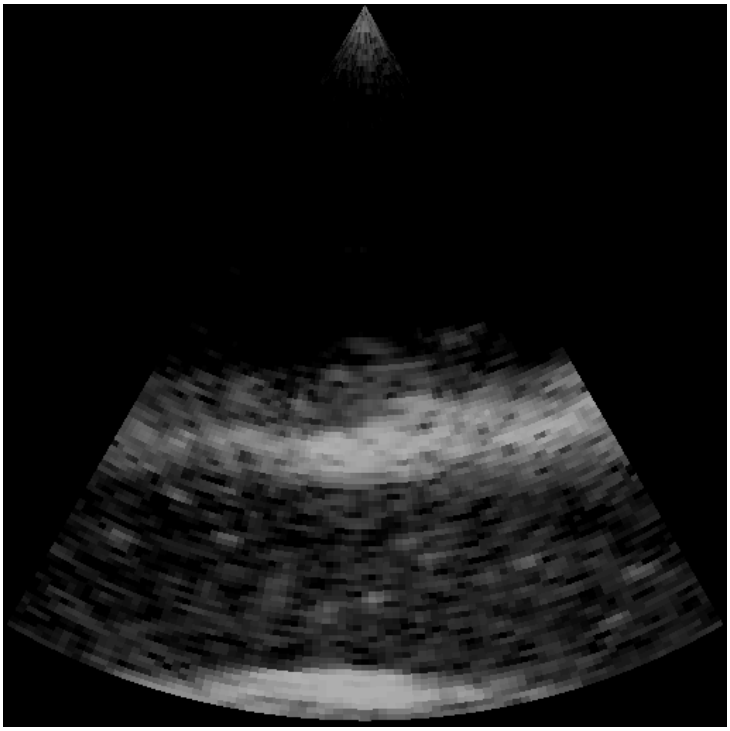

Figure 5-7. Contrast ultrasound image exported with EchoMAT showing epiaortic flow visualization of the infrarenal abdominal aorta from the second pig in this study.

Qualitative and quantitative flow visualization revealed differences in the infrarenal flow patterns between the two animals. For the first pig, forward flow appeared throughout the imaging plane during early systole and reached peak velocity at mid-systole. It then gradually decreased in speed through late systole. In early diastole, low velocity forward flow was initially present throughout the vessel and then slowed down to become relatively stagnant. During mid-diastole, low velocity reverse flow started in the posterior half of the vessel and then was

seen throughout the vessel. Reverse flow continued to be present through late diastole until suddenly being replaced with forward flow after the onset of the next ventricular systole.

Figure 5-8 shows a representative velocity vector field from the infrarenal abdominal aorta during late systole at a heart rate of 93 bpm. There was unidirectional flow in the forward direction with decreased velocities near the vessel walls. Figure 5-9 shows a representative velocity vector field during late diastole. The pattern of retrograde flow was essentially axisymmetric.

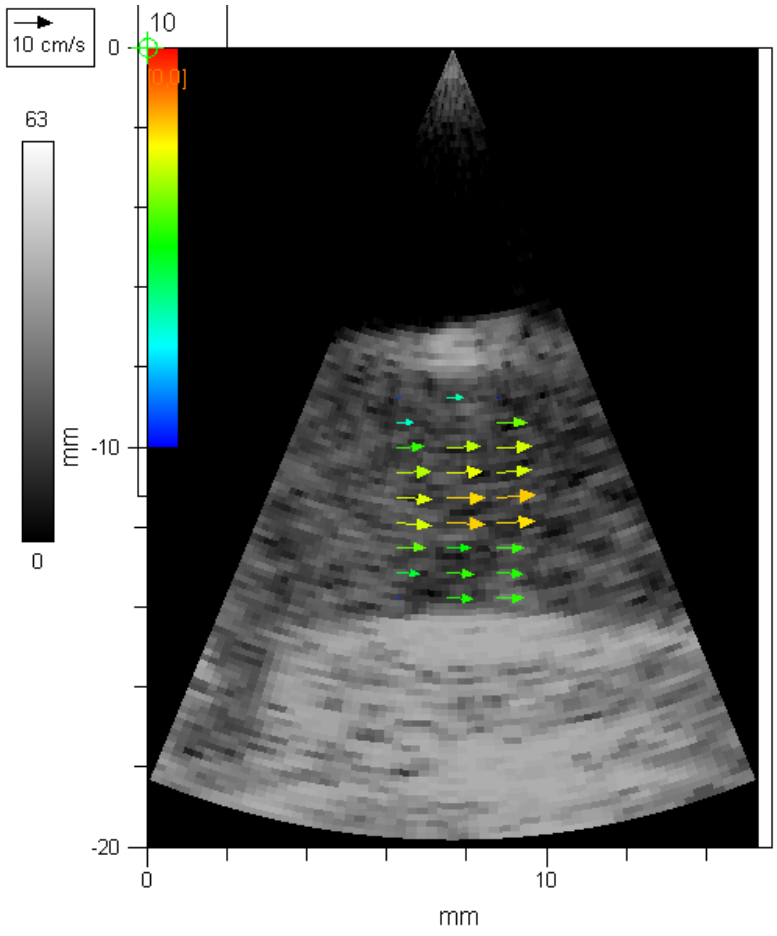

Figure 5-8. Velocity field from infrarenal abdominal aorta during late systole from the first pig in this study. There was unidirectional flow in the forward direction.

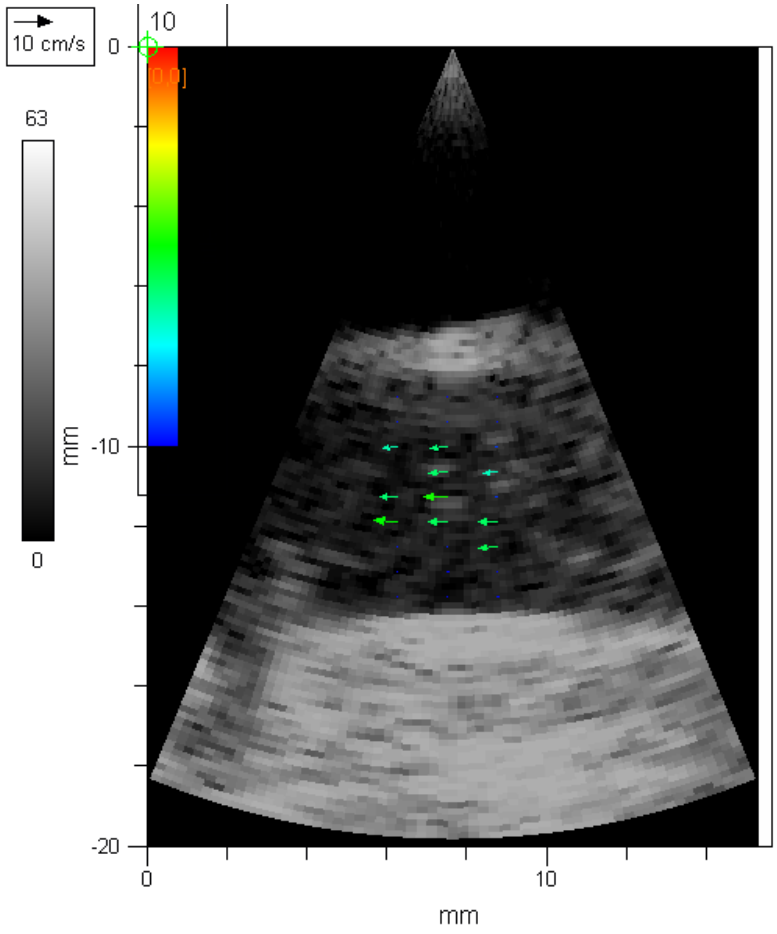

Figure 5-9. Velocity field from infrarenal abdominal aorta during late diastole for the first pig in this study. There was retrograde flow with an axisymmetric velocity profile.

For the second pig, forward flow appeared throughout the imaging plane during early systole and reached peak velocity at mid-systole. It then gradually decreased in speed through late systole. During early diastole, low velocity forward flow continued to be present in most of the vessel, but a thin layer of reverse flow was noted at the posterior wall of the aorta. The area of the imaging plane with reverse flow gradually grew larger and, by mid-diastole, there were nearly equal areas of forward flow anteriorly and reverse flow posteriorly. By late

diastole, reverse flow was no longer present and there was low velocity forward flow throughout the vessel.

Figure 5-10 shows a representative velocity vector field from the infrarenal abdominal aorta during early systole at a heart rate of 104 bpm. There was unidirectional forward flow with decreased velocities near the vessel walls. Figure 5-11 shows a velocity vector field during late diastole. The pattern of retrograde flow was asymmetric and located posteriorly in the presence of concurrent forward flow in the anterior portion of the vessel.

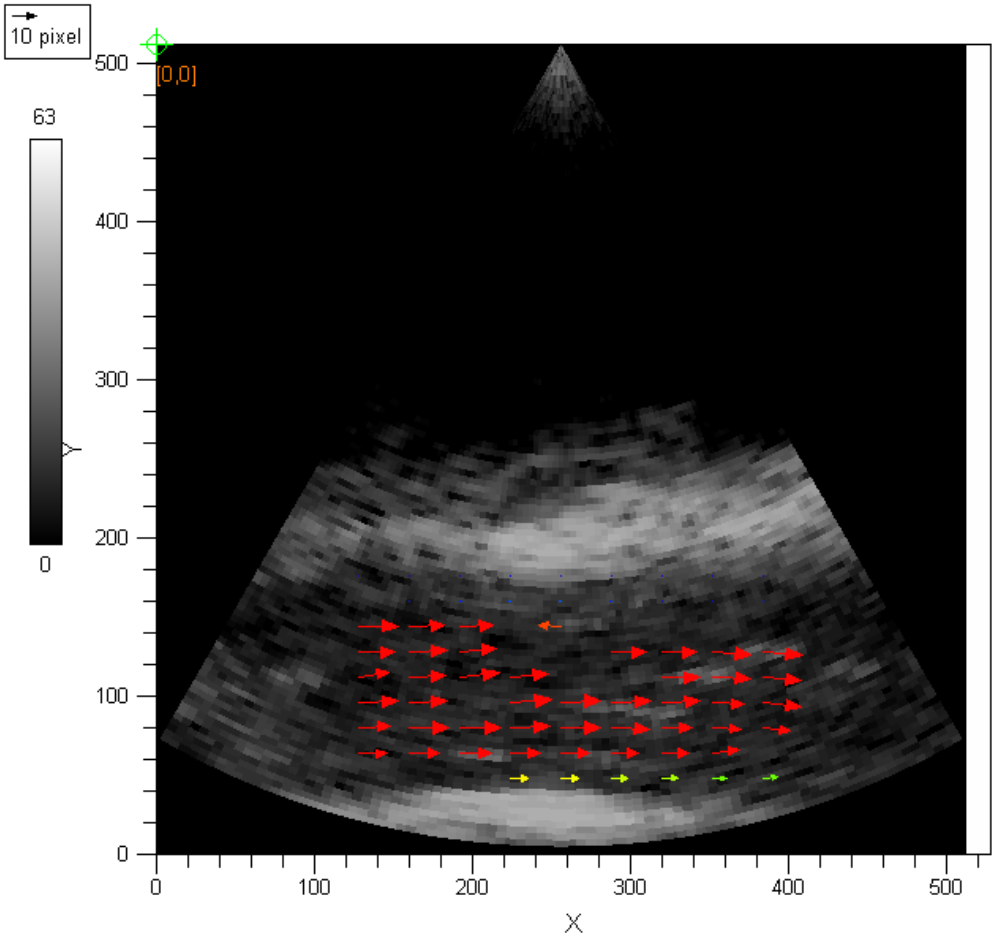

Figure 5-10. Velocity field from infrarenal abdominal aorta during early systole for the second pig in this study. There was unidirectional forward flow.

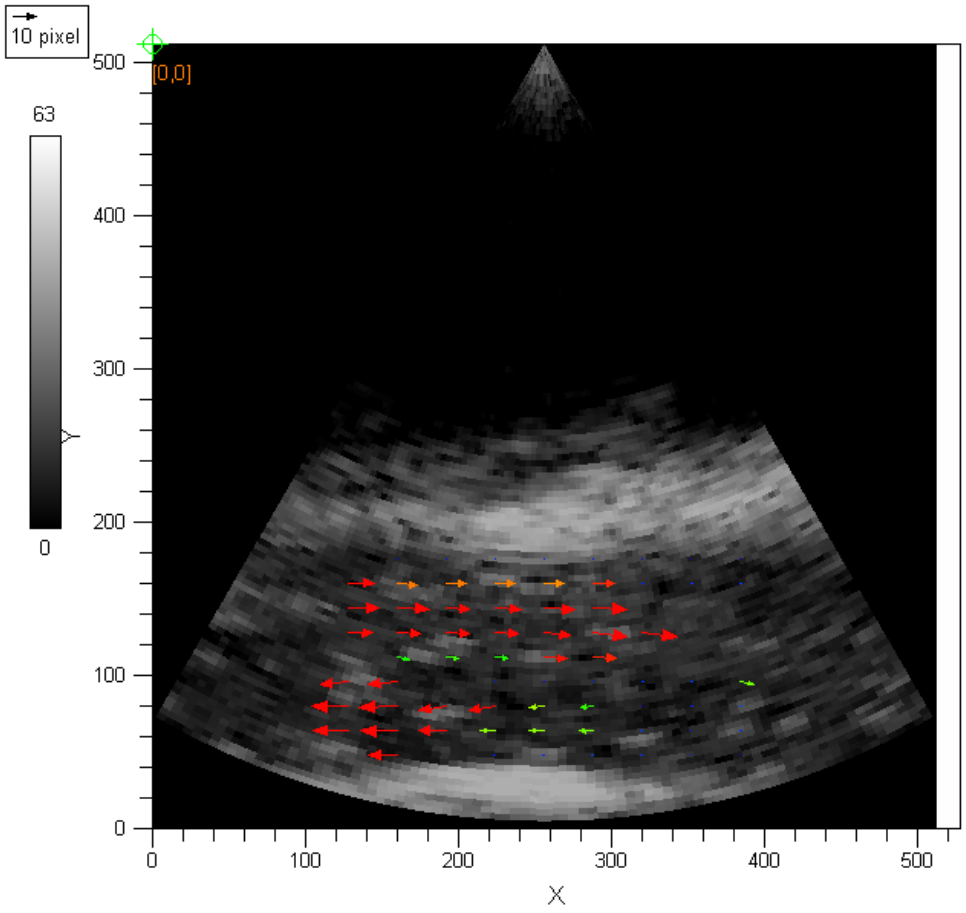

Figure 5-11. Velocity field from infrarenal abdominal aorta during mid-diastole for the second pig in this study. There was an asymmetric velocity profile with retrograde flow located posteriorly.

E. Discussion

To our knowledge, this is the first demonstration in the abdominal aorta of contrast ultrasound-based flow visualization and the acquisition of non-temporally gated multicomponent velocities from ultrasound imaging. As was the case for intracavitary left ventricular flow, we were able to visualize significantly more information about the spatial flow patterns in the infrarenal aorta compared to standard color flow imaging. Figure 5-12 shows an example of color flow imaging of the abdominal aorta near the renal arteries. Flow pattern observations

are generally limited to bulk flow directionality, either towards (red) or away (blue) from the transducer, and the presence of aliasing that suggests high velocities and possible stenosis. If flow is directed perpendicularly to the transducer at any location, its appearance will transition from appearing red to blue (or vice versa) and this may complicate proper flow pattern interpretation.

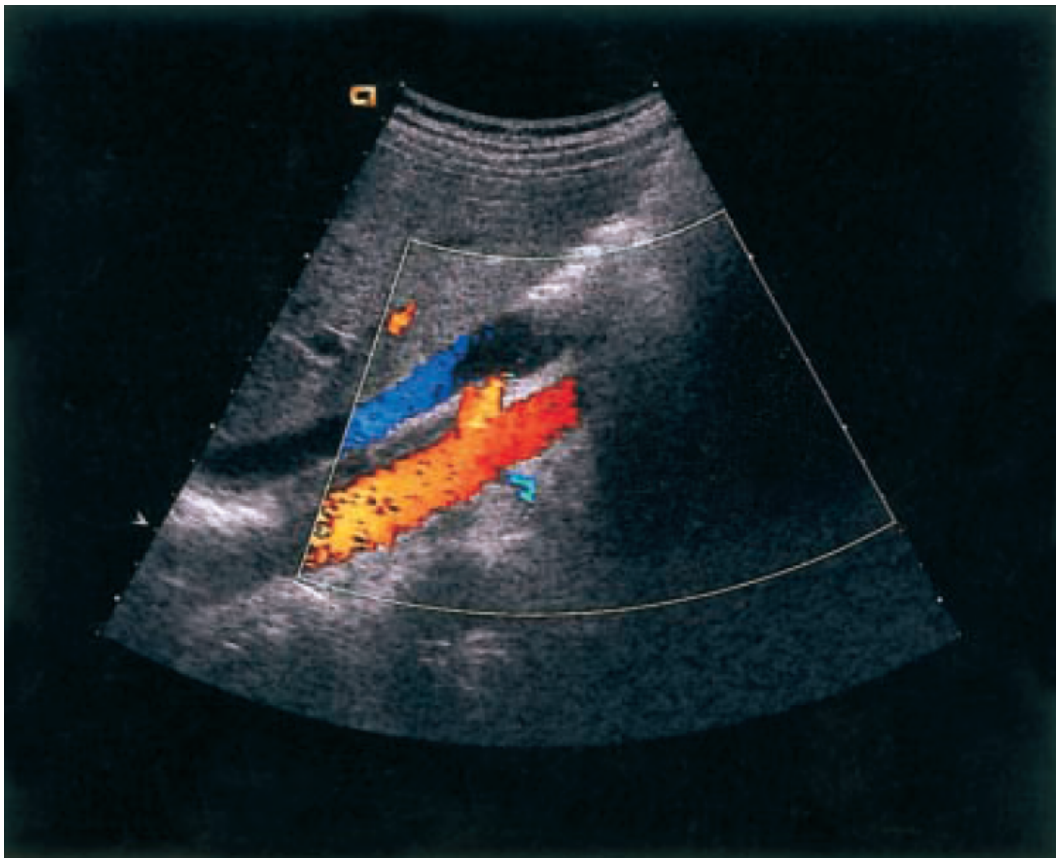

Figure 5-12. Example of color flow imaging of the abdominal aorta (large red vessel with flow directed towards the transducer at the top of the image). Right renal artery (small red vessel) and left renal artery (small blue vessel) are seen branching off from the aorta. Inferior vena cava is also seen (large blue vessel). Reprinted with permission from Zubarev (2001).

With USIV, however, we were able to discern subtle differences between test subjects regarding infrarenal flow patterns, especially with regards to the location and timing of retrograde flow. We were also able to avoid the restrictions on imaging angle that usually apply to vascular velocity measurements (since Doppler measurement accuracy is only good when insonification angles are far from perpendicular, even when using angle correction).

In our experiments, we observed the presence of two different infrarenal flow patterns. Both of these patterns differ from those most widely reported in the prior literature. The first pig in this study had retrograde flow that started posteriorly in mid-diastole, but then became axisymmetric throughout the vessel for the rest of mid- and late diastole. The second pig in this study had retrograde flow that started in a small posterior near-wall layer that appeared in early diastole and then grew to become part of an asymmetric velocity profile with simultaneous forward flow anteriorly and retrograde flow posteriorly.

There are several flow phenomena that can contribute to the presence of retrograde flow at a particular location. The first one, Womersley flow, was described in section 5.B and results from viscous flow being driven by an oscillatory pressure gradient. Whether the axisymmetric retrograde flow occurs mostly near the walls or throughout the vessel is dictated by the Womersley number. The original model (Womersley, 1955) assumed that arteries were rigid tubes and did not account for the effects of wave propagation, although this factor will clearly influence flow characteristics.

Other situations can result in boundary layer separation due to an adverse pressure gradient. A recirculation zone with retrograde flow is formed in the region where the viscous boundary layer becomes detached from the wall. The most common physiologic examples involve rapid increases in cross-sectional area such as those occurring at arterial bifurcations or distal to stenoses from large atherosclerotic plaques.

Another setting where boundary layer separation can occur is for a low resistance capillary bed (e.g., within a kidney) located proximally to induce reverse flow from a distal source (such as the infrarenal abdominal aorta) during part of the cardiac cycle. In this case, flow separation of the antegrade boundary layer is caused by inlet, outlet, and wave propagation conditions for the abdominal aorta that lead to retrograde suction by the renal arteries.

It is likely that all of the factors described above can make contributions in causing retrograde flow in the aorta. The two animals in this study may have had different infrarenal flow patterns due to varied hemodynamic conditions that altered the relative contributions of these factors. The axisymmetric retrograde flow for the first pig was consistent with a Womersley-type flow. The highly asymmetric posterior retrograde flow for the second pig may have been more strongly influenced by wave propagation dynamics.

Infrarenal abdominal aortic flow has been evaluated using *in vitro*, *in vivo*, and computational models (Chandran, 2001). Most studies have supported the presence of retrograde flow under certain conditions, but have varied slightly regarding the details. As described in Section 5.B, Moore et al. (1994) performed MRI of an *in vitro* model as well as human volunteers. They found that retrograde flow occurred at end-systole and during early diastole, mostly near the vessel walls (especially posteriorly). Taylor et al. (2002) also performed *in vivo* MRI on volunteers and described reverse flow appearing in early diastole near the walls. Reverse flow no longer appeared during steady-state bicycle exercise. Pedersen at al. (1999) used pulsed-wave Doppler ultrasound in a porcine model. They observed that, along an angled anterior-to-posterior line of interrogation points, retrograde flow also occurred near the walls (especially posteriorly) and mostly in early diastole.

Taylor et al. (1998) developed a computational model of pulsatile flow in an idealized abdominal aorta. They noted the development of a large recirculation zone along the posterior wall of the infrarenal aorta. Oscillatory shear index

values were calculated for the anterior and posterior walls over the entire abdominal aorta and were highest in the infrarenal region. The midplane velocity profiles demonstrated retrograde flow at times along both the anterior and posterior infrarenal walls. All of the infrarenal aortic walls, though, had low mean shear stresses that were consistent with oscillating flow.

We found only one study (Bogren and Buonocore, 1994) that described infrarenal retrograde flow as being limited to the posterior of the aorta during *in vivo* MRI scans of healthy subjects without cardiovascular risk factors. Figure 5-13 shows a representative image from that study where the posterior region with retrograde flow only occupies a small portion of the luminal cross-sectional area.

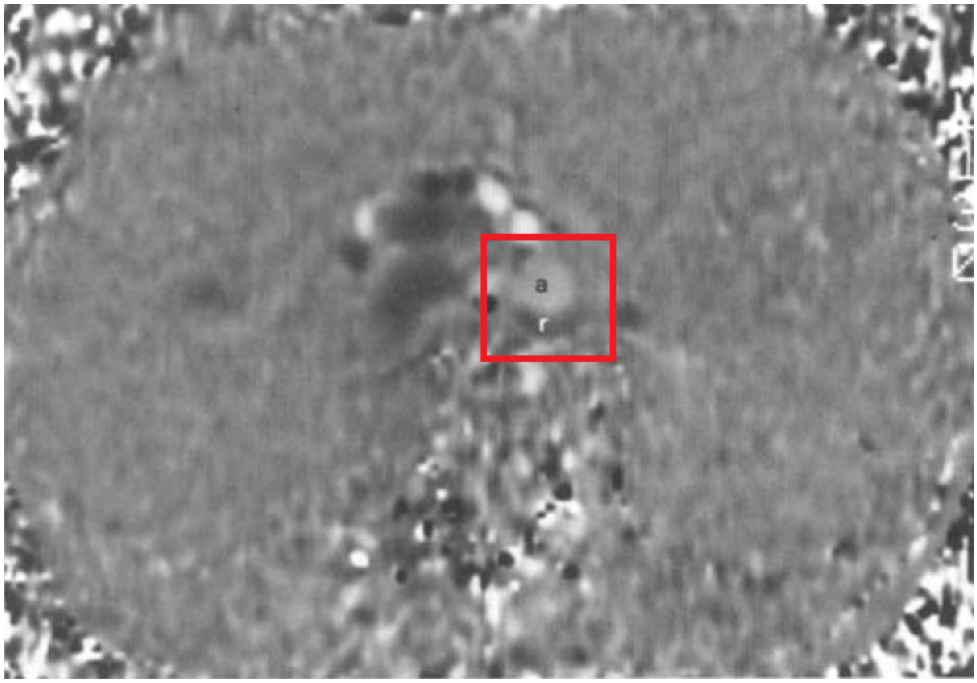

Figure 5-13. Velocity map derived from velocity-encoded phase-contrast MRI of the infrarenal abdominal aorta during early diastole in a healthy volunteer. The cross-sectional area of the vessel (within red rectangle) consisted of a large anterior region with antegrade flow (labeled as *a*) and a small posterior region with retrograde flow (labeled as *r*). Adapted with permission from Bogren and Buonocore (1994).

We were not able to find any studies that precisely described the infrarenal abdominal aortic flow patterns that we saw in our porcine experiments. Specifically, in the first pig, we saw axisymmetric retrograde flow that involved the entire vessel during mid- to late diastole. In the second pig, there was highly asymmetric posterior retrograde flow during early and mid-diastole involving up to half of the vessel. While our sample size for this pilot study was too small to support definitive conclusions, it is interesting to consider possible explanations for the differences compared with prior results in the literature.

To our knowledge, there have been no reports of multicomponent velocity profiles within the infrarenal abdominal aorta. Prior studies of the abdominal aorta with velocity-encoded MRI have reported only through-plane velocities for cross-sections at different aortic levels and have generally been conducted in humans. There is a relevant anatomic distinction involving the aorta that, in humans, terminates in a bifurcation with right and left common iliac arteries that each give off external and internal iliac branches. In pigs, there are two distal trifurcations involving the abdominal aorta. The first consists of three large branches including the right and left external iliac arteries as well as a large midline vessel alternatively referred to as the distal abdominal aorta or as the median sacral artery (Schummer et al., 1981; Strauch, 2007). As shown in Figure 5-14, this midline vessel quickly trifurcates again to give off the right and left internal iliac arteries and eventually continues into the tail as the median caudal artery.

While interspecies anatomic and physiological differences could contribute to varied aortic flow, it is also interesting that the two pigs in our study had distinct infrarenal flow patterns. The first pig did have a femoral arteriovenous fistula leading to some degree of continuous arterial to venous shunting distal to the infrarenal abdominal aorta. A distal shunt, however, would be expected to reduce the amount of retrograde flow and increase antegrade flow through the abdominal aorta. Another factor was that the first pig was relatively

hypotensive throughout the experiment compared to the second pig. This certainly may also have contributed to the interanimal differences.

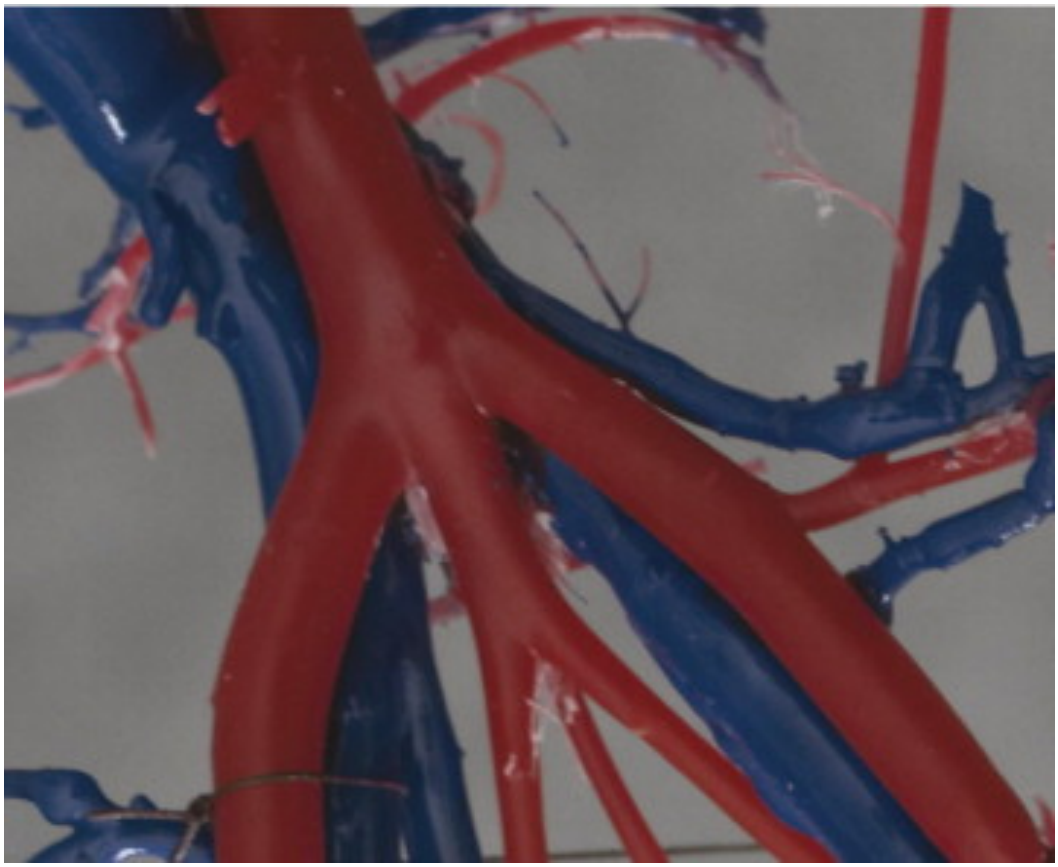

Figure 5-14. Pigmented polymer casts of porcine arterial (red) and venous (blue) vasculature showing two trifurcations involving the distal abdominal aorta. Reprinted with permission from Strauch (2007).

Technical factors may play a role in the differences compared with prior published results. MRI has much poorer temporal resolution than ultrasound imaging and transient flow phenomena may not be fully captured. Our current implementation of USIV is a two-dimensional technique and, therefore, can be sensitive to alignment of the imaging plane. Aortic flow is known to have important three-dimensional features, such as helical flow, that may appear

different in one longitudinal plane compared to another. It should be noted that none of the MRI studies described above evaluated velocities in a longitudinal plane.

The fact that neither of the infrarenal flow patterns seen in our experiments has been described in humans could potentially reflect interspecies differences. It is worth noting, though, that prior reports of *in vivo* human MRI studies of the abdominal aorta have mostly involved young and healthy volunteers with no known cardiovascular disease. It is possible that humans could also show similar patterns of infrarenal flow under hemodynamic conditions associated with reduced cardiac output. This would be consistent with the results from Gharib and Beizaie (2003) correlating significant retrograde flow with advanced heart failure symptoms. As mentioned before, the first pig in the current study was relatively hypotensive and, interestingly, had more severe retrograde flow that involved the entire vessel.

No true reference velocities were available for comparison in these experiments. However, the normalized cross-correlation coefficients for interframe displacement (and associated velocity) estimates provided a gross measure of the expected reliability of the USIV results obtained. Variability of the cross-correlation coefficient values was seen during the course of the cardiac cycle. Not surprisingly, USIV appeared to be most reliable during phases of the cycle where the expected velocities were not extremely high. In contrast, USIV results were often associated with low cross-correlation coefficient values during peak systole (when the expected velocities were highest). This finding was mitigated by imaging at increased frame rates. As with optical DPIV, USIV performs best when the interframe speckle pattern displacements are not large compared to the interrogation window sizes (to avoid the loss of speckles between frames). Increasing the frame rate decreases the interframe time interval and magnitude of displacements, but at the cost of having narrower sector widths and, therefore, less spatial information for each frame.

The interrogation window sizes used for this set of experiments were relatively large. This was related to the mean speckle sizes in the images and the goal of having enough distinguishable "speckles" present in each interrogation window in order to increase the likelihood that valid displacements would be identified. The interrogation window length was made significantly larger in the flow direction to avoid interframe loss of speckles due to the high velocities expected at peak systole. This, of course, lead to decreased spatial resolution of the resulting velocity field. It is anticipated that advances in ultrasound instrumentation may result in improvements in effective spatial resolution. This might include advanced beamforming techniques or direct cross-correlation of backscattered radiofrequency signals rather than envelope-detected data.

A limitation of the current study was the use of a porcine model with laparotomy and epiaortic imaging. This model was chosen in order to evaluate USIV with ultrasound images of optimal quality. In clinical practice, however, patient-based factors such as body habitus or chronic pulmonary disease can potentially affect image quality and USIV performance. In addition, while porcine cardiovascular function is similar to that of humans, there are known differences in anatomy and physiology that could affect the translation of findings from the porcine model. Since induction and maintenance of general anesthesia can affect cardiovascular function, results also may differ somewhat from those that would be found in the awake resting state.

F. Conclusions

We performed flow visualization and USIV using an anesthetized porcine model with laparotomy and epiaortic ultrasound imaging. To our knowledge, this is the first documentation of multicomponent velocity data in the infrarenal aorta. We observed varied flow patterns in the two animal subjects that may have reflected different hemodynamic conditions with altered wave propagation and flow separation dynamics. These infrarenal flow patterns have not previously

been identified in healthy humans using other velocimetry methods, but may provide insight into the pathophysiology of heart failure, atherosclerosis, and aneurysm formation.

Chapter 6

SUMMARY

The study of cardiovascular fluid mechanics is of vital importance to advancing knowledge about pathologic processes as well as improving medical device design. There are many limitations to routinely used techniques, such as Doppler ultrasound and magnetic resonance imaging, for measurement of *in vivo* blood flow velocities and visualization of flow patterns. Ultrasound speckle tracking approaches have been explored to obtain multicomponent velocity fields, but further understanding of the factors that affect accuracy will be critical to enabling widespread application of such techniques.

In this work, we studied a speckle tracking implementation that we refer to as ultrasound speckle image velocimetry (USIV). This technique involves using algorithms developed for digital particle image velocimetry (DPIV) of optical images and directly applying these to ultrasound images obtained with a commercially available system and transducer.

In the first set of experiments, we validated the USIV technique using uniform translation of a speckle phantom at known velocities. Overall, USIV performed well and very good agreement was seen compared with reference values. Standard sources of error that affect DPIV with optical images were confirmed to be relevant with USIV. Additional factors specific to the use of ultrasound-derived images were also identified. For any specific ultrasound imaging arrangement, there is likely an optimal focal depth in terms of achieving the best overall accuracy throughout the image. Theoretically, there will also be an effect related to sequential ultrasound beam scanning, but this may only be important when scatterer velocities are high relative to beam sweep speeds (or frame rates).

The second set of experiments involved creating a transparent flow phantom apparatus that allowed both ultrasound and optical imaging to be performed. The USIV technique produced velocity estimates that were fairly similar to those obtained using the reference standard of DPIV for an *in vitro* experimental setup with simple, but physiologically interesting, features that simulated arterial curvature and stenosis. The setup also allowed testing with a non-axisymmetric velocity profile that led to the presence of velocity gradients within the USIV interrogation windows. We found that USIV accuracy was slightly decreased in the near-field region and that the optimal focal depth appeared to be near the center of the overall region of interest.

In the third set of experiments, we performed flow visualization and USIV using open-chest epicardial echocardiography to examine *in vivo* left ventricular intracavitary flow in anesthetized pigs. Qualitative flow visualization provided initial insights on the left ventricular filling process in normal hearts. We demonstrated the feasibility of obtaining two-dimensional velocity as well as vorticity fields with high temporal resolution. Limitations were noted regarding the length scales of flow structures that could be identified due to the spatial resolution of ultrasound imaging. Excessive interframe speckle pattern decorrelation was also noted when peak blood flow velocities were present, leading to reduced USIV reliability during portions of the cardiac cycle.

The fourth, and last, set of experiments involved performing flow visualization and USIV using an anesthetized porcine model with laparotomy and epiaortic ultrasound imaging. To our knowledge, this is the first documentation of multicomponent velocity data in the infrarenal aorta. We observed varied flow patterns in the two animal subjects that may have reflected different hemodynamic conditions with altered wave propagation and flow separation dynamics. The most interesting finding was the presence in certain cases of highly asymmetric retrograde flow in the infrarenal aorta. These flow patterns have not previously been identified in healthy humans using other velocimetry methods,

but may provide insight into the pathophysiology of heart failure, atherosclerosis, and aneurysm formation.

The overall objectives of this project included studying USIV performance under controlled *in vitro* conditions and proving the feasibility of the technique in experimental *in vivo* models relevant to cardiac and arterial fluid mechanics. USIV is likely to be very useful for further studies both *in vivo* and with *in vitro* elastic aorta models.

BIBLIOGRAPHY

Guide for the care and use of laboratory animals. (1996). The National Academies Press.

Adrian, R. J. (2005). Twenty years of particle image velocimetry. *Experiments in Fluids, 39*(2), 159-169.

Benedek, G. B., & Villars, F. (2000). *Physics, with illustrative examples from medicine and biology* (2nd ed.). New York: AIP Press.

Bogren, H. G., & Buonocore, M. H. (1994). Blood-flow measurements in the aorta and major arteries with MR velocity mapping. *JMRI-Journal of Magnetic Resonance Imaging, 4*(2), 119-130.

Bohs, L. N., Friemel, B. H., & Trahey, G. E. (1995). Experimental velocity profiles and volumetric flow via 2-dimensional speckle tracking. *Ultrasound in Medicine and Biology, 21*(7), 885-898.

Bohs, L. N., Geiman, B. J., Anderson, M. E., Gebhart, S. C., & Trahey, G. E. (2000). Speckle tracking for multi-dimensional flow estimation. *Ultrasonics, 38*(1-8), 369-375.

Bohs, L. N., & Trahey, G. E. (1991). A novel method for angle independent ultrasonic-imaging of blood-flow and tissue motion. *IEEE Transactions on Biomedical Engineering, 38*(3), 280-286.

Brigham, E. O. (1988). *The fast fourier transform and its applications*. Englewood Cliffs, N.J.: Prentice Hall.

Bryant, D. J., Payne, J. A., Firmin, D. N., & Longmore, D. B. (1984). Measurement of flow with NMR imaging using a gradient pulse and phase difference technique. *Journal of Computer Assisted Tomography, 8*(4), 588-593.

Buonocore, M. H., & Bogren, H. (1992). Factors influencing the accuracy and precision of velocity-encoded phase imaging. *Magnetic Resonance in Medicine, 26*(1), 141-154.

Caro, C. G. (1978). *The mechanics of the circulation*. Oxford ; New York: Oxford University Press.

Chai, P., & Mohiaddin, R. (2005). How we perform cardiovascular magnetic resonance flow assessment using phase-contrast velocity mapping. *Journal of Cardiovascular Magnetic Resonance, 7*(4), 705-716.

Chandran, K. B. (2001). Flow dynamics in the human aorta: Techniques and applications. In C. T. Leondes (Ed.), *Biomechanical systems : Techniques and applications* (Vol. 2. Cardiovascular techniques, pp. 5-1 to 5-25). Boca Raton: CRC Press.

Chandran, K. B., Rittgers, S. E., & Yoganathan, A. P. (2007). *Biofluid mechanics : The human circulation*. Boca Raton: CRC/Taylor & Francis.

Cobbold, R. S. C. (2007). *Foundations of biomedical ultrasound*. Oxford ; New York: Oxford University Press.

Crapper, M., Bruce, T., & Gouble, C. (2000). Flow field visualization of sediment-laden flow using ultrasonic imaging. *Dynamics of Atmospheres and Oceans, 31*(1-4), 233-245.

Dabiri, J. O., & Gharib, M. (2004). Fluid entrainment by isolated vortex rings. *Journal of Fluid Mechanics, 511*, 311-331.

Domenichini, F., Pedrizzetti, G., & Baccani, B. (2005). Three-dimensional filling flow into a model left ventricle. *Journal of Fluid Mechanics, 539*, 179-198.

Feigenbaum, H., Armstrong, W. F., & Ryan, T. (2005). *Feigenbaum's echocardiography* (6th ed.). Philadelphia: Lippincott Williams & Wilkins.

Foster, D. R., Arditi, M., Foster, F. S., Patterson, M. S., & Hunt, J. W. (1983). Computer-simulations of speckle in B-scan images. *Ultrasonic Imaging, 5*(4), 308-330.

Friemel, B., Bohs, L., Nightingale, K., & Trahey, G. (1998). Speckle decorrelation due to two-dimensional flow gradients. *IEEE Transactions on Ultrasonics Ferroelectrics and Frequency Control, 45*(2), 317-327.

Fung, Y. C. (1990). *Biomechanics : Motion, flow, stress, and growth*. New York: Springer-Verlag.

Fung, Y. C. (1993). *Biomechanics : Mechanical properties of living tissues* (2nd ed.). New York: Springer-Verlag.

Fung, Y. C. (1997). *Biomechanics : Circulation* (2nd ed.). New York: Springer.

Gatehouse, P. D., Keegan, J., Crowe, L. A., Masood, S., Mohiaddin, R. H., Kreitner, K. F., & Firmin, D. N. (2005). Applications of phase-contrast flow and velocity imaging in cardiovascular MRI. *European Radiology, 15*(10), 2172-2184.

Gharib, M., & Beizaie, M. (2003). Correlation between negative near-wall shear stress in human aorta and various stages of congestive heart failure. *Annals of Biomedical Engineering, 31*(6), 678-685.

Gharib, M., Kremers, D., Koochesfahani, M. M., & Kemp, M. (2002). Leonardo's vision of flow visualization. *Experiments in Fluids, 33*(1), 219-223.

Gharib, M., Rambod, E., Kheradvar, A., Sahn, D. J., & Dabiri, J. O. (2006). Optimal vortex formation as an index of cardiac health. *Proc Natl Acad Sci U S A, 103*(16), 6305-6308.

Gharib, M., Rambod, E., & Shariff, K. (1998). A universal time scale for vortex ring formation. *Journal of Fluid Mechanics, 360*, 121-140.

Hale, J. F., Mcdonald, D. A., & Womersley, J. R. (1955). Velocity profiles of oscillating arterial flow, with some calculations of viscous drag and the reynolds number. *Journal of Physiology-London, 128*(3), 629-640.

Hong, G. R., Pedrizzetti, G., Tonti, G., Li, P., Wei, Z., Kim, J. K., . . . Vannan, M. A. (2008). Characterization and quantification of vortex flow in the human left ventricle by contrast echocardiography using vector particle image velocimetry. *JACC Cardiovasc Imaging, 1*(6), 705-717.

Hope, T. A., Markl, M., Wigstrom, L., Alley, M. T., Miller, D. C., & Herfkens, R. J. (2007). Comparison of flow patterns in ascending aortic aneurysms and volunteers using four-dimensional magnetic resonance velocity mapping. *Journal of Magnetic Resonance Imaging, 26*(6), 1471-1479.

Jensen, J. A. (1996). *Estimation of blood velocities using ultrasound : A signal processing approach*. Cambridge ; New York, USA: Cambridge University Press.

Jensen, J. A. (2000). Algorithms for estimating blood velocities using ultrasound. *Ultrasonics, 38*(1-8), 358-362.

Kilner, P. J., Yang, G. Z., Wilkes, A. J., Mohiaddin, R. H., Firmin, D. N., & Yacoub, M. H. (2000). Asymmetric redirection of flow through the heart. *Nature, 404*(6779), 759-761.

Kim, H. B., Hertzberg, J., Lanning, C., & Shandas, R. (2004). Noninvasive measurement of steady and pulsating velocity profiles and shear rates in arteries using echo PIV: In vitro validation studies. *Annals of Biomedical Engineering, 32*(8), 1067-1076.

Kim, H. B., Hertzberg, J. R., & Shandas, R. (2004). Development and validation of echo PIV. *Experiments in Fluids, 36*(3), 455-462.

Kleinstreuer, C. (2006). *Biofluid dynamics : Principles and selected applications*. Boca Raton, FL: CRC/Taylor & Francis.

Krueger, P. S., Dabiri, J. O., & Gharib, M. (2003). Vortex ring pinchoff in the presence of simultaneously initiated uniform background co-flow. *Physics of Fluids, 15*(7), L49-L52.

Lasheras, J. C. (2007). The biomechanics of arterial aneurysms. *Annual Review of Fluid Mechanics, 39*, 293-319.

Liakopoulos, O. J., Tomioka, H., Buckberg, G. D., Tan, Z. T., Hristov, N., & Trummer, G. (2006). Sequential deformation and physiological considerations in unipolar right or left ventricular pacing. *European Journal of Cardio-Thoracic Surgery, 29*, S188-S197.

Lin, B. A., Einav, S., Zarandi, M. M., & Gharib, M. (2003). Digital ultrasound speckle image velocimetry for quantitative cardiovascular

flow visualization *5th international symposium on particle image velocimetry*. Busan, Korea: Paper 3152.

Liu, L. L., Zheng, H. R., Williams, L., Zhang, F. X., Wang, R., Hertzberg, J., & Shandas, R. (2008). Development of a custom-designed echo particle image velocimetry system for multi-component hemodynamic measurements: System characterization and initial experimental results. *Physics in Medicine and Biology, 53*(5), 1397-1412.

Mills, C. J., Gabe, I. T., Gault, J. H., Mason, D. T., Ross, J., Braunwald, E., & Shillingford, J. P. (1970). Pressure-flow relationships and vascular impedance in man. *Cardiovascular Research, 4*(4), 405-417.

Mohiaddin, R. H. (1995). Flow patterns in the dilated ischemic left-ventricle studied by MR-imaging with velocity vector mapping. *JMRI-Journal of Magnetic Resonance Imaging, 5*(5), 493-498.

Moore, J. E., Maier, S. E., Ku, D. N., & Boesiger, P. (1994). Hemodynamics in the abdominal-aorta - a comparison of in-vitro and in-vivo measurements. *Journal of Applied Physiology, 76*(4), 1520-1527.

Nagueh, S. F., Appleton, C. P., Gillebert, T. C., Marino, P. N., Oh, J. K., Smiseth, O. A., . . . Evangelista, A. (2009). Recommendations for the evaluation of left ventricular diastolic function by echocardiography. *Journal of the American Society of Echocardiography, 22*(2), 107-133.

Nichols, W. W., O'Rourke, M. F., & McDonald, D. A. (2005). *McDonald's blood flow in arteries : Theoretical, experimental, and clinical principles* (5th ed.). London ; New York: Hodder Arnold ; Distributed in the U.S.A. by Oxford University Press.

O'Rourke, M. F. (1967). Pressure and flow waves in systemic arteries and anatomical design of arterial system. *Journal of Applied Physiology, 23*(2), 139-149.

Pedersen, E. M., Kim, W. Y., Staalsen, N. H., Hasenkam, J. M., Nygaard, H., & Paulsen, P. K. (1999). Development of velocity profiles and retrograde flow in the porcine abdominal aorta under different haemodynamic conditions. *Scandinavian Cardiovascular Journal, 33*(4), 206-214.

Pereira, F., & Gharib, M. (2002). Defocusing digital particle image velocimetry and the three-dimensional characterization of two-phase flows. *Measurement Science and Technology, 13*(5), 683-694.

Pereira, F., Gharib, M., Dabiri, D., & Modarress, D. (2000). Defocusing digital particle image velocimetry: A 3-component 3-dimensional DPIV measurement technique. Application to bubbly flows. *Experiments in Fluids, 29*, S78-S84.

Porter, T. R., Hiser, W. L., Kricsfeld, D., Deligonul, U., Xie, F., Iversen, P., & Radio, S. (2001). Inhibition of carotid artery neointimal formation

with intravenous microbubbles. *Ultrasound in Medicine and Biology, 27*(2), 259-265.

Qi, X. L., Nguyen, T. L., Andries, L., Sys, S. U., & Rouleau, J. L. (1998). Vascular endothelial dysfunction contributes to myocardial depression in ischemia-reperfusion in the rat. *Canadian Journal of Physiology and Pharmacology, 76*(1), 35-45.

Qi, X. L., Stewart, D. J., Gosselin, H., Azad, A., Picard, P., Andries, L., . . . Rouleau, J. L. (1999). Improvement of endocardial and vascular endothelial function on myocardial performance by captopril treatment in postinfarct rat hearts. *Circulation, 100*(12), 1338-1345.

Raffel, M., Willert, C. E., Wereley, S., & Kompenhans, J. (2007). *Particle image velocimetry : A practical guide* (2nd ed.). Heidelberg ; New York: Springer.

Ramamurthy, B. S., & Trahey, G. E. (1991). Potential and limitations of angle-independent flow detection algorithms using radiofrequency and detected echo signals. *Ultrasonic Imaging, 13*(3), 252-268.

Robinson, D. E., Chen, F., & Wilson, L. S. (1982). Measurement of velocity of propagation from ultrasonic pulse-echo data. *Ultrasound in Medicine and Biology, 8*(4), 413-420.

Sandrin, L., Manneville, S., & Fink, M. (2001). Ultrafast two-dimensional ultrasonic speckle velocimetry: A tool in flow imaging. *Applied Physics Letters, 78*(8), 1155-1157.

Schummer, A., Wilkens, H., Vollmerhaus, B., & Habermehl, K.-H. (1981). *The circulatory system, the skin, and the cutaneous organs of the domestic mammals* (W. G. Siller & P. A. L. Wight, Trans.). Berlin: Springer-Verlag.

Sengupta, P. P., Khandheria, B. K., Korinek, J., Jahangir, A., Yoshifuku, S., Milosevic, I., & Belohlavek, M. (2007). Left ventricular isovolumic flow sequence during sinus and paced rhythms: New insights from use of high-resolution doppler and ultrasonic digital particle imaging velocimetry. *Journal of the American College of Cardiology, 49*(8), 899-908.

Shung, K. K. (2006). *Diagnostic ultrasound : Imaging and blood flow measurements*. Boca Raton, FL: Taylor&Francis.

Suetens, P. (2009). *Fundamentals of medical imaging* (2nd. ed.). New York: Cambridge University Press.

Szabo, T. L. (2004). *Diagnostic ultrasound imaging : Inside out*. Amsterdam ; Boston: Elsevier Academic Press.

Taylor, C. A., Cheng, C. P., Espinosa, L. A., Tang, B. T., Parker, D., & Herfkens, R. J. (2002). In vivo quantification of blood flow and wall shear stress in the human abdominal aorta during lower limb exercise. *Annals of Biomedical Engineering, 30*(3), 402-408.

Taylor, C. A., Hughes, T. J. R., & Zarins, C. K. (1998). Finite element modeling of three-dimensional pulsatile flow in the abdominal aorta: Relevance to atherosclerosis. *Annals of Biomedical Engineering, 26*(6), 975-987.

Theunissen, R., Scarano, F., & Riethmuller, M. L. (2008). On improvement of PIV image interrogation near stationary interfaces. *Experiments in Fluids, 45*(4), 557-572.

Thiriet, M. (2008a). *Biology and mechanics of blood flows* (Part 1. Biology). New York, NY: Springer.

Thiriet, M. (2008b). *Biology and mechanics of blood flows* (Part 2. Mechanics and medical aspects). New York, NY: Springer.

Touil, B., Bernard, O., & Friboulet, D. (2008). Motion decorrelation in echocardiography: Analysis from a realistic simulation. *2008 IEEE International Symposium on Biomedical Imaging: From Nano to Macro, Vols 1-4*, 1469-1472.

Trahey, G. E., Allison, J. W., & Vonramm, O. T. (1987). Angle independent ultrasonic-detection of blood-flow. *IEEE Transactions on Biomedical Engineering, 34*(12), 965-967.

Trahey, G. E., Hubbard, S. M., & Vonramm, O. T. (1988). Angle independent ultrasonic blood-flow detection by frame-to-frame correlation of B-mode images. *Ultrasonics, 26*(5), 271-276.

Van Dijk, P. (1984). Direct cardiac NMR imaging of heart wall and blood-flow velocity. *Journal of Computer Assisted Tomography, 8*(3), 429-436.

Vasan, R. S. (2008). Pathogenesis of elevated peripheral pulse pressure - some reflections and thinking forward. *Hypertension, 51*(1), 33-36.

Wagner, R. F., Smith, S. W., Sandrik, J. M., & Lopez, H. (1983). Statistics of speckle in ultrasound B-scans. *IEEE Transactions on Sonics and Ultrasonics, 30*(3), 156-163.

Wang, L. M., & Shung, K. K. (1996). Adaptive pattern correlation for two-dimensional blood flow measurements. *IEEE Transactions on Ultrasonics Ferroelectrics and Frequency Control, 43*(5), 881-887.

Webb, A. R. (2003). *Introduction to biomedical imaging*. Hoboken, New Jersey: Wiley.

Westerweel, J. (1997). Fundamentals of digital particle image velocimetry. *Measurement Science and Technology, 8*(12), 1379-1392.

Westerweel, J., Dabiri, D., & Gharib, M. (1997). The effect of a discrete window offset on the accuracy of cross-correlation analysis of digital PIV recordings. *Experiments in Fluids, 23*(1), 20-28.

Wigstrom, L., Ebbers, T., Fyrenius, A., Karlsson, M., Engvall, J., Wranne, B., & Bolger, A. F. (1999). Particle trace visualization of intracardiac flow using time-resolved 3d phase contrast MRI. *Magnetic Resonance in Medicine, 41*(4), 793-799.

Willert, C. E., & Gharib, M. (1991). Digital particle image velocimetry. *Experiments in Fluids, 10*(4), 181-193.

Womersley, J. R. (1955). Method for the calculation of velocity, rate of flow and viscous drag in arteries when the pressure gradient is known. *Journal of Physiology-London, 127*(3), 553-563.

Zoghbi, W. A., Enriquez-Sarano, M., Foster, E., Grayburn, P. A., Kraft, C. D., Levine, R. A., . . . Weissman, N. J. (2003). Recommendations for evaluation of the severity of native valvular regurgitation with two-dimensional and Doppler echocardiography. *Journal of the American Society of Echocardiography, 16*(7), 777-80.